Cell Migration in Two-State Micropatterns

Alexandra Fink

Munich 2020

Cell Migration in Two-State Micropatterns

Alexandra Fink

Dissertation

submitted to the

Faculty of Physics

Ludwigs-Maximilians-Universität

München

by

Alexandra Fink

born in Strausberg

Munich, 30.01.2020

Supervisor: Prof. Dr. Joachim O. Rädler

Second Examiner: Prof. Dr. Chase P. Broedersz

Date of the PhD Defense: 13.03.2020

Zellmigration in

Zwei-Zustands-Mikrostrukturen

Alexandra Fink

München 2020

Contents

Associated Publications

[**P1**]: Stochastic Nonlinear Dynamics of Confined Cell Migration in Two-State Systems[1]
David B. Brückner*, Alexandra Fink*, Christoph Schreiber, Peter J. F. Röttgermann, Joachim O. Rädler, Chase P. Broedersz
Nature Physics **15**, 595–601 (2019)

[**P2**]: Area and Geometry Dependence of Cell Migration in Asymmetric Two-State Micropatterns[2]
Alexandra Fink, David B. Brückner, Christoph Schreiber, Peter J. F. Röttgermann, Chase P. Broedersz and Joachim O. Rädler
Biophysical Journal (2019), in press

[**P3**]: Disentangling the Behavioural Variability of Confined Cell Migration[3]
David B. Brückner, Alexandra Fink, Joachim O. Rädler, Chase P. Broedersz
accepted for publication in *Journal of the Royal Society Interface*

*authors contributed equally

x

Zusammenfassung

Die Hauptakteure in der (Embryonal-)Entwicklung und bei Immunreaktionen, sowie bei Krebsmetastasen sind migrierende Zellen. Zellen passen ihre Art der Migration aktiv den von ihrer mikroskopischen Umgebung gesetzten Randbedingungen an. Um standardisierte und justierbare Mikro-Umgebungen für die Untersuchung von Zellorganisation und -migration bereitstellen zu können, wurden Mikrostrukturierungstechniken entwickelt. Die Mikrostrukturierung erlaubt es, zelladhäsive Proteine in definierten Geometrien an einer Oberfläche anzubinden, während die umgebenden Flächen zellabweisend funktionalisiert werden. Die Spreit-Dynamik von Zellen auf Mikrostrukturen wurde schon zuvor erfolgreich modelliert; und eine Vielzahl an theoretischen Modellen existieren, die die Zellmigration auf homogenen Substraten beschreiben. Im Gegensatz dazu ist wenig über die Dynamik von Zellen in einengenden Geometrien bekannt. Insbesondere ist die Frage, wie sich die Dynamik als Funktion der Geometrie der Einengung verändert, noch unbeantwortet.

In dieser Dissertation habe ich ein artifizielles mikrometerskaliges Zweizustandssystem für die Untersuchung der Zellmigration bei Einengung entwickelt. Weiterhin habe ich mehrere geometrische Bestimmungsgrößen identifiziert, die die Migrationsdynamik beeinflussen, und habe ihren Effekt quantifiziert. Das mikrostrukturierte System besteht aus zwei zellgroßen Adhäsionsflächen, die an den beiden Enden eines verbindenden Streifens liegen. Menschliche Brustkrebszellen MDA-MB-231, sowie verschiedene andere Zelllinien, migrieren in dieser Hantelgeometrie zwischen den Adhäsionsflächen hin und her. Die Migration kann durch aus den Zelltrajektorien direkt auslesbare Größen wie Beschleunigungen, Aufenthaltsdauern und Aufenthaltswahrscheinlichkeiten charakterisiert werden. In Kollaboration mit der Arbeitsgruppe Broedersz haben wir eine neuartige theoretische Beschreibung der Zellmigration in beengten Geometrien entwickelt, die ausschließlich auf der Kurzzeitdynamik basiert. Wir haben gezeigt, dass die Zellmigration in Zweizustands-Mikrostrukturen von einer stochastischen Bewegungsgleichung, die aus einem deterministischen und einem stochastischen Term besteht, beschrieben wird. Beide Terme wurden aus den Daten inferiert und eine gute Übereinstimmung zwischen Modellvorhersagen und Experimentaldaten wurde beobachtet. Insbesondere haben wir herausgefunden, dass hoch-

metastatische MDA-MB-231 Brustkrebszellen und nicht maligne Zellen aus Brustgewebe (MCF10A) auf Zweizustandssystemen mit Brückenbreite 7.2 µm verschiedene deterministische Dynamiken aufzeigen. Das Zweizustandssystem wurde weiterhin genutzt, um systematisch den Einfluss der Geometrie der Mikrostruktur auf die Zellmigration zu studieren. Dabei haben wir herausgefunden, dass die Migrationsdynamik der Zellen sensitiv gegenüber der Brückenlänge und -breite, sowie der Adhäsionsflächengröße und -orientierung ist. Insbesondere wurden die Austrittsraten der Zellen aus Adhäsionsflächen mit verschiedenen Formen bestimmt. Wir haben festgestellt, dass die Austrittsraten für isotrope Formen ausschließlich von der Adhäsionsfläche linear abhängen. Wenn die Adhäsionsflächen eine signifikante, zur Brücke der Mikrostruktur orthogonale, Ausdehnung haben, beeinflusst die Zellpolarisation die Aufenthaltswahrscheinlichkeiten.

Daraus folgend ist das Zweizustandssystem ein geeigneter Testaufbau um Zelldynamik als Funktion der einengenden mikroskopischen Umgebung zu studieren. In dieser beengten Geometrie müssen Zellen ihre Form verändern um Übergänge zwischen den zwei Adhäsionsflächen zu bewerkstelligen. Da Zelllinien mit unterschiedlichem metastatischem Potential unterschiedliche dynamische Verhalten aufzeigen, kann man potentiell die gemessene Austrittsdynamik mit klinischen Parametern wie Invasivität verbinden.

Summary

Migrating cells are key players during development and immune response, and also in cancer metastasis. Cells actively adapt their mode of migration to constraints imposed by their microenvironment. To provide standardized and tunable microenvironments for the study of cell organization and migration, micropatterning techniques were developed. Micropatterning allows the controlled deposition of cell-adhesive proteins in defined geometries on a surface while rendering the surrounding areas cell-repellent. The spreading dynamics of cells on micropatterns has previously been successfully modelled and several theoretical models exist for cell migration on homogeneous substrates. In contrast, little is known about the dynamics of cells in confining microenvironments. In particular, it is an open question how the dynamics changes as a function of the geometry of the confinement.

In this thesis, I developed an artificial micrometre-scale two-state system for the study of cell migration in confinement. Furthermore, I identified several geometric determinants affecting the migration dynamics and quantified their effect. The micropatterned system consists of two cell-sized adhesion sites at either end of a connecting stripe. MDA-MB-231 human breast cancer cells, and several other cell lines, responded to the dumbbell-like geometry by migrating back and forth between the adhesion sites. The migration can be characterized by direct readouts from the cell trajectories such as accelerations, dwell times and occupation probabilities. In collaboration with the Broedersz group, we found a novel theoretical description for cell migration in confinement that is entirely based on short-timescale readouts. We showed that the cell migration in the two-state micropattern is captured by a stochastic equation of motion consisting of a deterministic and a stochastic term. Both terms were inferred from the data and a good agreement between model prediction and experimental data was found. In particular, we established that highly metastatic MDA-MB-231 breast cancer cells and non-tumourigenic MCF10A breast epithelial cells have distinct deterministic dynamics on two-state patterns with a bridge width of 7.2 µm. The two-state setup was further used to systematically probe the influence of geometrical cues presented to the cells within the micropatterns. Thus, the migration dynamics of cells was found to be sensitive to bridge

length and width, adhesion site area and adhesion site orientation. Specifically, the escape rates of cells from differently shaped adhesion sites were determined. For isotropic shapes, it was found that the escape rates linearly depend on adhesion site area only. When adhesion sites extend significantly into the direction orthogonal to the micropattern's bridge, cell polarisation on the adhesion sites biases occupation probabilities.

Consequently, the two-state system is a suitable assay to study cell dynamics as a function of the confining microenvironment. In this particular confinement, cells have to deform in order to transition between the two adhesion sites. As cell lines of different metastatic potential exhibit different dynamic behaviour, the measured escape dynamics may possibly be connected to clinical parameters like invasiveness.

1. Introduction

In the human body, cell migration is ubiquitous; it is a physiological process occurring at all stages of life and a task performed by a variety of cell types. Thus, neurons migrate from the sites they are generated in to their target destinations during brain development[4], leukocytes migrate from blood vessels to a specific site during immune response[5] and migrating epithelial cells mediate wound healing[6]. Likewise, pathological cell migration takes place during metastasis, when cancer cells leave the primary tumour, travel with the blood flow and eventually invade distant tissues[7]. Also, the failure to reliably perform a migratory function[8] or the inhibition of cell migration by scar tissue and excreted inhibitory molecules[9] may cause pathological states or prevent regeneration.

The quantitative study of cell migration began within the last century[10,11]. Before modern digital imaging techniques were developed and became commercially available, the study of microscopic systems was labour-intense and time-resolution was limited. How different the workflow used to be is nicely illustrated in the early papers on cell migration. Thus, Przibram observed and tracked the motion of infusoria under a light microscope with the help of Abbe's drawing apparatus. Briefly, this apparatus allows the simultaneous observation of a sample under the microscope and of a pen placed on a sheet of paper next to the microscope. By creating a virtual image overlay, the user sees the tip of the pen and the sample superimposed and can easily trace objects seen under the microscope[12]. Time was given by the beats of a metronome. In this manner, it was established that infusoria moved randomly[10]. A few years later, Fürth measured mean passage times with the help of a grid pattern in the light path of the microscope and established that infusoria performed a persistent random walk[11]. His formula for the mean squared displacement (MSD) has remained a standard for the analysis of cell trajectories.

Considerable technological advances have eliminated the need for drawing apparatuses and metronomes. In stark contrast to Przibram's and Fürth's work, nowadays many cells can be imaged simultaneously, with resulting datasets comprising tens[13,14], hundreds[15], and thousands[16] of cell traces. This leads to higher statistical certitude but can give rise to many new questions, as more phenomena become visible and

experimental parameters can often be easily tuned. Related to this is the changing view of cell migration in 2D: While for many years, in line with Fürth's findings, cell migration has been described as a persistent random walk[17,18], recently, contradictory results have started emerging and challenging this view[13,19]. In their seminal work, the group of Flyvbjerg carefully and systematically analysed the migration of cells on homogeneous 2D substrates and thereby showed that the data disagrees with some assumptions of the Ornstein-Uhlenbeck process underlying the persistent random walk model. They further proposed a workflow for the construction of cell-type specific models[20]. While such "bespoke" models give analytical expressions and are certainly useful to correctly capture and predict cell-type specific motion, it is difficult to compare parameters between different cell-type-specific models, and eventually assign a biological meaning to them. Therefore, it is all the more of interest to determine whether general "laws" describing cell migration exist.

The study of cells and cell migration on unstructured two-dimensional surfaces is useful for the characterisation of cell motion[1,17,18]. Also, cellular response to different surface structures has been successfully studied on 2D substrates. These experiments were often conducted sequentially, i.e. in a way that one surface was probed per experiment[21–24]. Similarly, two different surfaces can be placed next to each other to study population-level cellular affinities towards surfaces[25–30]. Such affinity assays are of great interest for biomedical applications which frequently depend on controllable cell adhesion to surfaces. However, mostly endpoint readouts were extracted, rather than details of the cellular dynamics. In these setups, it also remains unclear how a single cell would respond if probed several times. In particular, each cell contributes only one data point that does not allow for the determination of a *single-cell* relative affinity towards different surfaces. What is more, the results are routinely averaged over the whole cell population which includes cells with a wide range of sizes and shapes. Therefore, several parameters can potentially contribute to the final readout. Hence, it is desirable to increase standardisation, i.e. to provide additional control over cell morphology and interactions. To this end, several micropatterning techniques have been developed[31–33]. Micropatterning allows the deposition of a protein of choice in regions of particular shape and size, typically over a large area of a culture dish. As many micropatterning techniques are based on reusable masks or moulds, patterns are highly reproducible. Micropatterns have successfully been utilised to study the influence of cell shape and size on survival

and function[31,32,34], to probe cell spreading[32,35,36], to map internal cell organisation[37–40], define a hierarchy of geometric shape cues on cell polarisation[41] and to immobilise cells in a defined lattice[42,43]. Micropattern shapes can be modified to address specific questions and enable (semi-)automated data analysis: A program can take micropattern dimensions and separation as an input and, based on this information, automatically define regions of interest for further data analysis[16].

Several groups have aimed to study the influence of cell shape on cell migration. One possible approach is to initially confine cells to micropatterned adhesion sites and, after the cells have adopted the shapes of the underlying micropatterns, to release them from their confinement. To this end, either an electric field has to be applied[44] or a chemical has to be added to the sample[45]. In both cases, it is possible that cells are influenced by the external stimulus, and that the substrate undergoes ill-defined changes. When the micropattern's size is scaled up, motile cells can migrate within. Thus, micropatterned lanes have proved useful to confine cell migration to 1D. In this way, the speeds of several types of persistently migrating cells could be compared[46] and *migratory fingerprints* of several cell lines migrating on ring-shaped microlanes were identified[47]. In rows of triangles and teardrop-shaped micropatterns, cells migrate preferentially in one direction[14,48,49]. Due to the high reproducibility of behaviours and therefore repeated observations, it was possible to propose several mechanisms responsible for the biased migration. In particular, Caballero et al. quantitatively analysed cellular protrusions extending over non-adhesive areas and managed to successfully capture the main geometric determinants of cellular transitions between unconnected adhesion sites. Thus, the probability to transition between two unconnected micropatterns depends on their distance, the length of cellular protrusions, the rate of protrusion generation and the available adhesive area in reach of cellular protrusions[49]. However, all these measures are cell-type and setup-dependent. Therefore, it cannot be known in advance how different cell lines will respond to a variety of anisotropic shapes. Also, in different micropattern designs, some of the identified parameters might not be well defined any more.

The aim of this dissertation is to explore and describe cell migration in confining two-state systems. While the migration of unconfined cells has been studied extensively, it is not *a priori* clear how a cell will respond to confinement. In analogy to a freely diffusing particle, confinement could alter the migratory behaviour markedly and

new laws for the motion might emerge. In a novel approach, we employ a data-driven modelling approach to capture the dynamics of cell migration in two-state patterns. Furthermore, the experiments were designed to systematically study the influence of the geometry of the confining environment on cellular migratory response. It is not known yet whether cell migration in different geometries obeys the same rules, and how the response is quantitatively altered by micropattern geometry.

Addressing these questions, this dissertation has the following structure: The key concepts and methods mentioned in this introduction, i.e. cell migration, its mathematical description and micropatterning techniques, are described in more detail in **Chapter 2**. In **Chapter 3** an artificial two-state system for the detailed study of cell migration in confinement is introduced. In this geometry, cells migrate repeatedly between the two adhesion sites. It is shown that the observed hopping behaviour of cells is a common feature of several cell types. We find a nonlinear stochastic equation of motion capturing the dynamics of cell migration in this dumbbell-like micropattern. **Chapter 4** offers a more detailed characterisation of cell migration in the two-state setup. Here, the question of how escape rates are influenced by adhesion site size, shape and orientation is studied. In addition to the measures introduced in **Chapter 3**, more coarse-grained readouts are used for the characterisation of cell response. It is found that shapes isotropic under 90° rotations only weakly influence the escape behaviour, while adhesion site area and orientation are major determinants. The internal cell organisation is linked to biases detected in occupation probabilities. **Chapter 5** summarises the key findings, provides an outlook to outstanding questions and sketches out future experiments. Experimental details are given in **Appendix A.1**, and data analysis is described in detail in **Appendix A.2**.

2. Fundamental Concepts

Cell migration is of importance in many healthy physiological processes in the human body but also for the development or progression of disease. Thus, cells migrate as single cells or collectively during embryogenesis, immunoresponse and wound healing. One of the hallmarks of cancer is the activation of the migratory ability in cells and resulting metastasis[50,51]. In cancer metastasis, cells leave the site of the primary tumour and colonise a new, secondary site. To recolonise, cells have to migrate through the basement membrane and stroma and pass through a layer of endothelial cells to enter blood vessels (Fig. 2.1). During their journey, cells encounter a variety of environments and barriers, ranging from criss-crossing extracellular matrix fibres to relatively unstructured surfaces[52]. Typically though, migration *in vivo* takes place in confining environments, where cells can either use existing tracks or create their own by degradation of extracellular matrix[53]. Typical pore diameters range from 1 to 20 µm, and fibrillar or channel-like tracks are typically 3 to 30 µm wide[54]. Whether cells need to degrade the surrounding matrix by proteases depends on the prevalent pore size in the matrix. It was also shown that no migration can occur, if matrix degradation is not possible, for pore sizes smaller than 10% of the nuclear cross-section[55]. To disentangle the cues cells face *in vivo*, microstructuring techniques were developed that provide defined *in vitro* environments.

This chapter aims to summarise the basic mechanisms underlying cell migration, to introduce micropatterning as an experimental method for the standardisation of the study of cell migration *in vitro* and to introduce theoretical models of cell migration and the migratory machinery.

2.1. The Basics of Cell Migration

Depending on their position in the body, cells are faced with 1D, 2D or 3D environments through which they migrate. One-dimensional environments *in vivo* are typically provided by collagen fibres. 2D migration occurs on the surface of physiological structures such as blood vessels or epithelial tissue. Three-dimensional
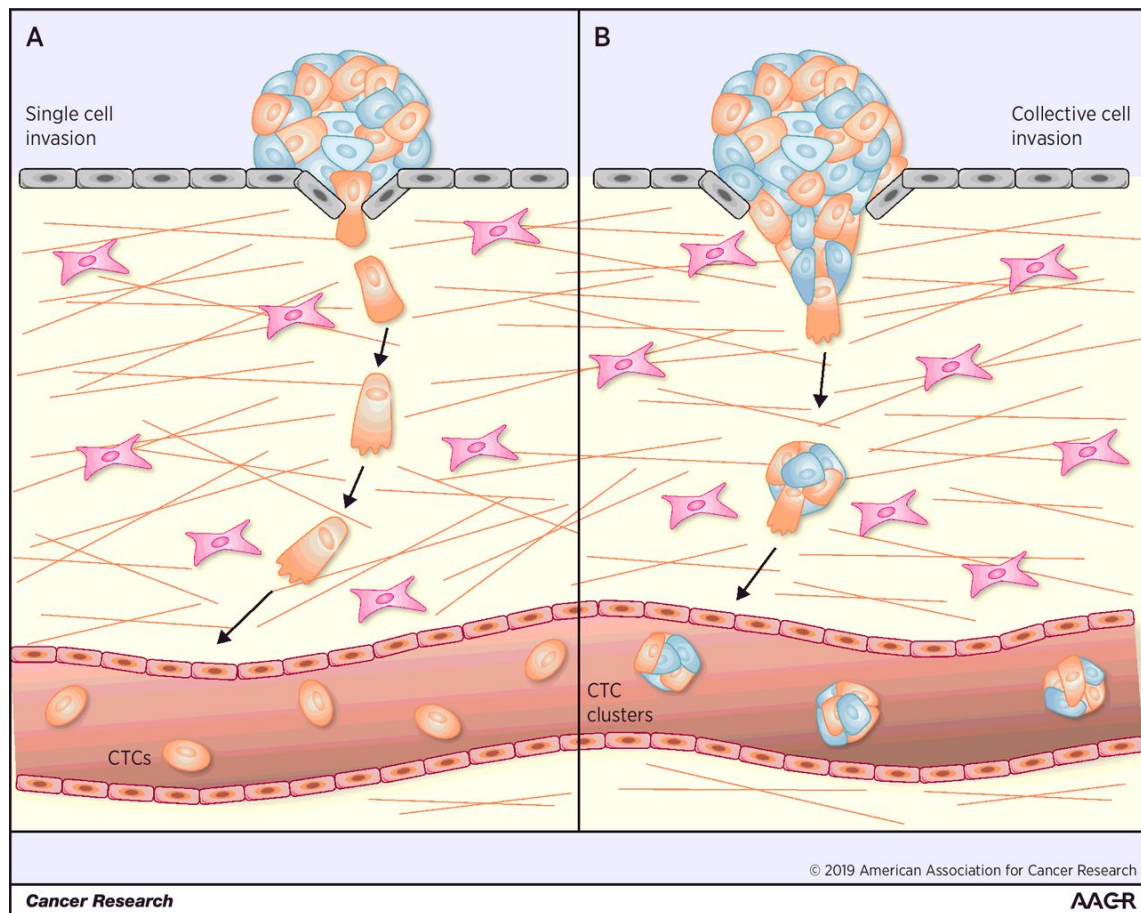
Figure 2.1.: Tissue invasion by cells. **A**: Single cells leaving a tumour site. During their migration, they interact with epithelial cells, fibroblasts, the extracellular matrix (ECM) and endothelial cells. **B**: A group of cells leaving a tumour site and migrating collectively towards a blood vessel. Reprinted with permission from VanderVorst et al.[56].
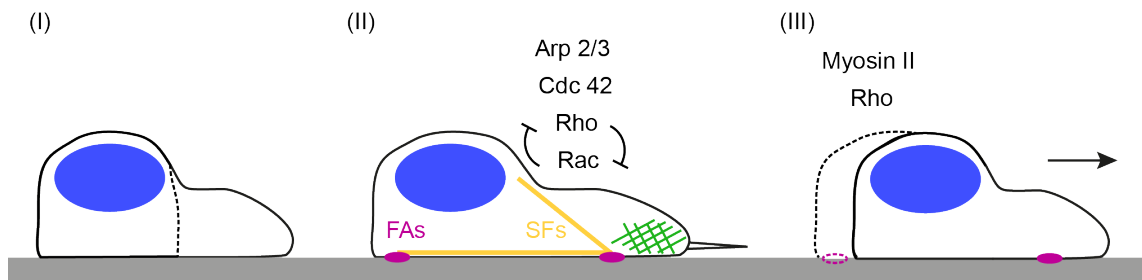
(I)   (II)   Arp 2/3   (III)   Myosin II
                Cdc 42   Rho
                Rho
                Rac
        FAs   SFs

Figure 2.2.: The cycle of cell migration. **(I)**: A cell polarises, which means that it acquires a shape with a designated front and back. The nucleus (blue) trails the cell front. **(II)**: The cell front grows. Several types of protrusions can occur: needle-like filopodia and sheet-like lamellipodia. A lamellipodium is characterised by the branched actin network inside (green). Rho, Rac, Cdc42 and Arp 2/3 are the key players mediating protrusion formation. Adhesions to the substrate form under the protrusion, providing a means for the cell to apply traction forces. These cell-substrate links are called focal adhesions (FAs) (pink). Highly contractile ventral stress fibres (SFs) (yellow) link focal adhesions inside the cell. **(III)**: The rear is retracted and the cell moves forward. In this step, which is prominently mediated by myosin II and Rho, the attachment points at the cell back are released and thereby a net translocation of the cell is achieved.

migration distinguishes between confined and discontinuous meshwork environments: Confined environments are given where cells are being "sandwiched" between structures from two sides, e.g. between fibre bundles, and discontinuous meshworks are typically encountered where extracellular matrix proteins criss-cross[57].

The cell type and the exact molecular and structural make-up of the cellular environment determine the migratory phenotype. Tumour cells are able to adapt their migratory response to the environments they face and switch between migration modes, a behaviour called *migration mode plasticity*[58,59]. It was suggested that the migration mode is determined by adhesion with the substrate, cell contractility and confinement[59]. In *amoeboid migration*, cells typically have a rounded morphology and round membrane protrusions (blebs) contribute to the migration. Typically, cells push themselves through the extracellular matrix (ECM) or deform it. Also, in amoeboid migration, adhesion to the surrounding matrix is low or absent. The variations are classified into a range of sub-modes, ranging from gliding to protrusion-mediated migration[57,60]. Conversely, in *mesenchymal migration*, cells have an elongated morphology and a defined cell front and rear. In this migration mode, cells can degrade and remodel the surrounding extracellular matrix[58,61].

Mesenchymal cell migration is a cyclic process comprising three main steps[62], which are shown in Fig. 2.2: **(I)** Cells polarise, often in response to external cues such as gradients of chemoattractants or spatial cues. Polarisation denotes an organisational difference between cell front and back. **(II)** The polarisation is accompanied by protrusion formation at the cell front. Actin polymerisation pushes the membrane forward. Typically, two types of protrusions are distinguished: lamellipodia[a], which are broad sheet-like structures with an underlying branched actin network, and filopodia, which are thin needle-like structures of parallel actin bundles. Both have distinct roles in cell migration: Lamellipodia are necessary for directional migration whereas filopodia seem to act as sensors to explore the cellular environment. The protrusions are stabilised and the cell anchors to the substrate using integrins. These sites of adhesion are a means of traction force generation. **(III)** Contractile forces generated by myosin II help to release the adhesions in the cell rear to allow for locomotion.

A host of signalling molecules is involved in all these steps of cell migration. Thus, actin polymerisation in the lamellipodium is mediated by Arp2/3, which in turn is regulated by Rho GTPases and WASP/WAVE family activators. Of the Rho GTPases, Rac1, Cdc42 and RhoA are required for the protrusion of lamellipodia and filopodia. Furthermore, the engagement of integrins in new adhesions activates Rac. Rho and Rac are antagonists, so that the presence of active Rac in the cell front leads to an inhibition of Rho. Consequently, Rho accumulates mainly on the sides and in the rear of the cell, thereby manifesting a polarised cell state. Cdc42 regulates cell polarity by restricting where protrusions form and by localising the microtubule organising centre and the Golgi apparatus. Integrins are a family of migration promoting transmembrane receptors and mechanosensors. By attaching to binding sites in the substrate, they stabilise the lamellipodium and are used for force transmission to the substrate. The strongest forces are exerted at the cell front and at the cell rear. In the cell front, new adhesions perpetually form, while older adhesions are either disassembled or reinforced. Force transmission is myosin II

---

[a]Note that, strictly speaking, the leading edge of a cell consists of two distinct functional entities, the 1-3 µm wide *lamellipodium* and the more proximal *lamella*. The *lamellipodium* is characterised by fast actin polymerisation and fast retrograde flow, whereas the *lamella* marks a region of slow retrograde flow, the presence of myosin II and focal adhesion assembly[63]. In this work, *lamellipodium* is used for both functional entities, as the experimental data does not allow a clear distinction.
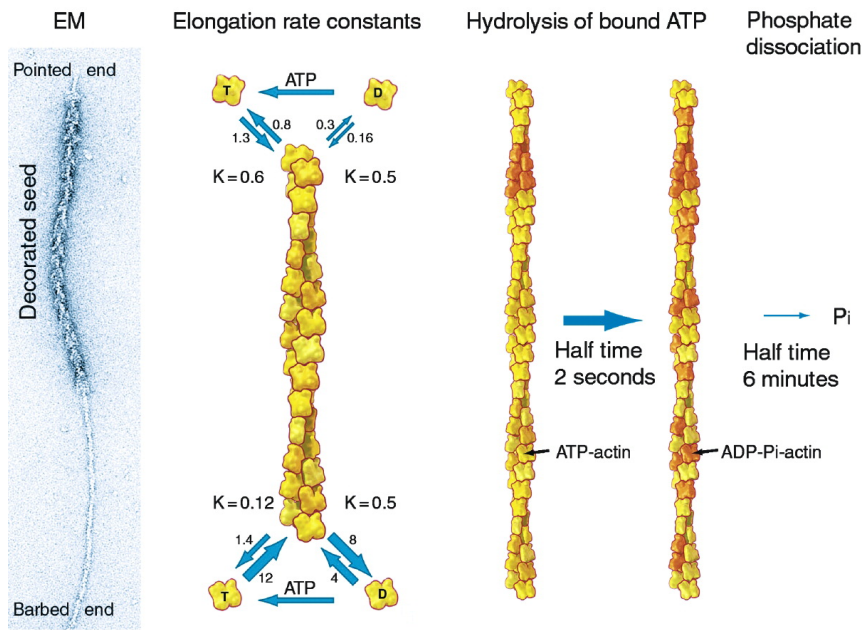
Figure 2.3.: Actin filaments. **Left**: Electron micrograph of an actin filament partially decorated with myosin motor heads ("decorated seed"), giving rise to the arrowhead pattern which gives both actin filament ends their names ("barbed" and "pointed" ends). **Second from left**: Actin filament with association and dissociation rates and equilibrium dissociation constants K for adenosine diphosphate (ADP)- and adenosine triphosphate (ATP)-actin. **Right**: Ageing of actin filaments. At first, the ATP in the ATP-actin monomers is hydrolysed, before the phosphate is slowly dissociated. Reprinted with permission from Pollard and Borisy [66].

regulated, which itself is regulated by molecules involving myosin light chain (MLC) kinase, Rho kinase, MLC phosphatase and MLC. Cell-substrate adhesion sites may be small, consisting of single integrins or may result from integrin clustering and be (much) bigger. These clusters are called focal adhesions (FAs). Ventral stress fibres (SFs) connect FAs at the cell front and rear - and through contractility they apply pulling forces over the cell length. Two other types of stress fibres have been identified, dorsal fibres and transverse arcs, and only the former are attached to focal adhesions on one end. Some details of the workings of stress fibres and of stress-fibre-focal-adhesion interactions remain unclear up to now [64]. In the last step, rear retraction, myosin II is again involved [62,65].

Interestingly, cells do not need their nuclei, microtubules, centrosomes and most other organelles to migrate. Yet actin is crucial for cell migration. Actin is also the main component of the lamellipodium, occuring in two forms: as globular monomer,
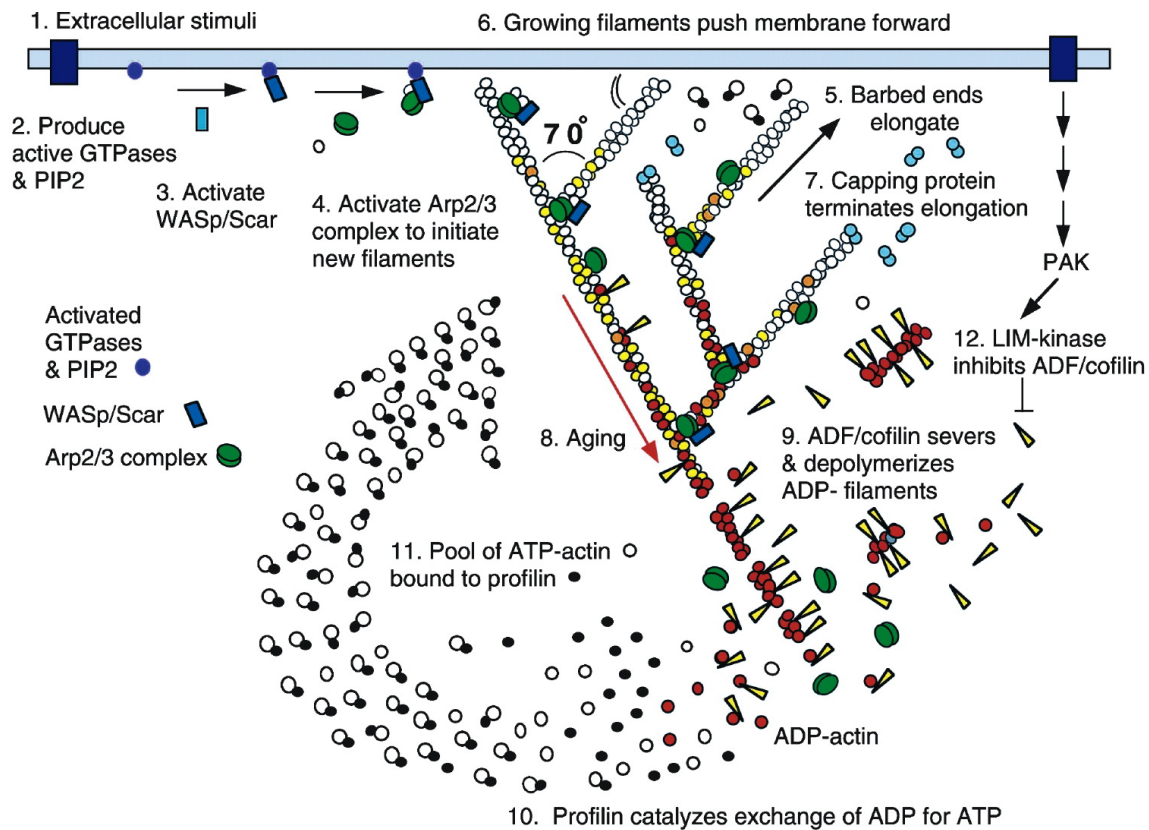
Figure 2.4.: Lamellipodial growth at the molecular level. **1.** An external stimulus triggers a signalling cascade that involves GTPases (**2.**) and WASP (identical to WASp) (**3.**). **4.** Active Arp2/3 attaches to actin filaments, initiating branching. **5.** Actin monomers attach to the barbed ends of actin filaments, which push the membrane forwards (**6.**). **7.**, **8.**, **9.** In some actin branches, elongation is capped by capping proteins. During ageing of actin filaments, ATP-actin is hydrolysed and the phosphate is dissociated, and eventually the ADP-actin-filaments are severed and depolymerised with the help of actin depolymerising factor (ADF)/cofilin. **10.** Profilin catalyses the exchange of ADP to ATP in the actin monomers, so that **11.** a pool of ATP-actin is maintained. **12.** Rho GTPases also activate PAK which activates LIM-kinase. LIM-Kinase inhibits ADF/cofilin. Reprinted with permission from Pollard and Borisy [66].

or in double-helical filaments. The electron microscope image of such a filament is shown in Fig. 2.3 on the very left. In the region called "decorated seed", an arrowhead pattern of myosin motor heads is visible. This arrowhead pattern indicates the polarity of each actin filament: The filament has a barbed and a pointed end. Actin monomers bound to ATP or ADP can bind to both ends, but the binding and dissociation rates differ between the ends (compare Fig. 2.3, second image from left), giving rise to what has been termed *treadmilling. Treadmilling* refers to the constant growth of actin filaments at their barbed ends, while simultaneously disassembly takes place at their pointed ends. It is this continuous growth and disassembly that results in protrusion growth and actin retrograde (i.e. rearwards) flow inside the cell. Within each actin filament, the ATP-actin is quickly hydrolysed (half time: 2 seconds) to ADP-P_i-actin. The dissociation of the phosphate takes place on a longer time scale, with a half time of 6 minutes[66].

Inside the lamellipodium, several actin filaments have to cooperate to exert meaningful forces needed for protrusion growth. Thus, actin filaments are densely packed at the leading edge at about 100 filaments per micrometre[67]. A scheme of the most important processes involved in protrusion formation is shown in Fig. 2.4. Rather than comprising single actin filaments, the lamellipodium consists of a branched actin network where new actin filaments grow out of existing filaments in branches. The branching is mediated by Arp2/3. Arp2/3 caps the pointed ends of actin filaments and thereby initiates growth in the direction of barbed ends only, at an angle of 70° to an existing filament. Profilin also prevents the binding of actin monomers to pointed ends and inhibits nucleation. As treadmilling can only continue in the presence of a sufficient concentration of actin monomers, it is important that the pool of monomers is not depleted and that disassembly at the ends of actin filaments takes place at a practical rate. To limit the use of actin monomers, capping proteins attach to barbed ends of actin filaments and terminate their growth. Also, actin depolymerising factor (ADF)/cofilin accelerates actin depolymerisation and phosphate dissociation. The force to push the plasma membrane forward is generated by short filaments which are highly cross-linked. To resolve the question of how actin filaments can grow while their barbed ends push against the membrane, the *elastic Brownian ratchet* mechanism was proposed: Thus, actin filaments are bending, and through this new monomers can get into place at the front[68]. Figures 2.3 and 2.4 were reproduced from the excellent review by Pollard and Borisy[66] where more

details on the molecular processes involved in actin-mediated cell migration can be found.

Myosin II is an actin-binding motor protein that walks along actin filaments and can generate contraction. Its assembly in the cell rear, and consequently the establishment of cell polarity, is tightly associated with actin dynamics. In migrating fish keratocytes, which are a model organism for the study of cell migration, myosin II localises in the lamellipodium but remains stationary with respect to the substrate. Thus, while the cell moves, myosin "relocates" to more proximal cell regions[69]. Another proposed mechanism for myosin II assembly in the cell rear is that myosin II associates with actin filaments and is transported rearwards by the retrograde flow. In the cell rear, the actin network is disassembled and actin filaments are easily contracted by myosin motors[70]. Also, a combined experimental and theoretical study found that the accumulation of myosin triggers two feedback loops: First, the contractility of myosin increases rearward actin flow, which in turn transports more myosins to the cell rear. Second, fast actin flow reduces adhesion, which in turn increases actin flow. Thereby, the polarity of migrating cells can be reinforced[71,72].

To have an effect, the forces created within cells need to be translated to the substrate. The means of doing so are FAs. Focal adhesions are integrin-based adhesion organelles which connect the actin cytoskeleton to integrins binding to the ECM. As actin cannot directly bind to integrins, other molecules need to be involved to mediate the interaction, such as talin, α-actinin and paxillin, giving rise to a layered 3D structure. FAs form as small nascent adhesions under the lamellipodium with a life time of about one minute. A subset of these nascent adhesions gets disassembled, whereas the other fraction grows into mature FAs. FA maturation requires tension application, either internally or externally, and thus focal adhesions are associated with SF assembly and myosin II activity. The working mechanism of focal adhesions is summarised in the *molecular clutch hypothesis*[73] and a schematic drawing is depicted in Fig. 2.5. Briefly, without clutch engagement, new actin monomers attach to the front of existing actin filaments, resulting in a fast retrograde flow, no traction forces and no membrane displacement (Fig. 2.5 a and b). In contrast, when the clutch becomes engaged by binding to the ECM externally and to actin internally, the retrograde actin flow slows down, leading to the transfer of traction force to the substrate. Also, the newly growing actin filaments are able to apply forces to the membrane and induce membrane protrusion (Fig. 2.5 c)[74].

In recent years, the microscopic study of the localisation of the key players of membrane protrusion events, Cdc42, RhoA and Rac1, has provided new insights. In the past, bulk measurements of protein localisation were carried out. The recent development of fluorescence resonance energy transfer (FRET)-based biosensors shifted the focus onto the study of protein activation. Thus, surprisingly, it was found that RhoA is active in a narrow band along the edge of membrane protrusions in randomly migrating cells[75]. Also, RhoA activity is low across the cell body, challenging the assumption that it is involved in FA production in the cell body[76]. However, the effectors of membrane protrusions seem to matter, as in growth-factor induced lamellipodia, no pronounced band of RhoA actication was visible[75]. In a follow-up study, the activity of all three key Rho proteins was monitored with biosensors. This confirmed the previous finding of localised RhoA activity, confined within $2\,\mu m$ of the leading edge, which coincides with edge protrusion. In contrast, Cdc42 and Rac1 are activated with a $40\,s$ delay, at a distance of $1.8\,\mu m$ from the leading edge[77]. While the different localisation of RhoA and Rac1 activities is in line with the notion that both proteins are antagonists[78], the relative spatiotemporal activation of these RhoGTPases challenges the view of how Rac and Cdc42 are involved in protrusion formation (see above).

In the absence of external cues, cells polarise and form protrusions randomly along the cell periphery. Homogeneously distributed cues may increase the rates of protrusion formation but will not induce directionality. In this case, intrinsic directionality will decide over the extent of persistence in resulting migration[79]. In contrast, the following cues can directionally bias migration:

- fibre orientation (**contact guidance**)[80]

- gradient of surface-bound adhesive molecules (**haptotaxis**)[81]

- stiffness gradient of the substrate (**durotaxis**)[82]

- gradient of chemicals in solution (**chemotaxis**)[83]

- electric fields (**electrotaxis**)[84]

Importantly, all of these cues occur *in vivo*[85].

Upon closer investigation of protrusions forming in stationary and also in migrating cells, travelling protrusion waves along the cell periphery[86,87] and periodic cycles of protrusions and retractions[86,88] were observed. It was suggested that the periodic
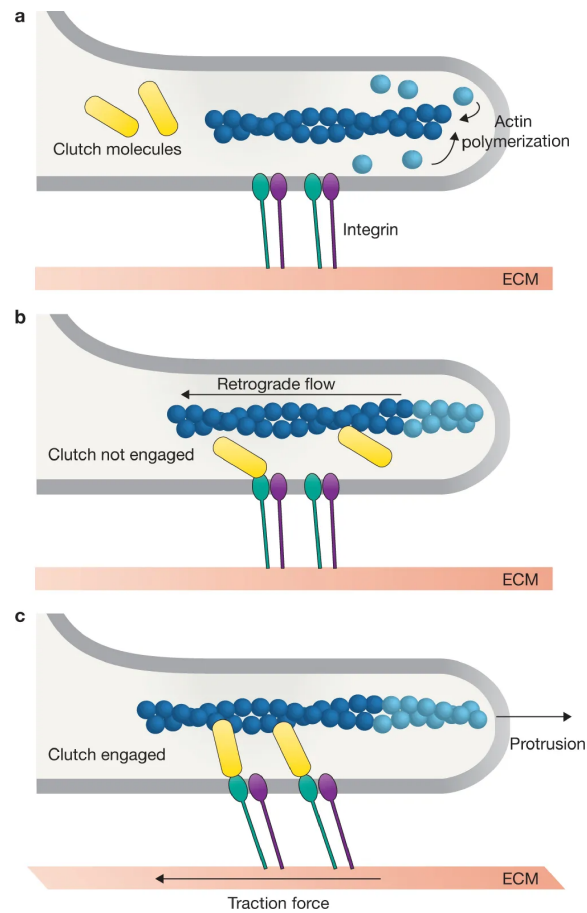
Figure 2.5.: The molecular clutch hypothesis formulated for FAs. **a**: Integrins (green and purple) are attached to the ECM and actin filaments (dark blue) grow by the binding of new actin monomers (light blue). **b**: The binding of new actin monomers to the front of existing actin filaments is accompanied by a constant depolymerisation at the back of the filaments, giving rise to *treadmilling* and a retrograde flow of actin. **c**: When the clutch becomes engaged, i.e. the integrins are connected to actin via some binding proteins (yellow), the retrograde flow can be converted into traction forces, and the binding of new actin results in membrane protrusion. Reprinted with permission from Case and Waterman[74].

contractions of lamellipodia are a means to probe substrate stiffness and to modulate adhesion to the substrate[88]. Rac1 activity plays a crucial role in travelling waves and oscillating protrusions-retraction cycles: Thus, a positive feedback loop during protrusion formation further enhances Rac1 activity, which leads to the depletion of actin monomers and eventually results in retraction[86]. Only recently, a whole-cell model comprising actin-myosin dynamics, adhesion formation and substrate deformation was developed which is able to capture the emergence of rotating lamellipodial waves. Furthermore, the model explains how cells are able to polarise in the presence of these isotropically-distributed waves[89]. This is in line with a model developed by Zimmermann and Falcke finding that for random protrusion formation, no cell signalling is necessary. Using the density and length of actin filaments, and dividing the cell front into two distinct regions, one of them gel-like and the other one semi-flexible, they were also able to predict the formation of transverse arcs[90].

Based on recent experiments, and using experimentally determined quantities for diffusion coefficients *et cetera*, models incorporating molecular processes were developed to model cellular response to external stimuli. Thus, the group of Edelstein-Keshet managed to capture the essential features of cell polarisation, as mediated by Rho proteins, using reaction-diffusion dynamics. In particular, their model is able to account for polarisation in response to several types of external stimuli as well as to describe the change of polarisation direction. For this, they made a number of assumptions, namely that the membrane-bound, active form of a Rho protein diffuses much slower than the cytosolic, inactive protein, that protein numbers are conserved and that the protein self-enhances its activity[91]. In another study it was found that the localised presence of curvature-inducing signalling molecules in the cell membrane triggers a local response in actin polymerisation, and allows to account for membrane ruffling and filopodia formation in response to external stimuli[92]. It remains a challenge to accommodate all of these principles into one working theoretical framework.

2.2. Cell Migration Assays

Due to the variability of cellular environments *in vivo*, and the corresponding necessity for cells to adapt their migration behaviour, it is difficult to repeatedly observe
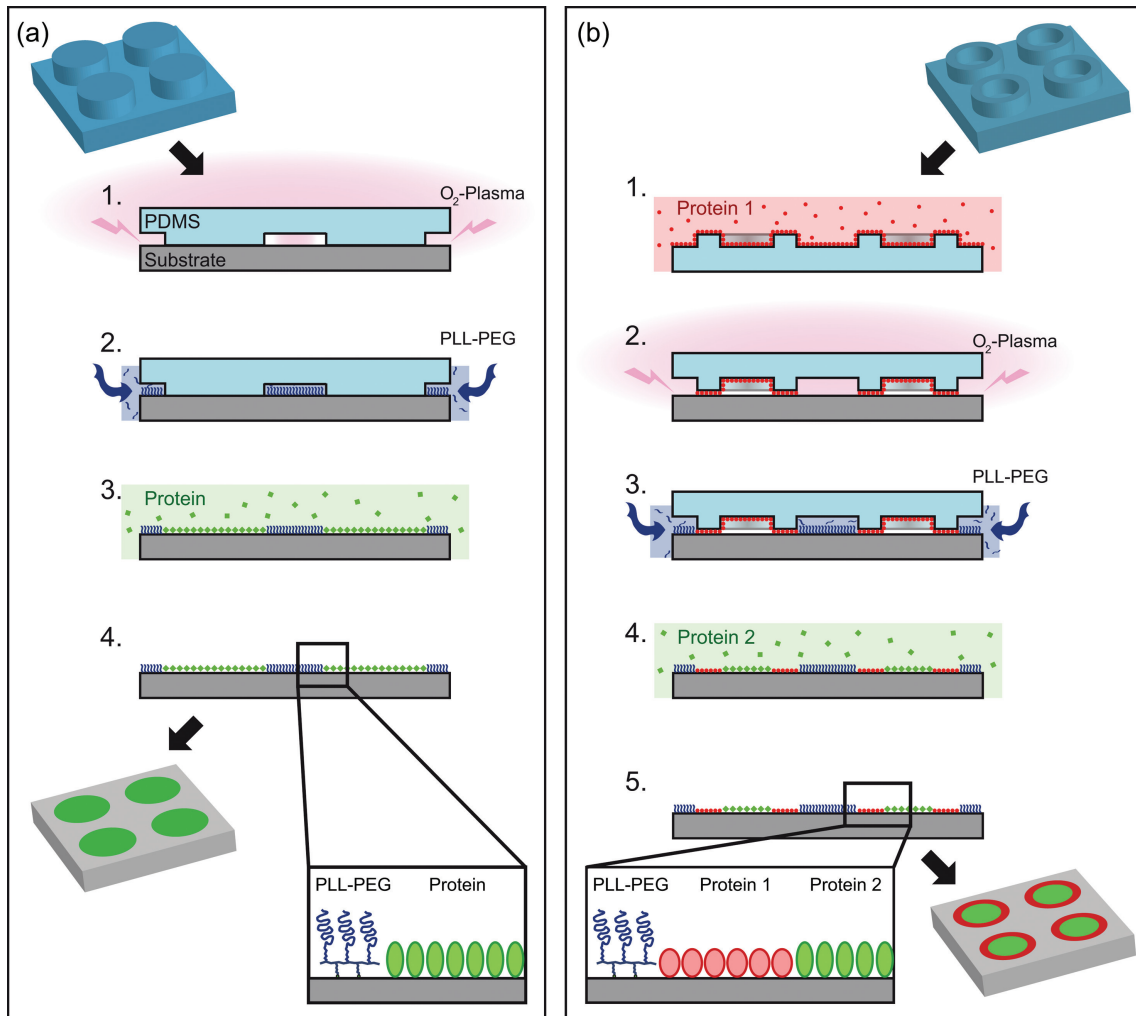
Figure 2.6.: Micropatterning techniques. **(a)**: The workflow of microscale plasma-initiated protein patterning (µPIPP). **1.** A polydimethylsiloxane (PDMS) stamp is brought into contact with a substrate, where it selectively covers some areas. These areas are not subjected to oxygen plasma (**1.**), and subsequently not passivated with poly-l-lysine-graft-polyethylene glycol (pll-PEG) (**2.**). **3.** Therefore, upon removal of the stamp, protein can adhere to the non-passivated areas. **(b)**: Workflow of two-protein patterning, which is a combination of µPIPP and microcontact printing (µCP). Two-protein patterning expressly requires framed structures, while for µCP any geometries can be used. **1.** The stamp is inked with a protein and brought into contact with a substrate (**2.**). Applying oxygen-plasma is not necessary for µCP. **3.** In the next step, pll-PEG is applied to all uncovered areas. **4.** After removal of the stamp, for two-protein patterning, a second protein can be incubated. Reprinted with permission from Segerer et al.[93].

the same processes and to gather sufficient statistics for describing and modelling migration behaviour. For that reason, several techniques for the structuring of surfaces were developed[31–33]. The advantage of such techniques is that the resulting cellular microenvironments are reproducible, tunable and well defined. Micropatterning techniques are used to deposit cell-adhesive proteins in a controlled manner, while rendering the surrounding areas cell-repellent. In particular, microcontact printing (μCP)[94–96] and microscale plasma-initiated patterning (μPIP)[97], microscale plasma-initiated protein patterning (μPIPP)[93] and variants thereof[98–101] are widely used. These techniques are polydimethylsiloxane (PDMS) stamp-based. The stamp is cast from a silicon wafer that acts as a master mould, and that can be repeatedly used. To engrave the desired structures and patterns onto the silicone wafer, photolithography techniques are employed. Here, μCP and μPIPP will be described in more detail: In μCP, the stamp is coated with a protein before it is pressed, structures facing down, onto a substrate (Fig. 2.6 (b), steps 1 and 2 without O_2-plasma). This results in the localised deposition of a protein layer on the substrate. To enable the adsorption of a cell-repellent polymer to the substrate, in this case poly-l-lysine-graft-polyethylene glycol (pll-PEG), the substrate is subjected to ultraviolet (UV) light and ozone gas prior to stamping. This activates the surface, promoting electrostatically-mediated binding between the substrate surface and the polycationic poly-l-lysine (PLL) backbone[102]. The stamp is left in contact with the substrate for a few minutes, and during that time, pll-PEG is added to bind to the substrate as well (Fig. 2.6 (b), step 3). Upon removal of the stamp, the substrate comprises protein-coated microstructures with cell-repellent surroundings.

For μPIPP, the bare stamp, structures facing down, is brought into contact with the substrate. Afterwards, all areas which are not covered by the stamp are subjected to oxygen plasma treatment (Fig. 2.6 (a), step 1). Plasma treatment is another way to activate the substrate to promote pll-PEG binding. While the stamp is still on the substrate, pll-PEG is incubated. When the stamp is removed, activated, PEG-coated and untreated, blank surface areas are present on the substrate. In a final step, a protein is added that can be physisorbed to the blank, hydrophobic substrate surface (Fig. 2.6 (a), step 3). Note that both techniques may be combined to allow for the patterning of two proteins, as shown in Fig. 2.6 (b)[93].

Cells plated on micropatterned surfaces self-organise on the surface[103]. Once they attach to a micropattern, cells spread to adopt the underlying shape[32], and thus

enable the study of internal cell organisation with respect to the adhesive geo-metry[37–40], yielding a map of internal cell organisation by averaging over several cells of equal shape. Such experiments allow to observe changes in cell organisation induced by drugs and genetic knockouts[104,105]. If the adhesive area or the number of adhesion sites is increased, microstructured environments can also be used to study cell migration. Thus, micropatterned lanes, with their ability to confine cell motion to 1D, have proved useful for extracting and ranking cell motility parameters. Due to the standardisation of cell behaviour, it was possible to measure these quantities for several cell types[46,47]. When asymmetric geometric shapes are patterned close to each other in a row, or if connected, they can guide cell migration directionally, a mechanism termed *ratchetaxis*[14,48,49].

2.3. Theoretical Description of Cell Spreading and Migration

The trajectories of cells migrating freely on a homogeneous 2D substrate are shown in Fig. 2.7. For decades, such a motion has been described as persistent random walk (i.e. an Ornstein-Uhlenbeck process)[17,18] with Fürth's formula[11] for the MSD as central descriptor:

$$\langle d(t)^2 \rangle = 2n_{dim}D(t - P[1 - \exp(-t/P)]) \tag{2.1}$$

with n_{dim} number of dimensions, P persistence time and D diffusion coefficient.

Technological advances improving time-resolution and statistical certitude are main contributors to the recent advances in the understanding of cell motility. Over the last two decades, contradictory results have started emerging and the prevalent view has been challenged, both in 2D[19,20,106] and 3D[107]. In particular, it was shown that the persistent random walk does not capture all features of the data collected for several motile cell lines: In three dimensions, an anisotropic random walk correctly describes the data[19]. In 2D, made-to-measure models including memory kernels of past velocities have been proposed and shown to describe cell motility data[20,106].

When confined to micropatterns, cell shapes and migratory behaviours are different to those of freely moving cells: Arbitrary shapes can be imposed on the cells and
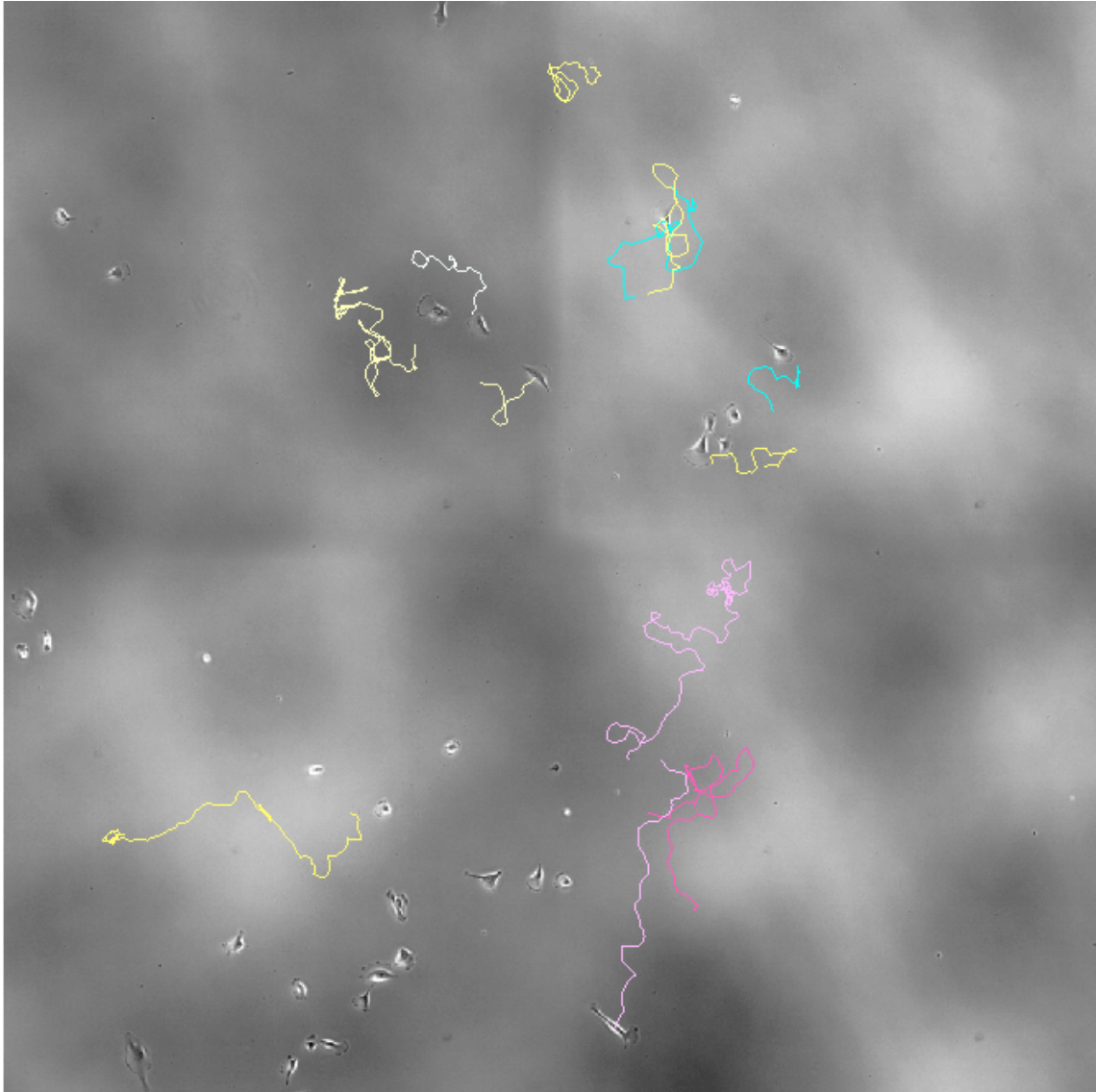
Figure 2.7.: MDA-MB-231 cells spreading and migrating on a homogeneously fibronectin-coated surface. The coloured lines represent trajectories of single cells. Due to the brightness variation, it can clearly be seen that for the analysis of freely migrating cells four individual fields of view were stitched together to allow for longer tracking. Image courtesy of C. Schreiber.

micropatterned environments act as constraints on the migration. Thus, it is not *a priori* clear how cell migration in these microenvironments can be described with respect to the additional determinants.

There are models that describe cell shape in confining environments. Thus, to model cell shapes on micropatterned adhesion sites, a Cellular Potts Model (CPM) combined with a tension-elasticity model has been successfully utilised. In order to determine the spreading shape and dynamics, the following energy functional has been assigned to each cell:

$$H = \sigma A + \lambda_s l + \sum_{arc\,i} \frac{EA}{2L_{0,i}}(L_i - L_{0,i})^2 - \frac{E_0}{A_{ref} + A_{ad}} A_{ad} \tag{2.2}$$

where the first and second term comprise surface tension, σ, which scales with cell area A and line tension, λ_s, scaling with cell perimeter l, respectively. The third term accounts for free arcs over non-adhesive areas, with the one-dimensional elastic modulus EA and contour lengths of free spanning cell edges, L_i and L_0 (rest length). The last term takes the adhesive geometry into account. In particular, the adhesive area A_{ad} does not have to be equal to cell area and thereby can give rise to free arcs. E_0 and A_{ref} are parameters controlling adhesive energy[36].

To describe the motion of cells confined to micropatterned stripes[108] or in contact with a surface of tilted micropillars[109], the language of energy potentials has also been employed, with the cell modelled as an active Brownian particle in a potential, successfully reproducing the experimentally observed migratory response. Similarly, a phase-field model including cell-substrate adhesions, actin and myosin contractions and the cytoskeleton as an active viscous compressible fluid, has predicted periodic migration and turning on micropatterned stripes[110]. Such a behaviour has indeed been observed experimentally[111].

On ratchets, i.e. a series of micropatterned anisotropic adhesion sites, cells are typically modelled as random walkers on a lattice: Thus, the probability to walk over several sites in the same direction depends on the number of sites and on the individual probability to exit an adhesion site to the left or right[14]. Alternatively, on a more mesoscopic level, the direction chosen by a cell depends on the frequency of its protrusions in that direction and on the time the protrusions dwell on the probed adhesive area[49].

3. The Bridge Modulates Cell Migration in Two-State Patterns

While freely migrating cells have been extensively studied (see Section 2.3), much remains unknown about the dynamics of cell migration in confining geometries. This is all the more surprising as cells frequently encounter confining geometries *in vivo*. In this chapter, a versatile dumbbell-like two-state micropattern to study single cell migration in confining geometries is introduced. Cells repeatedly migrate back and forth between the two adhesion sites. Using a data-driven modelling approach, we find an equation of motion. The dynamics of cell migration in the two-state system is modulated by bridge length and width.

Most of the results presented in this chapter were published in Publication [P1]. The variability in cell behaviour mentioned in this chapter is described in more detail in Publication [P3]. New results are presented in Chapter 3.4.

3.1. Phenomenology of Cell Migration in Two-State Patterns

Within five hours of cell deposition on the microstructured substrate, a sufficient number of cells have adhered to the dumbbell-shaped micropatterns consisting of two square adhesion sites and a connecting stripe (Fig. 3.1). The adhesion site area was chosen to be similar to the size of freely migrating MDA-MB-231 human breast carcinoma cells. Cells usually adhere to one of the two adhesion sites and spread within. Afterwards, a typical order of morphologies can be observed (see also Fig. 3.2 A):

  (i) membrane ruffling

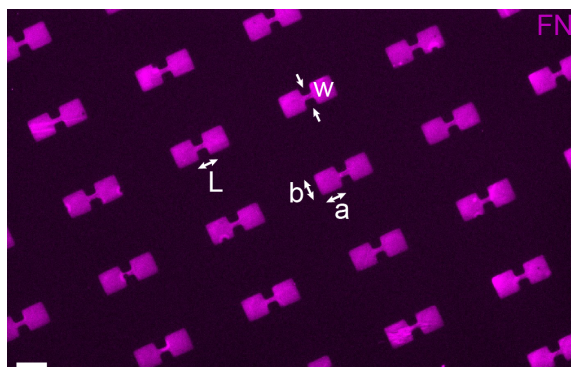 (ii) protrusion formation

(iii) lamellipodial extension and growth

Figure 3.1.: Fluorescently labelled dumbbell-shaped micropatterns. The main geometric parameters are indicated, namely bridge length L, bridge width w and adhesion site edge lengths a,b.

While a cell is located within one adhesion site, membrane ruffles, visible as dark regions in the phase contrast images, can be seen along the periphery of the cell (Fig. 3.2 A, denoted by the white arrows). These membrane ruffles indicate inefficient lamellipodial protrusions and sites of densely packed actin[112] during the exploration of the adhesion site. That the black regions on the cell periphery, or at the lamellipodial tip, coincide with actin accumulation can be seen in LifeAct-GFP stained cells migrating on the same type of dumbbell patterns, as shown in Fig. 3.2 B. Protrusions forming at the bridge entrance can grow into mature lamellipodia. However, some of these protrusions are retracted again. In most cases, a protrusion reaching the unoccupied island and its tip growing into a fan-like shape, is a safe indicator for a subsequent transition of the cell body. Before transitioning, the cell rear rounds up, as can be seen by the white halo around it in Figure 3.2 A. Once the cell body has transitioned over the narrow bridge, the cell spreads on the new adhesion site and the described typical morphological sequence starts again. At high optical magnification, filopodia extending over the passivated areas surrounding the fibronectin-coated micropatterns and retraction fibres (RFs) trailing the cell can be observed. Also, aligned in the direction of cell polarisation, faint stress fibres (SFs) spanning over the cell body are visible in LifeAct-stained cells (Fig. 3.2 B with SF direction indicated by the yellow line and RFs indicated by pink arrows).

Microscale plasma-initiated protein patterning (μPIPP) allows for the simultaneous production of thousands of adhesion sites. MDA-MB-231 cells reliably follow the previously described behaviour on dumbbell-like two-state patterns, so that, per exper-
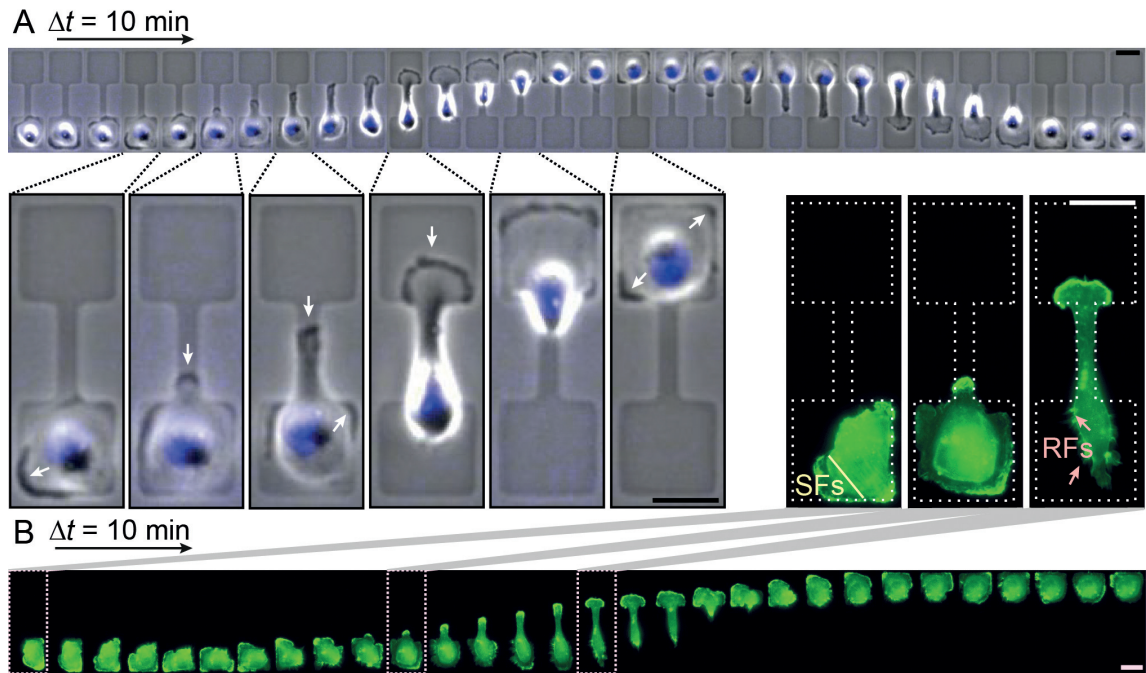
Figure 3.2.: Timeseries of single MDA-MB-231 cells migrating in the two-state micropattern. **A**: Snapshots with a time difference of 10 minutes of a single cell in the dumbbell-like micropattern. The cell is migrating repeatedly back and forth between the two square adhesion sites. Below is a zoom-in: The cell spreads into the adhesion site and forms membrane ruffles (dark regions, indicated by white arrows). These ruffles can grow to become mature protrusions inside the channel. Once a lamellipodium reaches the unoccupied adhesion site, the cell rear rounds up and the cell transitions over the bridge. Afterwards, the process repeats. **B**: Timeseries of a LifeAct-GFP stained cell. The time interval is 10 minutes. Bright actin hotspots at the cell periphery are visible. Above is a zoom-in where stress fibres (SFs) and retraction fibres (RFs) are visible. SF orientation is illustrated by the yellow line and pink arrows indicate RFs. Scale bars: 25 μm. Figure adapted and modified from published version in Brückner et al. [1].

iment, hundreds of cells hop between the two adhesion sites. A typical experimental field of view is shown in Fig. 3.3 A. In order to track these cells semi-automatically, their nuclei are labelled with Hoechst 33342. Experiments are run for up to 50 h, and single cell trajectories are recorded until the cells round up for division or until the end of a measurement. For each cell, the trajectory of the labelled nucleus is extracted. Trajectories of 149 cells, recorded in seven experiments, are shown in Fig. 3.3 B. While all the trajectories exhibit similar behaviour, showing repeated rapid transitions between the sites, the variability in trajectories is striking. Thus, some cells transition frequently in a very regular manner, while other cells either show a large variability in their migration pattern or transition only rarely. A sample trajectory is shown in more detail in Fig. 3.3 C: First, transitions between the adhesion sites occur rapidly, which is why the setup may effectively be considered as a two-state system. In this context, the dwell time τ is defined as the time between two subsequent transitions of the centre of the cell nucleus over the middle of the bridge. The definition of τ is illustrated by the two dotted lines in Fig. 3.3 C. Second, although cells do not perform any net movement while located on the square adhesion sites, an intrinsic noise in the trajectories is visible. This most likely correlates with the exploration of the adhesion site and the surroundings, as well as with protrusion formation on the bridge. The previously described heterogeneity of trajectories is also manifested in the broad distribution of dwell times seen in Fig. 3.3 D. While dwell times, and their distributions, give insight into the dynamics of the system, we can also quantify cellular behaviour on two-state micropatterns using occupation probabilities (Fig. 3.3 C). Occupation probabilities are given by the normalised distributions of cell positions on the micropatterns.

Not all cells are included in the analysis. While it is clear that non-moving cells cannot be used for further analysis, some other considerations need to be taken into account. Thus, trajectories are typically cropped in a way that excludes the first and the last stay. This is done to avoid artefacts, as the lengths of the first and last stay are determined by the start and the end of the measurement, respectively, rather than by the cellular dynamics itself. More details on cell exclusion criteria can be found in Appendix A.2.

Interestingly, the hopping behaviour is a common feature in several cell lines (Fig. 3.4). Cell lines derived from different species and tissues and of variable invasive potential all transition between the two adhesion sites. All types of cells used, and their
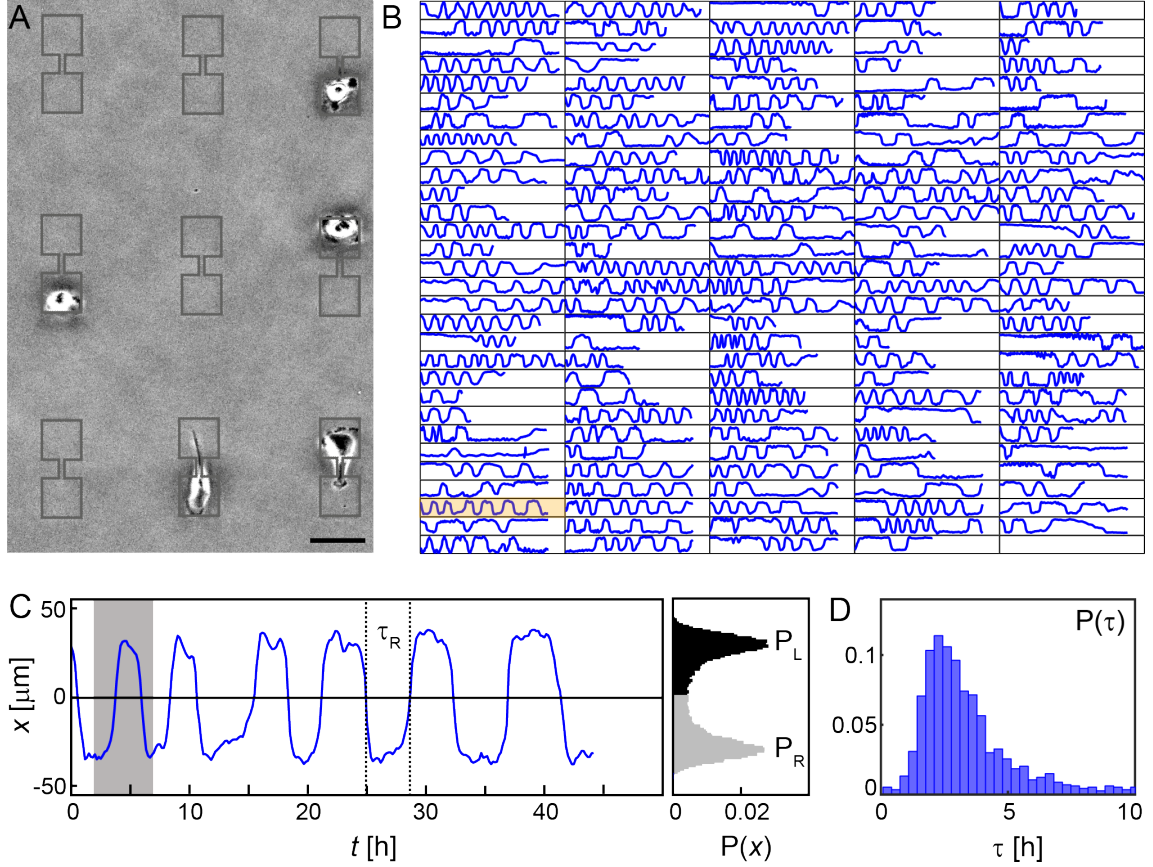
Figure 3.3.: Experimental readouts. **A**: Typical experimental field of view. Cells are sparsely seeded to ensure that only single cells occupy the micropatterns. The image is denoised and drawings of the micropatterns are superimposed. Scale bar: 50 μm. **B**: All trajectories of experiments performed on micropatterns with a bridge length L of 35.3 μm. The length of the trajectories varies due to cell division and the length of measurements. The vertical axis is position along the long axis of the micropattern, the horizontal axis is time. **C**: Zoom-in for the trajectory highlighted in orange in **B**. The grey region corresponds to the nuclear trajectory of the cell shown in Fig. 3.2 A. Also, the definition of a dwell time on the right side of the dumbbell, τ_R, is marked. When all cellular positions are counted and plotted, the resulting histogram looks like that shown on the right. The histogram depicts the occupation probabilities. **D**: Probability distribution of dwell times τ for L=35.3 μm. Figure adapted and modified from published version in Brückner et al.[1].

Property ⟍ Cell Line	Invasiveness	Species	Tissue	Disease
MDA-MB-231[113]	$+++$[114] $\backslash ++$[115]	human	breast	carcinoma
MCF10A[116]	$+$[115]	human	breast	fibrocystic disease
MDA-MB-436[117]	$++$[114] $\backslash +++$[115]	human	breast	carcinoma
MDCK[118]	- (low)[119]	dog	kidney	none
A549[120]	yes[121]	human	lung	carcinoma
HuH7[122]	low[123]	human	liver	carcinoma

Table 3.1.: Overview over all cell lines used in this work. An invasiveness rating is given according to literature. However, it is not possible to relate the invasiveness of cell lines of different tissues to each other, as no such studies comparing these cell lines exist.

invasiveness, are summarised in Table 3.1. For MCF10A and MDA-MB-436 cells, the typical morphological sequence, as described previously for MDA-MB-231 cells (in Chapter 3.1), consisting of membrane ruffle formation, extension of a lamellipodium and rounding of the cell body during the bridge passage, is visible. The details of adhesion site exploration are concealed by a white halo for MDCK and A549 cells (Fig. 3.4 B, C). This halo indicates that the cells extend well into the z-direction, either because they do not have sufficient space to spread on the adhesion site or because they cannot adhere properly on the fibronectin-coated surface. For experimental reasons, such as dwell times well below typical division times and good adhesion to fibronectin-coated surfaces, we decided to further investigate the migration behaviour of MCF10A breast epithelial cells in two-state micropatterns and compare it to that of MDA-MB-231 cells. This also allows a quantitative comparison between a cancerous and a non-cancerous cell line derived from the same tissue.

3.2. Dwell Times Scale with the Bridge Length

To challenge the observed hopping behaviour and to study its universality and limits, in the next step, we designed two-state patterns with variable bridge lengths L while maintaining a constant bridge width w of $7.2 \, \mu m$. Specifically, we have studied cell
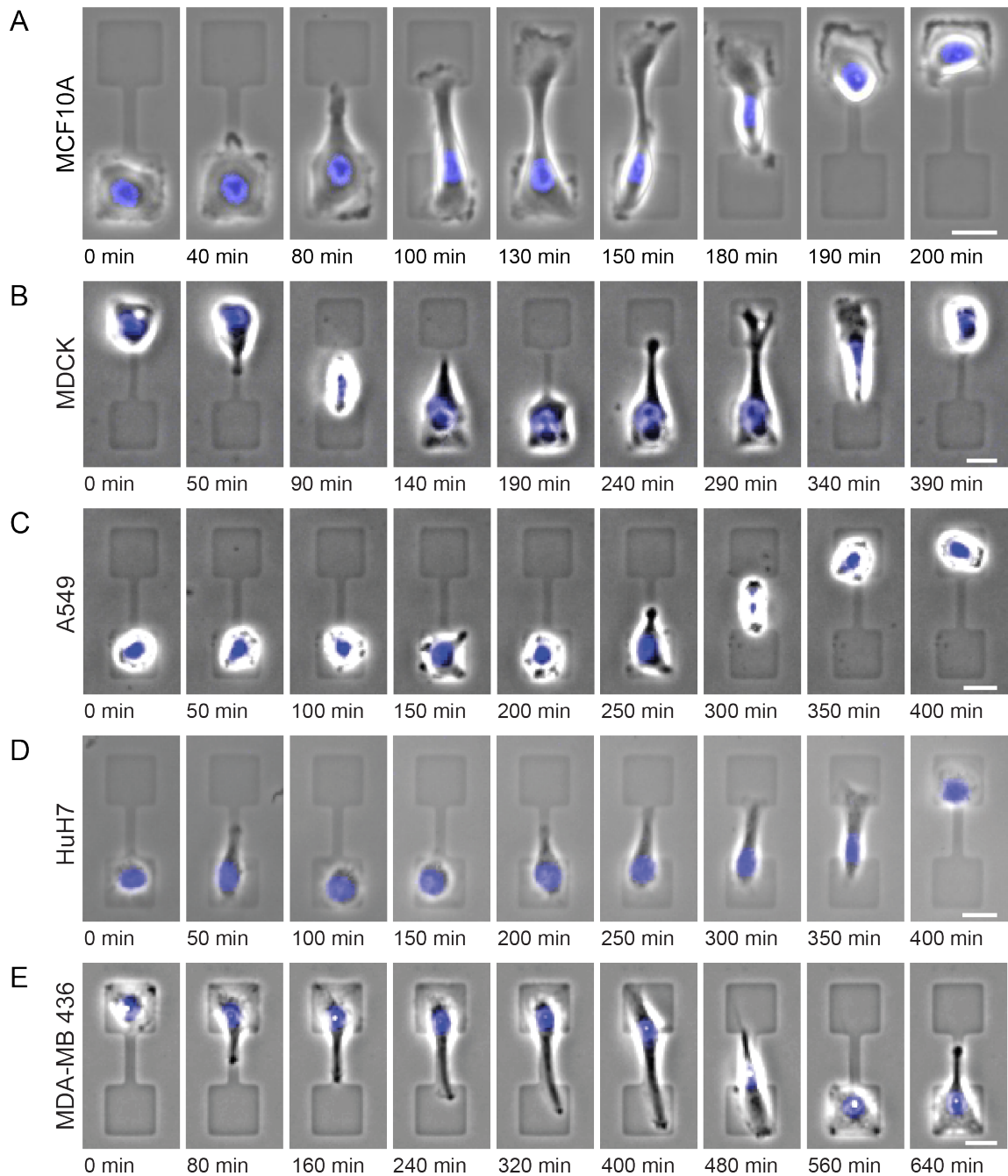
Figure 3.4.: Timeseries of different cell lines migrating on the two-state micropatterns. All tested cell lines transition between the adhesion sites. Their different morphologies on the micropatterns are visible. White halos indicate that cells extend into *z*-direction rather than being nearly flat. **A**: MCF10A, a cell line also further probed in this thesis. **B**: A single MDCK epithelial cell. **C**: A549 human lung carcinoma cell. **D**: HuH7 liver carcinoma cell. **E**: A MDA-MB-436 breast carcinoma cell. Scale bars: 25 µm. Figure adapted and modified from Supplementary Information of Brückner et al.[1].

migration behaviour on micropatterns with bridge lengths ranging from $L = 6.4 \pm 0.3$ µm to $L = 56.0 \pm 0.3$ µm. Details on the statistics for each bridge length, and on the exact measures of all other L, can be found in Appendix A.2.

For all studied bridge lengths, MDA-MB-231 cells perform transitions with the same morphological sequence as described previously (Fig. 3.2 and Fig. 3.3). The distribution of dwell times for each bridge length L can be visualised with the help of *survival probability functions S(t)*. *S(t)* gives the probability that after a certain time t a cell has <u>not</u> transitioned to the other site. When plotting *S(t)* for all used bridge lengths, we find that the distributions get broader with increasing L (Fig. 3.5 A). However, when the time axis for each geometry is re-scaled by the mean dwell time $\langle \tau \rangle$, all curves collapse onto a single master curve (see inset in Fig. 3.5 A). Plotting $\langle \tau \rangle$ against L reveals a linear increase (Fig. 3.5 B). The data collapse observed in Fig. 3.5 A means that the process underlying the transitions is the same for all bridge lengths. Therefore, we can look for a model describing our data.
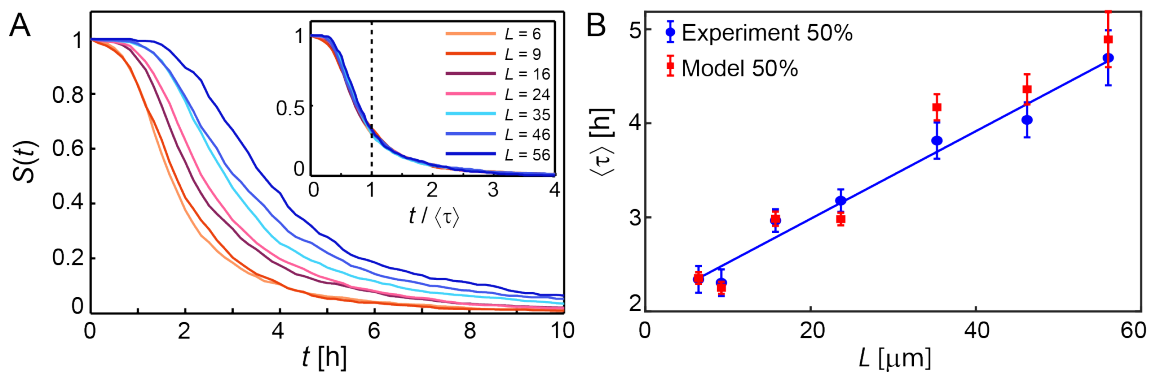

Figure 3.5.: The dependence of dwell times τ on bridge length L. **A**: Survival probability functions *S(t)* of dwell times on micropatterns with different bridge lengths. The distributions get broader with increasing bridge length. Inset: When the time-axis is re-scaled by the mean dwell time $\langle \tau \rangle$, all *S(t)* collapse onto the same master curve. L given in µm. **B**: The mean dwell times $\langle \tau \rangle$ increase linearly with increasing bridge length L. The agreement between experimentally determined and theoretically predicted $\langle \tau \rangle$ (blue and red datapoints, respectively) is good. Figure adapted and modified from published version in Brückner et al.[1].

3.3. Nonlinear Cellular Dynamics in Response to the Presence of a Constriction

Similar to motion on homogeneous 2D substrates, and as a starting point, we postulate that the cell motion in two-state micropatterns can be described by a generalised Langevin equation:

$$\frac{dv}{dt} = F(x, v) + \sigma(x, v)\eta(t) \tag{3.1}$$

As in the Ornstein-Uhlenbeck model for describing persistent random motion, the noise term $\sigma(x, v)$ is multiplied by uncorrelated Gaussian white noise $\eta(t)$. In contrast, here both the deterministic force term $F(x, v)$ and the noise strength $\sigma(x, v)$ depend on position x and velocity v. The terms are inferred by conditional averaging from the experimentally acquired trajectories as follows:

$$F(x, v) = \langle \dot{v} | x, v \rangle \tag{3.2}$$

$$\sigma^2(x, v) = \Delta t \langle [\dot{v} - F(x, v)]^2 | x, v \rangle \tag{3.3}$$

where Δt is the experimental time resolution (=10 minutes).

Importantly, both terms Eq. 3.2 and Eq. 3.3 only depend on the local accelerations $\dot{v}$, and thereby no explicit knowledge about dwell times τ enters the model. The model is "trained" on 50% of the data and its predictions are compared to the remaining 50% of experimental data.

Looking at the phase-space maps of $F(x, v)$ and $\sigma(x, v)$ is instructive, in particular to study the influence of the presence of the bridge (Fig. 3.6 A-C, with $F(x, v)$ in the top row and $\sigma(x, v)$ in the bottom row). The bridge is marked as the area between the two dashed lines. For the two different cell lines studied in detail, MDA-MB-231 (Fig. 3.6 A) and MCF10A (Fig. 3.6 C), few differences in the phase-space maps of $F(x, v)$ (top row) and $\sigma(x, v)$ (bottom row) are visible. For both cell lines, the highest velocities on the adhesion sites, or when transitioning towards an adhesion site, are decelerated the most. Also, motion on the adhesion sites directed towards the bridge is counteracted. Further, for both cell lines, just upon entry into the channel, the cell
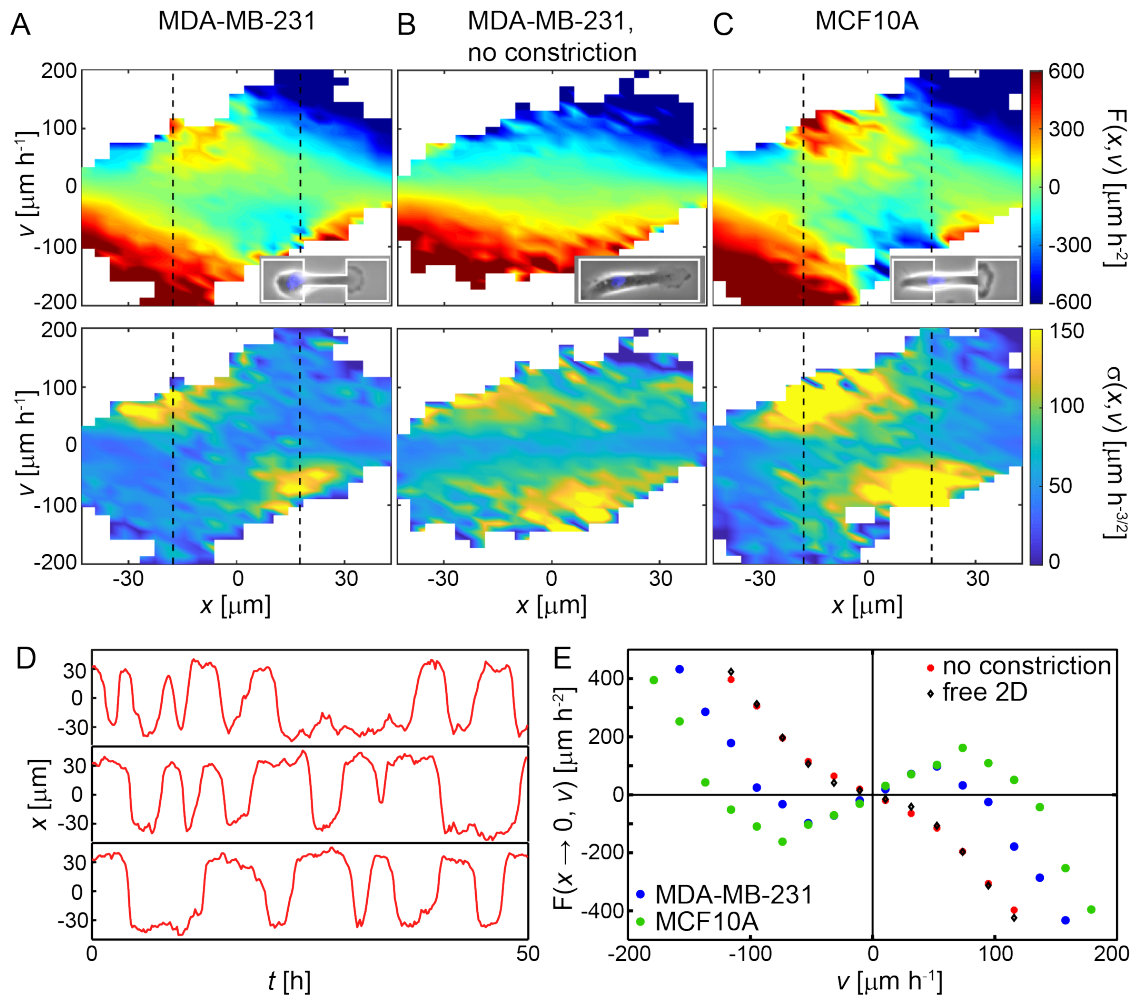
Figure 3.6.: Stochastic nonlinear dynamics of MDA-MB-231 and MCF10A cells migrating in confinement. **A**, **B**, **C**: Top row: x-v phase space maps of the deterministic component $F(x, v)$ of the cell migration for different cell lines (MDA-MB-231 and MCF10A) and on different micropatterns (rectangular stripe and two-state patterns). Bottom row: x-v phase space maps of the stochastic component $\sigma(x, v)$ of cells migrating in the patterns shown above. The black dashed lines indicate the boundaries of the bridge with $L = 35.3 \, \mu\text{m}$. **D**: Sample trajectories predicted by the model. **E**: The acceleration in a small interval around the middle of the channel plotted against velocity v. The dynamics of MDA-MB-231 cells (blue dots) and MCF10A cells (green dots) show similar behaviour. Also, MDA-MB-231 cells in rectangles (red dots) and MDA-MB-231 cells migrating on homogeneous 2D substrates show similar dynamic behaviour. Figure adapted and modified from published version in Brückner et al.[1].

is accelerated. For MCF10A cells, this acceleration seems to start just outside the channel. The most striking differences in $F(x, v)$ are the presence of high velocities at the micropatterns' left and right edges for MCF10A cells, thereby increasing the phase space with respect to MDA-MB-231 cells, and higher accelerations inside the channel for MCF10A cells. Interestingly, for MDA-MB-231 cells, the highest noise is visible just at the channel entrance, whereas for MCF10A the noise level persists to be high within the channel as well. If the bridge is removed, the regions of increased acceleration within, or next to, the bridge vanish, and the phase space landscape seems more uniform (Fig. 3.6 B (top)) with the cells being mainly decelerated. Also, the noise levels $\sigma(x, v)$ are more uniformly elevated.

More insights into the cellular dynamics can be gained by plotting the deterministic component against velocity in a small interval around the middle of the bridge ($F(x \to 0, v)$, Fig. 3.6 E). The data plotted can be divided into two groups, free cells and confined cells, with free cells comprising cells migrating on a uniform 2D surface and cells on a wide stripe without constriction. The behaviour of $F(x \to 0, v)$ is very similar for both types of free cells, as the cells are always decelerated. Interestingly, the behaviour of MDA-MB-231 and MCF10A cells is also similar; while both cell lines experience deceleration for high velocities, they are accelerated for low velocities. This is most pronounced for MCF10A cells.

We can test the predictive qualities of the model by visually comparing the experimentally acquired trajectories (Fig. 3.3 B,C) with those generated by the model, as shown in Fig. 3.6 D. The similarity of the trajectories is striking, and most importantly, the hopping behaviour, although not encoded in the model, is captured. When analysed analogously to experimental data, we can extract the mean dwell times from the theoretical trajectories for different bridge lengths and compare them to the experimental values (Fig. 3.5 B). A good agreement between experimental and theoretical values for $\langle \tau \rangle$ is observed for all L.

When simulating trajectories in the deterministic flow fields, the differences between the studied systems become apparent. Thus, for different initial conditions, the trajectories in the deterministic phase space for MDA-MB-231 cells always converge onto the same limit cycle (Fig. 3.7 A). In effect, MDA-MB-231 cells deterministically perform an oscillatory motion on the two-state micropatterns. In contrast, the deterministic dynamics of MCF10A cells encodes a bistable system (Fig. 3.7 C).
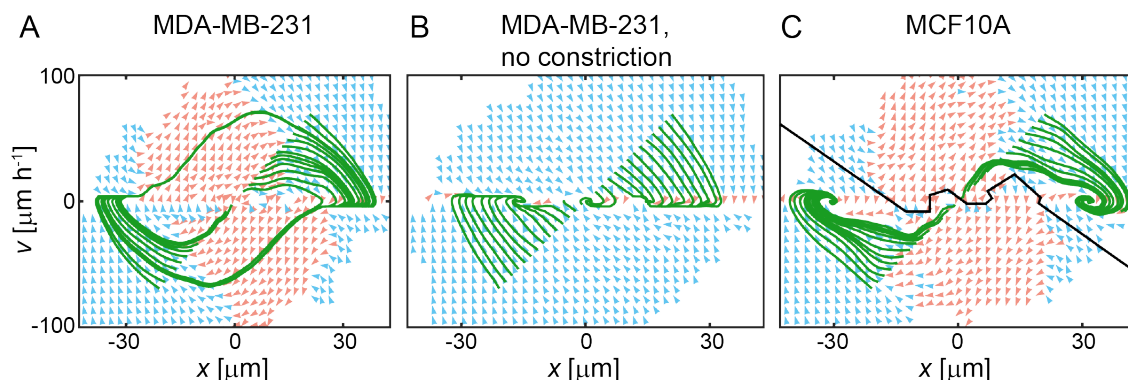
Figure 3.7.: Flowfields of the deterministic component $F(x, v)$ and deterministic trajectories within these flowfields. Blue arrows denote deceleration, orange arrows show acceleration. **A**: All trajectories in the deterministic flowfield of MDA-MB-231 cells on two-state micropatterns collapse onto the same curve and thereby describe a limit cycle. **B**: All deterministic trajectories for MDA-MB-231 cells on a rectangle collapse onto the same line of fixed points at $v = 0$. **C**: Trajectories for MCF10A cells collapse on either of the two fixed points situated on both adhesion sites. The black line is the separatrix showing the boundaries of the basins of attraction of the respective fixed points. Figure adapted and modified from published version in Brückner et al.[1].

The black line in Fig. 3.7 C denotes the border between the basins of attraction for each fixed point. As the basins of attraction for each fixed point reach well onto the other side of the micropattern, a small perturbation by noise can result in the cell transitioning towards the other fixed point. Strikingly, for both cell lines, the transitions we observe are encoded in the deterministic dynamics of the cells. In the absence of a constriction, MDA-MB-231 cells always relax at $v = 0$ (Fig. 3.7 B).

3.4. The Bridge Width Alters the Deterministic Dynamics

In the previous sections, it was shown that the bridge mediates the transition dynamics of cell migration in two-state micropatterns. In particular, the dwell times $\langle \tau \rangle$ scale with the length of the bridge (see Chapter 3.2) and we found a marked difference in cell dynamics between two-state systems with a thin constriction and in the absence thereof (see Chapter 3.3). Furthermore, we observed distinct dynamics of cancerous and non-cancerous cell lines. Mechanical differences have been

reported before; generally, cancer cells are softer than their non-cancerous counterparts[124,125]. Thus, a link between cell deformability and the dynamics could exist. As cells have to deform for their transit over the bridge, we hypothesise that the bridge width w will affect transition dynamics. It remains to be seen at what bridge width the observed dynamics of limit-cycle oscillations changes into a dynamics that relaxes at $v = 0$. To this end, additional two-state micropatterns with a fixed bridge length $L \approx 37$ µm but with varying widths $w = 3.5, 12.1, 18.5$ µm are created.

For all bridge widths, MDA-MB-231 cells transition repeatedly back and forth between the two adhesion sites (Fig. 3.8 (i-iv), and Fig. 3.9 A) and spread and explore the micropatterns. As expected, lamellipodial widths during the growth process within the channel are different (compare, for example, Fig. 3.8 (i) at 420 min, (ii) at 150 min, (iii) at 160 min and (iv) at 190 min). The wider the channel, the more continuous the back and forth motion: On wider bridges, cells can start their transitions to the neighbouring adhesion site as soon as the lamellipodium has reached the other site (Fig. 3.8 (iii) 110 min and (iv) 80 min). In contrast, there is usually some lag time between the lamellipodium reaching the unoccupied island and the onset of a transition for narrower bridge widths. In the presence of a constriction, all trajectories have similar traits (Fig. 3.9 A). Generally, they are characterised by stays of stochastic length on the adhesion sites without any net displacement of the cell nucleus, and abrupt transitions between the two adhesion sites. Interestingly, it seems as though the trajectories become more irregular for the largest used bridge width.

Note that without a constriction, or in other words on a rectangular island, "adhesion sites" and "dwell times" are not well defined anymore. Therefore, for rectangular stripes without a bridge, cells that did not perform at least three transitions (data inclusion criterion 3, Appendix A.2.2) were nevertheless included in the data analysis. In most cases, cells on rectangular stripes perform a back and forth motion, while in some cases cells move more erratically (Fig. 3.9 A). The survival probability functions $S(t)$ for bridges of 3.5 µm and 7.2 µm widths show a prominent plateau for small bridge widths (Fig. 3.9 B, red and black curves) and the long-timescale behaviour is very similar. Also, the behaviour of $S(t)$ for bridges of $w = 12.1$ µm and $w = 18.5$ µm width is alike (Fig. 3.9 B, blue and green curves). These similarities are reflected in the mean dwell times $\langle \tau \rangle$ as can be seen in Fig. 3.9 C. Interestingly, $\langle \tau \rangle$ does not seem to decrease linearly with increasing bridge widths. There is a
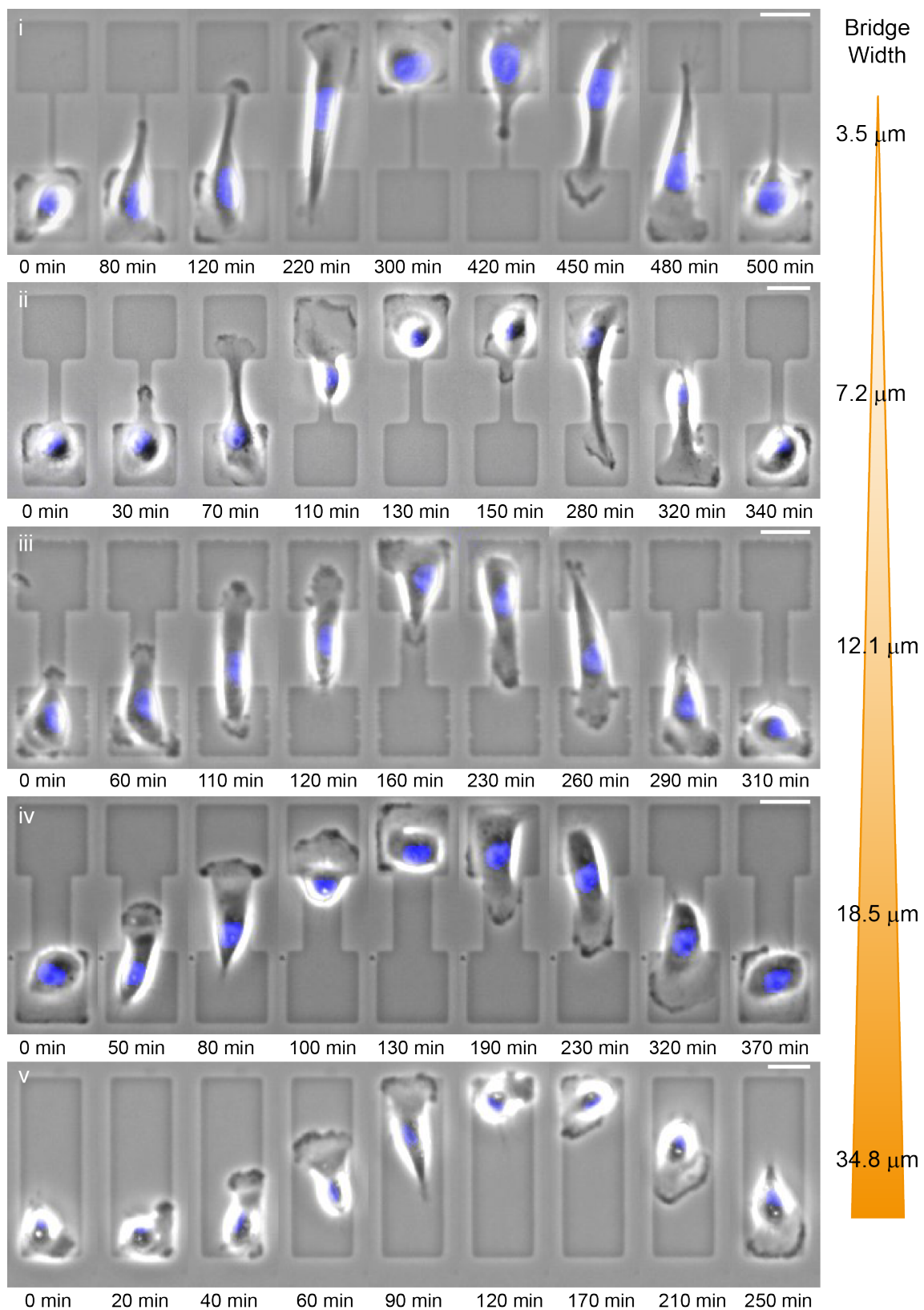
Figure 3.8.: Timeseries of single MDA-MB-231 cells on two-state patterns with different bridge widths w, and without constriction (v). Scale bars: 25 µm.
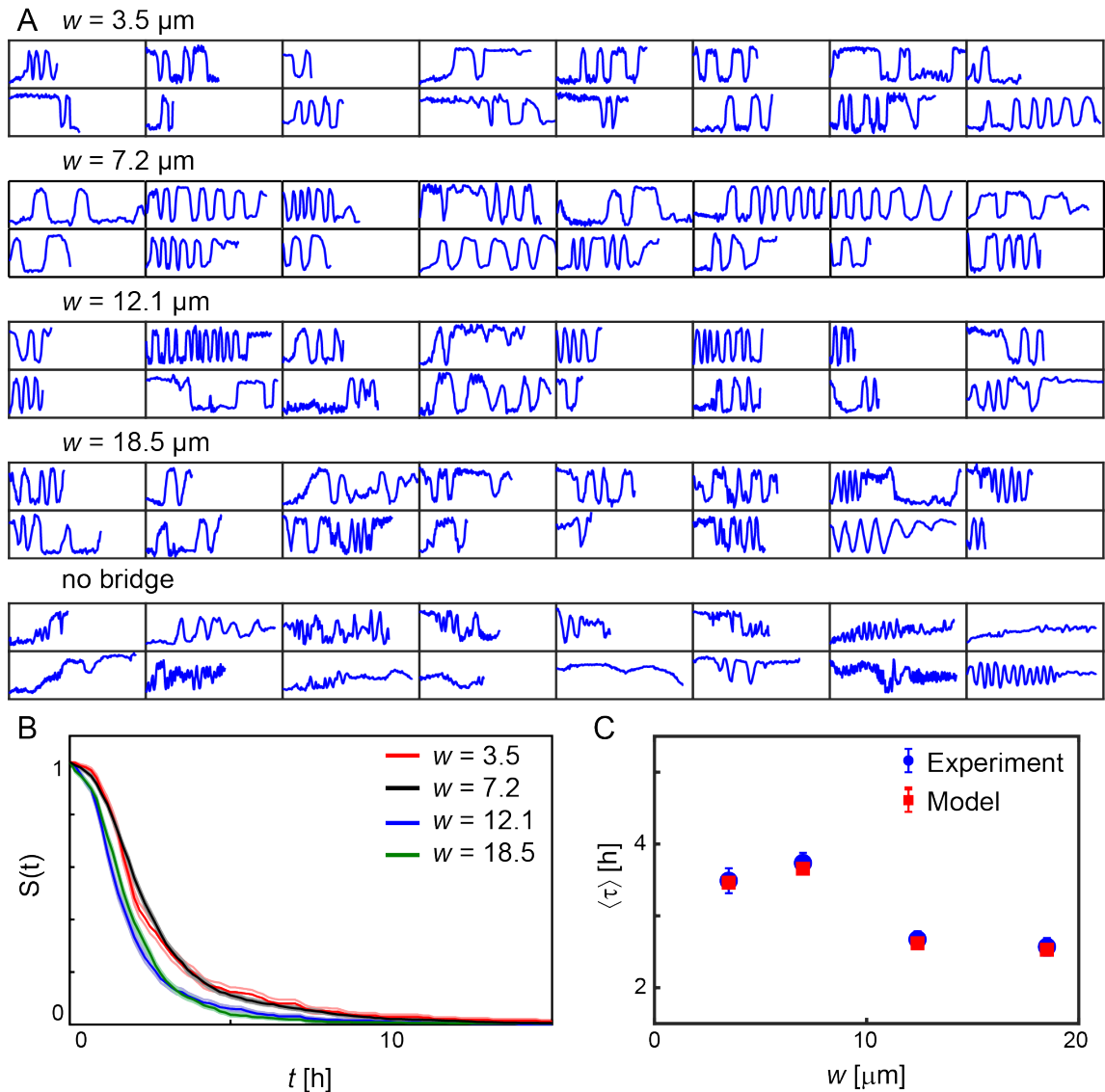
Figure 3.9.: Cell trajectories and transition dynamics on two-state micropatterns with different bridge widths *w*. **A**: Randomly selected sample cell trajectories in systems with different bridge widths *w*, and without a bridge (i.e. on the rectangular stripe). The *x*-axis corresponds to 50 h, the *y*-axis is centred at $y = 0$ and corresponds to 110 μm. **B**: Survival probability functions *S(t)* of dwell times for different bridge widths *w*. The lightly coloured lines denote bootstrapping errors. *w* are given in μm. **C**: Mean dwell times $\langle\tau\rangle$ plotted against bridge widths *w*. The experimental data (blue data points) is compared to the model predictions (red squares). Errors are bootstrapping errors. Plot courtesy of D. Brückner.

good agreement between experimentally determined dwell times (blue data points) and model predictions (red squares, Fig. 3.9 C), indicating that the previously developed framework (see Chapter 3.3) captures the essential features of the dynamics in two-state systems with variable bridge widths.

Specifically, we observe bistable behaviour of the deterministic dynamics for all newly designed two-state micropatterns with bridges of width $w = 3.5, 12.1, 18.5\,\mu m$ (Fig. 3.10). This is unexpected, as we found earlier that for an intermediate bridge width of $w = 7.2\,\mu m$ MDA-MB-231 cells perform limit cycle oscillations (compare Chapter 3.3, Fig. 3.7 A, Fig. 3.10) and that in the absence of a constriction all deterministic trajectories converge on a line of fixed points at $v = 0$ (Fig. 3.7 B, 3.10). Fig. 3.10 also shows that the extent of regions of acceleration (orange arrows) in the flow fields decreases with increasing bridge length, so that in the case of the rectangular stripe, acceleration only occurs around $v = 0$. In light of these distinct deterministic dynamics, the bridge widths at which transitions between the dynamic regimes occur remain to be identified.

3.5. Discussion

In this chapter, the repeated transitions of single cells of various cell lines in two-state micropatterns with varying bridge lengths and widths are described. In particular, cell lines originating from different species (human and dog), as well as being associated with different diseases and of different invasiveness perform these transitions. While the migratory response of MDA-MB-231 and MCF10A cells is extensively characterised, for a selection of other cell lines, no sufficient statistics could be gathered for several reasons. For some of the tested cell lines shown in Fig. 3.4, confinement was not generally sufficient and cells, or their protrusions, frequently entered the passivated areas. This is altogether important as we aim to create controlled cellular interactions with adhesion sites of defined areas and composition. If confinement is not given, several parameters are not well defined. For a few of the screened cell lines, the transition statistics obtained with the used setup is not sufficient: While MCF10A cells (Fig. 3.4 A) readily transition between the adhesion sites, a single transition of A549 (Fig. 3.4 C) and HuH7 cells (Fig. 3.4 D) takes much longer. Obviously, mean dwell times vary and have a broad distribution
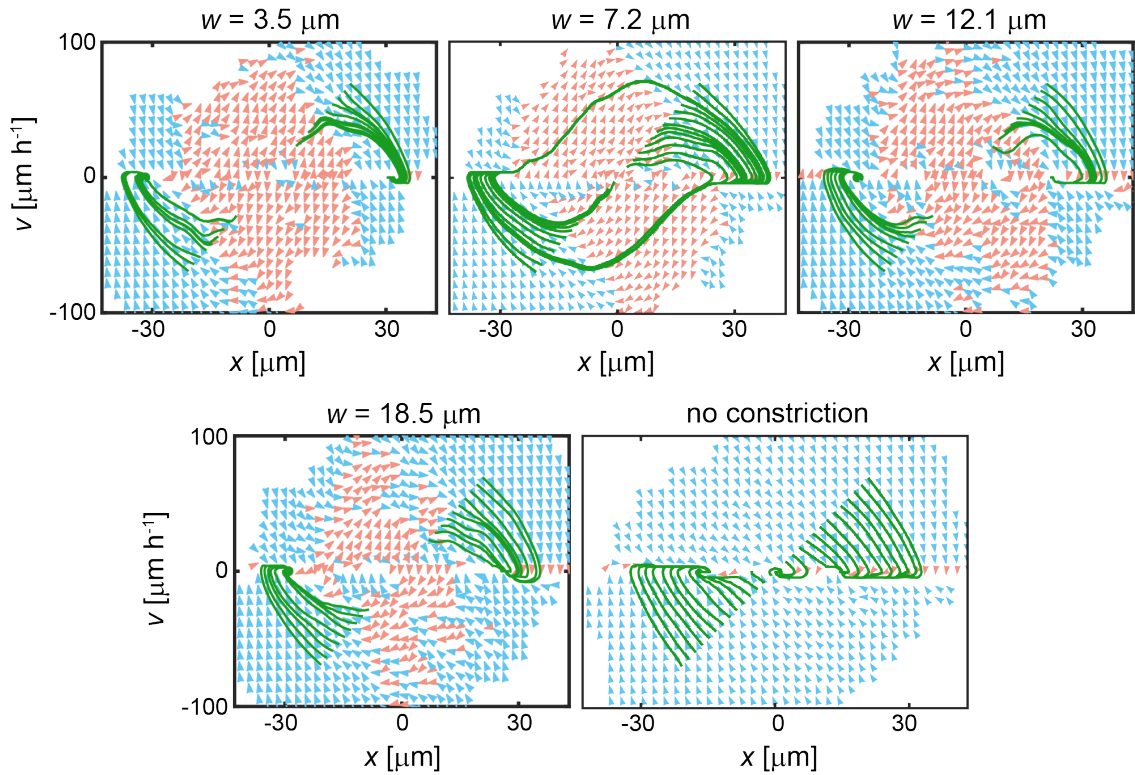
Figure 3.10.: Flowfields of the deterministic dynamics of MDA-MB-231 cells for different bridge widths w, and on the rectangular stripe (i.e. with no constriction). Orange arrows denote areas of acceleration, blue arrows denote areas of deceleration. The green trajectories are initialised for different starting conditions. For $w = 3.5, 12.1, 18.5\,\mu\text{m}$ the deterministic trajectories converge in fixed points located on the adhesion sites. Flowfields for $w = 7.2\,\mu\text{m}$ and no constriction are reproduced from Fig. 3.7. Plots courtesy of D. Brückner.

(compare Fig. 3.3 D) so that a single timeseries does not represent the whole cell population, but it is well capable of depicting a trend. As already mentioned in Chapter 3, both MDCK and A549 cells seem to significantly extend into z-direction, as they are surrounded by a white halo (Fig. 3.4 B and C). This potentially implies that the fibronectin-coated surface does not support cell spreading for these cell lines, or that the dimensions of the used adhesion sites are not suitable. However, as many of these cell lines were previously successfully confined and their migration analysed[47,126], tuning experimental parameters such as pattern dimensions, surface adhesiveness and grade of passivation of the surroundings, might enable their study.

Cellular characteristics underlying the variability observed in the trajectories need further inspection. Clearly, heterogeneity is an intrinsic property of cell cultures[127,128] and several (sub-)cellular processes, such as protein level dynamics[129] and gene expression[130], are highly variable. Could the cell transition dynamics be related to cell size or is the variability caused by heterogeneity in gene expression? It is likely that both parameters are linked, as it has been shown that molecularly different HeLa cells have different morphologies[127]. Cell size has previously been identified as a determinant of migration speed[131,132]. Also, the intrinsic requirements for experiments as posed by the data analysis and data reproducibility, necessitate that several independent experiments are performed. Sometimes, in a series of similar experiments, different subsamples of the original cell sample obtained from the cell bank were used. All this increases the likelihood that cells with variable gene expression are probed in the experiments. In contrast, ensemble-averaged quantities profit from the repeated observations as the influence of experimental day-to-day-variations can be reduced by averaging over several experiments.

We found that a nonlinear stochastic equation of motion describes the dynamics of cancerous MDA-MB-231 and less invasive MCF10A cells in confinement to both, two-state patterns and on a stripe with similar dimensions (Fig. 3.6). This constitutes a novel finding. The range of models previously used for the description of cell motion spans from cell-type dependent models of varying complexity[20] for cells migrating on homogeneous 2D substrates to models that incorporate a switching between modes of migration[19,47]. Frequently, the language of energy potentials is used[108,133–135]. In particular, the Cellular Potts Model has been successfully utilised to model cell spreading on micropatterns[36,136], periodic migration of cells on stripes[111] and to capture collective rotational motion[126]. While it seems intuitive,

and would be in line with other ansatzes, we have ruled out the description of a cell in a two-state pattern as a Brownian particle in a double-well potential with a constant noise strength and uncorrelated, time-dependent noise (see Supplementary Information (SI) of Brückner et al.[1]). Nonetheless, it is likely that other models are able to describe and predict the observed motion.

On two-state micropatterns with a bridge of $w = 7.2\,\mu m$, the deterministic dynamics of MDA-MB-231 cells encodes limit-cycle oscillations and MCF10A cells have a deterministic driving to transition to the neighbouring adhesion site. In the presence of noise, these transitions happen in a repeated manner (Fig. 3.7). In biology, oscillations in cells are widespread. For example, hair bundles can oscillate spontaneously[137], cytoskeletal components in Dictyostelium cells were found to oscillate[138], lamellipodia exhibit periodic contractions[88] and cell nuclei oscillate in cells immobilised on stripe micropatterns[139]. Only in recent years however, oscillatory and near-periodic migration of cells have been theoretically predicted and experimentally observed. In particular, zyxin-depleted cells embedded in a 3D matrix environment performed a one-dimensional oscillatory motion. Interestingly, when plated on 2D substrates, the same cells' motion looked like a random walk. In contrast, on 1D micropatterned stripe, a periodic motion similar to that within the matrix could be reproduced[140]. A theoretical phase-field model coupling actin and myosin localisation predicts the emergence of periodic motion in cells confined to stripes[110]. This has been recently experimentally confirmed when MDA-MB-231 cells seeded on stripe micropatterns exhibited quasi-periodic motion[111].

For MDA-MB-231 cells, we investigated the role of the constriction more closely by varying the bridge width w. In detail, we find that the bridge width modulates the deterministic dynamics of the transitions, which includes bistable behaviour for bridges of width $w = 3.5\,\mu m$, limit-cycle oscillations for bridges of $7.2\,\mu m$ width, another region of bistability for bridges of $12.1\,\mu m$ and $18.5\,\mu m$, and a stable mannifold on rectangular stripes. While the mean dwell times in these setups do not seem to be linearly correlated with the bridge widths, they are lower for increasing w. Dwell times that decrease with increasing bridge widths (Fig. 3.9 C) are intuitively understandable, as wider bridges impose less of a hindrance to cells migrating from the wide adhesion sites onto the bridge (compare also Fig. 3.8). Additionally, it was recently demonstrated that the available adhesive area determines the growth and reinforcement of cellular protrusions. In particular, the existence of a minimum

adhesion nucleation area needed to stably anchor protrusions was reported[141]. It is therefore possible that the waiting times for the establishment of a sufficient adhesion area necessary for cell locomotion are longer on narrower bridges. Surprisingly, we find that limit cycle dynamics are so far restricted to an intermediate bridge width of 7.2 µm. While for the smallest bridge width (3.5 µm) the bridge constitutes a considerable obstacle to repeated transitions between the adhesion sites, it is less clear why we observe bistable behaviour for the other two tested bridge widths (Fig. 3.10). It is possible that the 12.1 µm and 18.5 µm wide bridges are too wide for quick cell transitions during limit-cycle oscillations: The lamellipodia are less confined in their growth while on the bridge, and therefore might grow less efficient into the direction of the other adhesion site, and also cells can establish more adhesions with the substrate. A less efficient confinement of cells and their protrusions could also be the reason for the higher phenomenological variability of trajectories for wider bridges. Previously, a biphasic dependence of cell migration velocity on the width of micropatterned stripes was reported. For fibroblasts migrating on stripes, Doyle et al. observed a peak in velocity for an intermediate stripe width, and attributed the lower velocities for narrower and wider stripes to less efficient adhesions and less efficient confinement, respectively[142]. Inefficient adhesion formation on very thin lines has also been suggested by other authors. However, the same authors report results contradicting Doyle's findings on wide stripes, reporting quicker and more persistent cell motion[132,143]. As in all these studies different cell types were utilised, it is possible that the effect of wide stripes on cell migration is cell-type specific.

On rectangular stripes in the absence of a constriction, the cellular dynamics relaxes onto a line of fixed points at $v = 0$. Intuitively, in the absence of a bridge, a migrating cell can stop in any place, which is a behaviour consistent with the previously reported persistent random walk on stripes[46,111]. Also, the observed dynamics could be a superposition of a variety of other dynamic behaviours. In particular, a wide range of cell migration phenomena on stripes effectively confining cells to one dimension was found previously, namely two-state motion[47], quasi-periodic motion[111], oscillations[140] as well as crawling and turning[110].

The bridge constitutes a geometrical constriction in the two-state system. Specifically, the trajectories are characterised by near-stationary states while the cell is located on the adhesion sites, and abrupt transitions between the sites (Fig. 3.3 and Fig. 3.9). During their stays on an adhesive motif, cells de- and repolarise fol-

lowing a transition onto the island, transiently polarise, grow a protrusion on the bridge, and typically initiate a transition once the lamellipodial tip has reached the neighbouring adhesion site (Fig. 3.2 and Fig. 3.8). Hence, the spread of the probability distribution of dwell times (Fig. 3.3 D, Fig. 3.5 B, Fig. 3.9 C) is caused by the stochasticity of several processes. Recently, Zhou et al. reported a mean de- and repolarisation time of 100 min for MDA-MB-231 cells reversing repeatedly on stripes with blunt ends[111], which is smaller than the mean dwell times observed on any of the two-state geometries (Fig. 3.5 B, Fig. 3.9 C). This further supports the notion that the bridge acts as a constriction on the motion of migrating cells. Also, cells visibly round up their rear during the bridge passage (Fig. 3.2 A, Fig. 3.5). And additionally, the area surrounding the bridge is associated with higher noise and deceleration (Fig. 3.6 A, C). In contrast, while cellular transitions between adhesion sites separated by a cell-repellent surface also occur in the absence of a connecting stripe[47,49,103,144], the stripe also acts as an important guidance cue for membrane ruffles (Fig. 3.2 A, Fig. 3.8). Furthermore, cells are accelerated on the bridge (Fig. 3.6 A, C, E and Fig. 3.10), with no such areas of acceleration visible for cells confined to a rectangular stripe in the absence of the bridge 3.6 B, E). In other words, the bridge promotes efficient protrusion growth by providing guidance and confinement, which seems to be a pre-requisite for a deterministic driving to transition between the adhesion sites.

4. The Geometry and Orientation of Adhesion Sites Bias Cell Migration

In Chapter 3, the behaviour of MDA-MB-231 cells and other cell lines on two-state micropatterns was described. In particular, it was shown that the bridge modulates the deterministic dynamics of MDA-MB-231 cells. While the bridge acts as both, constriction and guidance cue, it is unclear how the geometry of the adhesion sites influences the migratory response of cells in the two-state micropatterns. This chapter aims to characterise the migration behaviour with respect to adhesion site geometry.

The results presented here were published in [P2].

4.1. Dwell Times Increase with Increasing Adhesion Site Area

To test the influence of adhesion site geometry on cell migration behaviour in the two-state patterns, the symmetry of the system is gradually and systematically changed. As a first step, the size of the adhesion sites is altered, while their quadratic shape and a constant bridge length and width are maintained. Thus, we varied the square edge length a (compare Fig. 3.1) from 27.3 ± 0.4 µm to 42.2 ± 0.5 µm. A limit for adhesion site sizes was found for edge lengths smaller than approximately 25 µm. In this case, cells do not fully fit onto the small adhesion sites and, in their transitions, do not comply with the cell exclusion criteria (compare Appendix A.2.2) applied during data analysis.

Generally, cell behaviour on these newly designed dumbbells does not vary from that observed on symmetric dumbbells (as depicted in Fig. 3.2): Cells form membrane ruffles while exploring the adhesion site, and within the channel, protrusions can grow into mature lamellipodia. Usually, a lamellipodium reaching the opposite, unoccupied site is a safe indicator for a subsequent transition. Cells then repeatedly transition between the adhesion sites. When plotting a histogram of nuclear positions

on the used geometries (Fig 4.1 A), an asymmetry is visible. This asymmetry contrasts with the symmetric distribution observed for two-state patterns with equally sized adhesive squares (4.1 A(iii)). The mean dwell times $\langle\tau\rangle$ on the adhesive squares scale almost linearly with adhesion site area (Fig. 4.1 B). Only for large adhesion sites, the data deviate from the linear trend indicated by the dashed line. It seems as though the data saturates. Importantly, the data points from different combinations of adhesion site areas agree within errors, indicating that no memory effects are relevant in this particular setup.

While occupancies p_i are an end-point readout, and a static quantity, they can be connected to the dynamic quantity of mean dwell times as follows:

$$p_i = \frac{\sum_i \tau_i}{T_{tot}} = \frac{N_i \langle \tau_i \rangle}{T_{tot}} \tag{4.1}$$

with $i = \{small, large\}$, p_i the occupation probability, $\langle\tau_i\rangle$ the mean dwell time, N_i the total number of stays on site i and T_{tot} the total observation time.

Thus, the ratio of occupation probabilities p_i/p_j becomes

$$\frac{p_i}{p_j} = \frac{N_i \langle \tau_i \rangle}{N_j \langle \tau_j \rangle} \approx \frac{\langle \tau_i \rangle}{\langle \tau_j \rangle} \tag{4.2}$$

with the last equality holding for $N_i \approx N_j$.

The ratio of mean dwell times on both adhesion sites, $\frac{\langle\tau_{small}\rangle}{\langle\tau_{large}\rangle}$ follows a linear trend when plotted against the area ratio of the respective adhesion sites, $\frac{A_{small}}{A_{large}}$ (Fig. 4.1 C). Again, the strongest deviation from the linear trend, marked by the dashed line, is observed for data from the largest used adhesion sites. This leads to the question whether cells do not usually fully cover the largest tested adhesion sites. Interestingly, we find that already for adhesion sites larger than $\approx 1250\ \mu m^2$ the mean cell area does not increase as much as the adhesion site area (Fig. 4.1 D). However, as MDA-MB-231 cells have a large size distribution, this is true only on average. Also, cells grow over time, so that cells that are smaller than the adhesion site initially, can grow over time to fully fill it. However, it has to be emphasized that the linear relationship we find between mean dwell times $\langle\tau\rangle$ and adhesion site areas A_{ad} can only partially be explained with cell (adhesive) area. As MDA-MB-231 cells are highly motile, the spreading within and the exploration of the adhesion site certainly contribute to the dwell times.
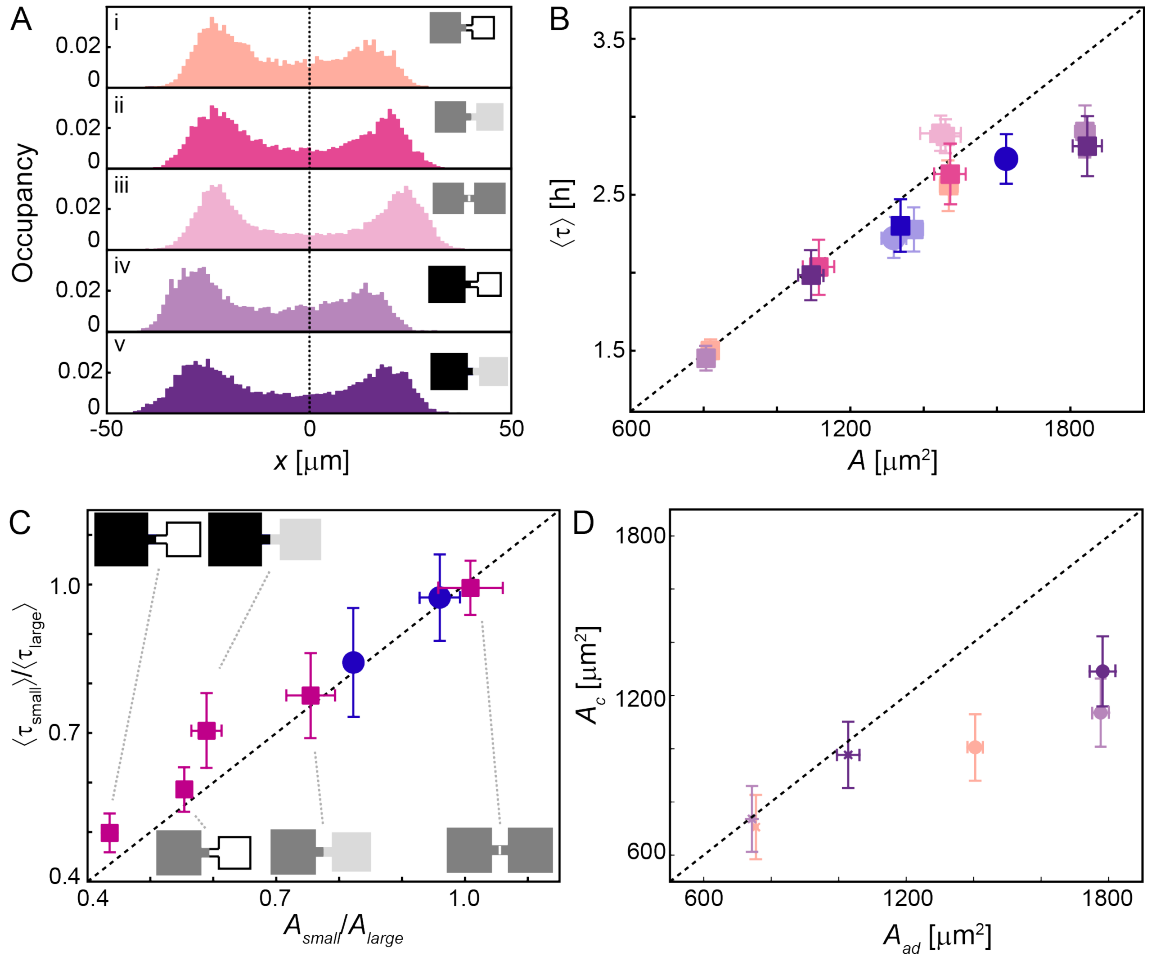
Figure 4.1.: Occupation probabilities and mean dwell times on square adhesion sites of different areas. **A**: Occupation probabilities along the long axis of the micropattern. (iii) corresponds to the symmetric setup as presented in Chapter 3. The occupation probabilities reflect the asymmetry of the underlying micropattern. **B**: Mean dwell times $\langle\tau\rangle$ plotted against adhesion site area A with the same colour code as in **A**. Blue data points correspond to square-circle micropatterns with adhesion sites of either equal area or equal perimeter. The dashed line is a guide to the eye. Errors in x are weighted standard deviations and errors in y are bootstrapping errors. **C**: The ratio of mean dwell times plotted against the ratio of corresponding adhesion site areas. Pink data points correspond to square-square micropatterns and blue data points to square-circle micropatterns. The dashed line is a guide to the eye. Errors in x are weighted standard deviations and errors in y are bootstrapping errors. **D**: Plot of cell area A_c against adhesion site area A_{ad} for selected combinations of square sizes. The colour code is the same as in panels **A** and **B**. The dashed line is a guide to the eye. Errors in x are weighted standard deviations and errors in y are bootstrapping errors. Figure adapted and modified from published version and its SI in Fink et al.[2].

As for symmetric dumbbells, we can train the previously introduced model (see Chapter 3.3) on 50% of the experimental data to probe its predictive capabilities for the asymmetric system. For all two-state patterns with differently sized adhesion sites the agreement between model prediction and experimental data is good, as can be seen in Fig. 4.2 C. Again, the phase space maps are instructive. The deterministic dynamics, Fig. 4.2 A, shows that the cells are mostly decelerated on the adhesion sites, unless their velocities lie within a small interval of velocities. When cells transition from the large to the small adhesion site with a high velocity, they are strongly decelerated. In contrast, no equally strong deceleration is visible for transitions from the small to the large adhesion site. The regions of acceleration within the channel are not as strongly evident as in the symmetric case (compare Fig. 3.6 A). Similarly, the noisiest regions of $\sigma(x,v)$ do not extend significantly into the channel. The noise level is highest just next to the bridge (Fig. 4.2 B).

4.2. Anisotropic Shapes Bias Occupation Probabilities

In the next step, the rotational symmetry of the adhesion sites is changed, and the migratory response to circular, rhombical and triangular adhesion sites of approximately the same area is studied. While cells form uniform membrane ruffles along their periphery while spread on circular adhesion sites, cells on rhombical and triangular sites preferentially form protrusions in the corners (Fig. 4.3 A). The occupation probabilities on squares and circles of equal areas do not differ, while rhombical adhesion sites introduce a small bias. Cells spend a significantly longer time on the tested triangular adhesion sites than on square sites of approximately the same size (Fig. 4.3 B). The different response to the probed adhesion sites is partially due to the extent of cell motion into the y-direction, i.e. perpendicular to the axis of transitions. Thus, the 2D occupation probability distributions, which are shown in Fig. 4.3 C, in square-circle and square-rhombus patterns look very similar. However, on the triangle, cell positions are much more scattered than on any of the other geometries.

Square-circle micropatterns in particular allow to probe cellular response to adhesion sites of either equal area or equal perimeter. When the mean dwell times $\langle \tau \rangle$ on both setups are included in the $\langle \tau \rangle$-A_{ad}- and dwell-time ratio versus adhesion-site-area
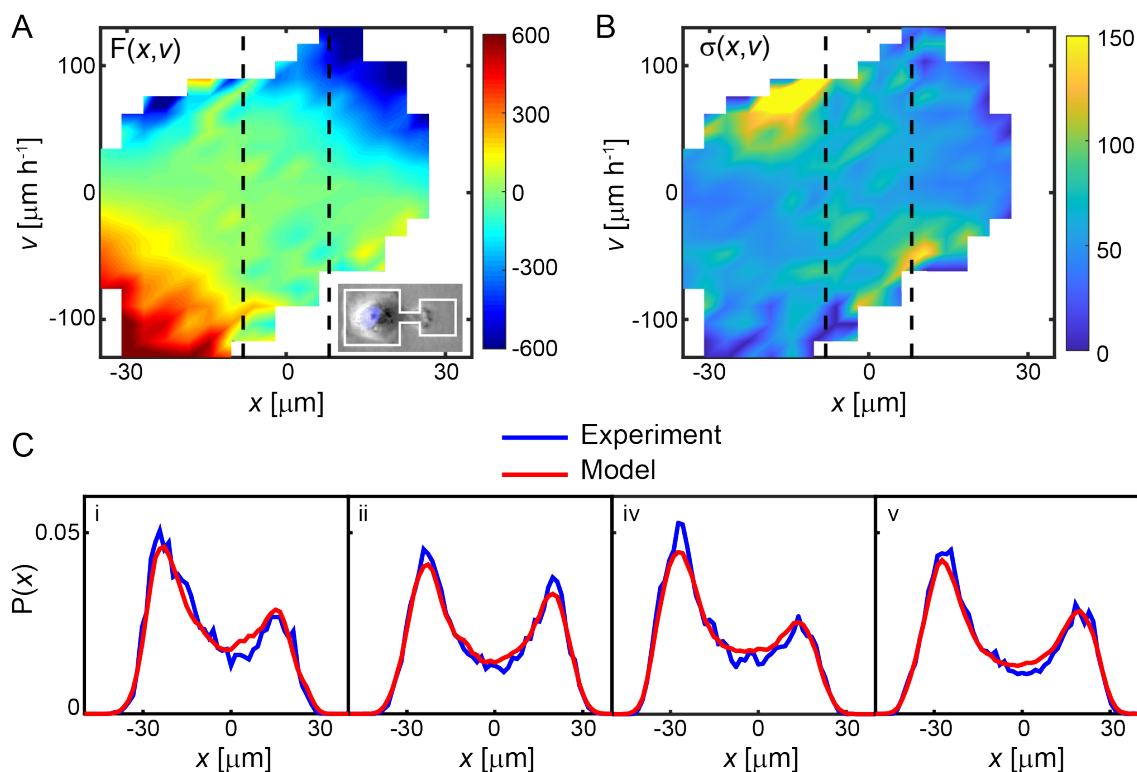
Figure 4.2.: Stochastic nonlinear dynamics of MDA-MB-231 cells in two-state micropatterns with different adhesion site areas. Here, the left square adhesion site has an edge length a of 42.1 μm and the right square adhesion site has an edge length a of 27.3 μm. The bridge length is $L = 16$ μm. **A**: Phase space map of the deterministic component $F(x, v)$ of the cellular dynamics. The dashed lines indicate the boundaries of the bridge. **B**: Phase space map of the stochastic component $\sigma(x, v)$ of the cellular dynamics, with the black dashed lines indicating the boundaries of the bridge. **C**: Comparison between experimental occupation probabilities (blue) and model predictions (red) for all tested dumbbell-like micropatterns with unequally sized adhesion sites. The numbering corresponds to the numbering in Fig. 4.1 A. Figure adapted and modified from published version and its SI in Fink et al.[2].

ratio plots in Fig. 4.1 B and C, respectively, the data points follow the same trend as data points from square adhesion sites.
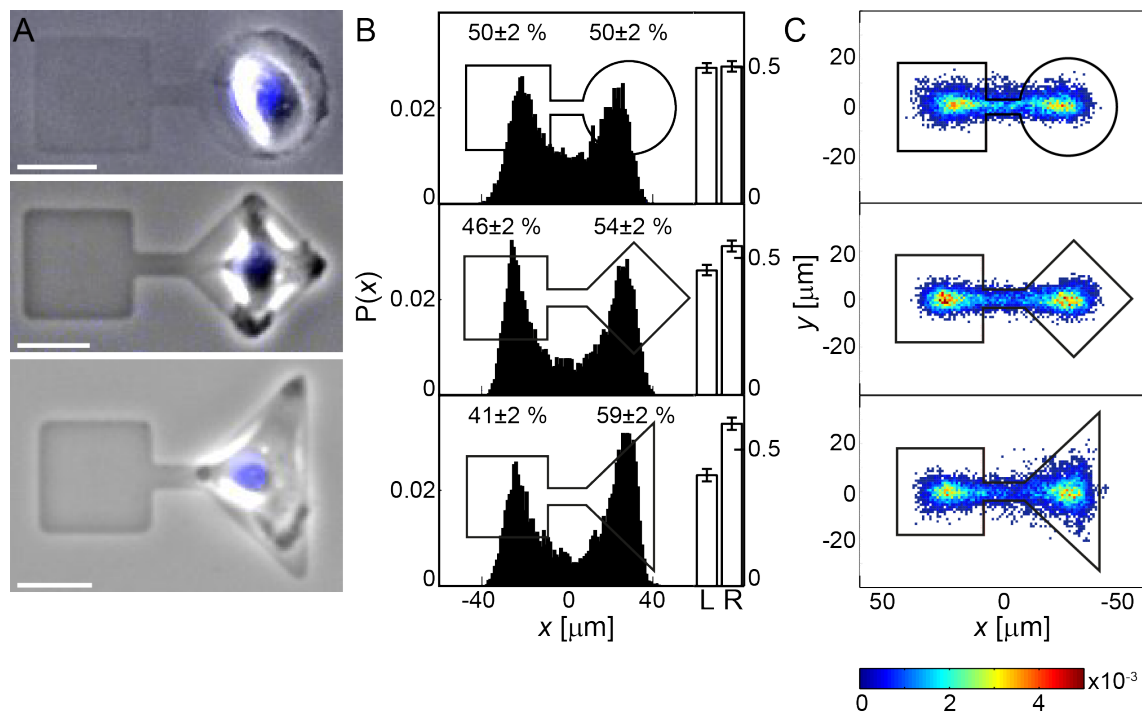

Figure 4.3.: Occupation probabilities on micropatterns with adhesion sites of different shapes. **A**: Single cells spreading on differently shaped adhesion sites of approximately equal areas. Membrane ruffles, visible as dark regions, are preferentially localised in corners. Scale bar: 25 µm. **B**: Corresponding occupation probabilities. The percentages given are normalised by adhesion site area to account for differences in the areas: While the patterns were designed to have adhesion sites of equal area, due to the manufacturing process, the final protein patterns have slightly different adhesion site areas. Errors are bootstrapping errors. **C**: Two-dimensional occupation probabilities on the respective micropatterns. Figure adapted and modified from published version in Fink et al.[2].

So far, it seems as though equally sized shapes that are symmetric under 90° rotations only weakly bias occupation probabilities. It is unclear, however, how the orientation of equal anisotropic shapes influences the migration. To this end, we have created rectangular adhesion sites of aspect ratio $\approx 1 : 2$ with different relative orientations: Either both rectangles face in the same direction, being both vertically or horizontally oriented, or their main axes are oriented perpendicularly to each other. In line with the previously reported observations, cells exhibit an exploratory behaviour within the adhesion sites and also transition between the adhesion sites.

Mean Dwell Time / Setup	$\langle \tau_\parallel \rangle [h]$	$\langle \tau_\perp \rangle [h]$
symmetric	2.70 ± 0.11	2.79 ± 0.21
mixed	2.67 ± 0.22	3.44 ± 0.32

Table 4.1.: Mean dwell times $\langle \tau \rangle$ on rectangular adhesion sites for the symmetric configuration, where both adhesion sites are equally oriented and the mixed setup, where the rectangles are oriented perpendicular to each other. Compare also Fig. 4.4.

Importantly, during their exploratory or spreading phase, cells are seen to form lamellipodia in the direction of the long rectangle axis, and sometimes migrate within the adhesion sites (Fig. 4.4 A, 0-10 min and 220-230 min). Therefore, the distributions of cell positions in 2D look different on differently oriented rectangles (Fig. 4.4 C). In both setups with equally oriented rectangles, the occupation probabilities on both sides are equal. In the asymmetric, mixed-orientation setup, however, the occupancies are biased towards the upright rectangle (Fig. 4.4 B). The preferential localisation of cells on the vertical rectangle is linked to the escape rates k_i, which are defined as the inverse mean dwell times $\langle \tau \rangle$,

$$k_i = \frac{1}{\langle \tau_i \rangle} \tag{4.3}$$

Figure 4.4 D visualises the distribution of dwell times τ in a plot of the survival probability functions *S(t)*. Different behaviours for the horizontal escape rate, $k_{m\parallel}$, and the vertical rate, $k_{m\perp}$ are apparent. While initially $\tau_{m\perp}$ decay faster, indicating that more cells transition within a short time, the trend reverses for dwell times > 4 h. Hence, in the long term, cells escape quicker from the horizontal rectangle than from the upright rectangle. Most interestingly, *S(t)* behaves very similarly for the respective dwell times for symmetrically orientated rectangles (Fig. 4.4 E) including the exchange of relative positions of both curves. Yet, the difference for long dwell times is much less pronounced than in Fig. 4.4 D. Eventually, these escape dynamics result in very similar mean dwell times for three of the four conditions, as can be seen in Table 4.1. Here, the dwell times on the left and right sites for symmetric combinations of rectangles were pooled to enhance the statistics.

The mechanism leading to different occupancies and escape rates on adhesion sites of equal area but of different orientation is still unclear. Also, it is an open question
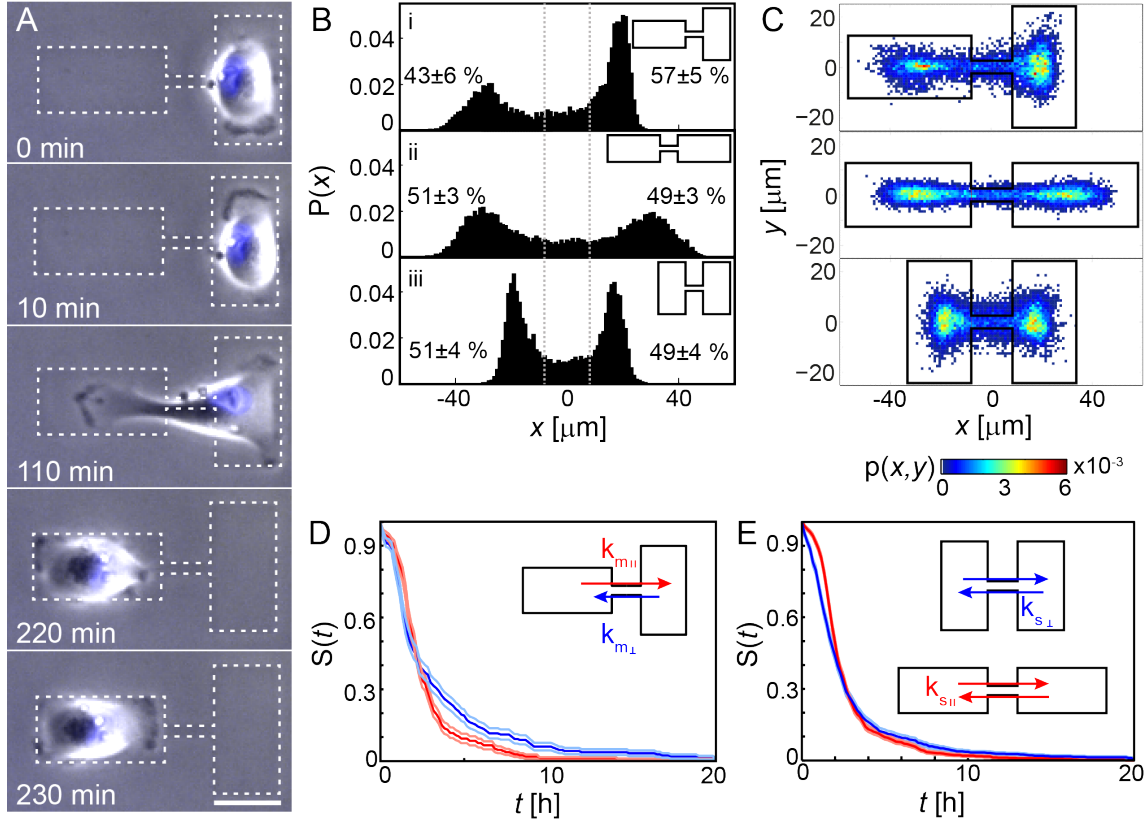
Figure 4.4.: Cell migration on two-state patterns with rectangular adhesion sites of different orientations. **A**: Timeseries of a single cell migrating on a two-state pattern with mixed rectangle orientations. The cell aligns with the long axis of the rectangle. Scale bar: 25 µm. **B**: Occupation probabilities for all setups with rectangular adhesion sites and bridge length $L = 16.2\,\mu\text{m}$. Errors are bootstrapping errors. **C**: 2D occupation probabilities, in the same order as in **B**. **D**: Survival probability functions $S(t)$ of dwell times τ on the adhesion sites in the mixed setup. The lightly coloured lines indicate bootstrapping errors. **E**: $S(t)$ for dwell times τ on the adhesion sites in equally oriented adhesion sites. Dwell times on the left and right adhesion sites are grouped together to enable the comparison between the different geometries. Bootsrapping errors are shown as lightly coloured lines. Figure adapted and modified from published version in Fink et al. [2].

why the occupancy does not differ for squares and circles of equal area, whereas a pronounced bias is visible for square-triangle systems. To answer these questions, it is instructive to look at the actin dynamics of cells migrating in three representative adhesion site shapes, namely in squares of $\approx 37.2 \times 37.2$ µm^2, in circles with a diameter of ≈ 40.3 µm and in right-angled triangles of the same area. Thus, LifeAct-GFP transfected MDA-MB-231 cells show very similar actin dynamics on squares and circles (Fig. 4.5 (i) and (ii)). In both cases, along the cell periphery a single broad lamellipodium is formed, and actin accumulates in a narrow band all along its leading edge. If present, stress fibres are only faintly visible and typically span all over the cell body. Actin hotspots are frequently visible in square corners. This preferential localisation of hotspots to corners can also be observed on the triangle (Fig. 4.5 (iii)). Here, several hotspots near different corners are visible at the same time. Thus, the protrusion dynamics and potentially cell polarisation are altered by adhesion site shape.

To test whether cell polarisation has a significant effect on cell behaviour within different adhesion sites, we analyse the angular distribution of cell velocities. Fixed cells were stained for their actin and paxillin to gain further insights into the underlying cell organisation (Fig. 4.6). The reason for using fixed rather than live cells is related to the low statistics that can typically be gathered in stained live cell imaging experiments. For medium squares ($\approx 37.2 \times 37.2$ µm^2), small squares ($\approx 27.5 \times 27.5$ µm^2), circles of similar area to the medium squares and rhombi of similar area, the angular distributions of the directions of cell velocities look very similar: Cell motion within the adhesion sites seems to primarily take place in the direction of transitions. Motion perpendicular to that axis is infrequent. Interestingly, the most striking difference in the angular distributions appears to be related to the side the channel meets the adhesion site. While the distributions for small square, circle and rhombus look almost identical, the distribution for medium squares differs. Thus, cells seem to migrate more frequently along the line defined by the channel when moving away from it and within a broader range of directions when migrating towards the channel. In the case of the triangular adhesion sites, the angular distribution changes distinctively, and migration perpendicular to the axis of transitions becomes more frequent.

In general, the internal cell organisation on the studied geometries does not vary much: Typically, stress fibres are mostly oriented in the direction of migration,

crossing over the cell body. Lamellipodia are characterised by the occurrence of transverse arcs and criss-crossing actin fibres. Focal adhesions are preferentially localised in corners, and accumulate under the leading cell edge. Few focal adhesions are visible at the cell rear. Studying the co-localisation of actin and paxillin in greater detail, as shown in the zoom-in for the circular adhesion site in Fig. 4.7, focal adhesions are co-localised and aligned with the stress fibres crossing the cell body. Also, typically there is a small band at the cell periphery characterised by the presence of actin and by the lack of paxillin.

In conclusion, cells polarise to migrate both between adhesion sites and within adhesion sites, and possibly also as a response to adhesion site shape. However, in the presented analysis it is not possible to distinguish between imposed polarity and polarisation due to actual migration within the adhesion sites. Of the geometries studied so far, the triangle alters the directionality of cell migration the most, introducing a significant amount of motion perpendicular to the main axis of the micropattern. By this, the bias in occupation probabilities may be explained.
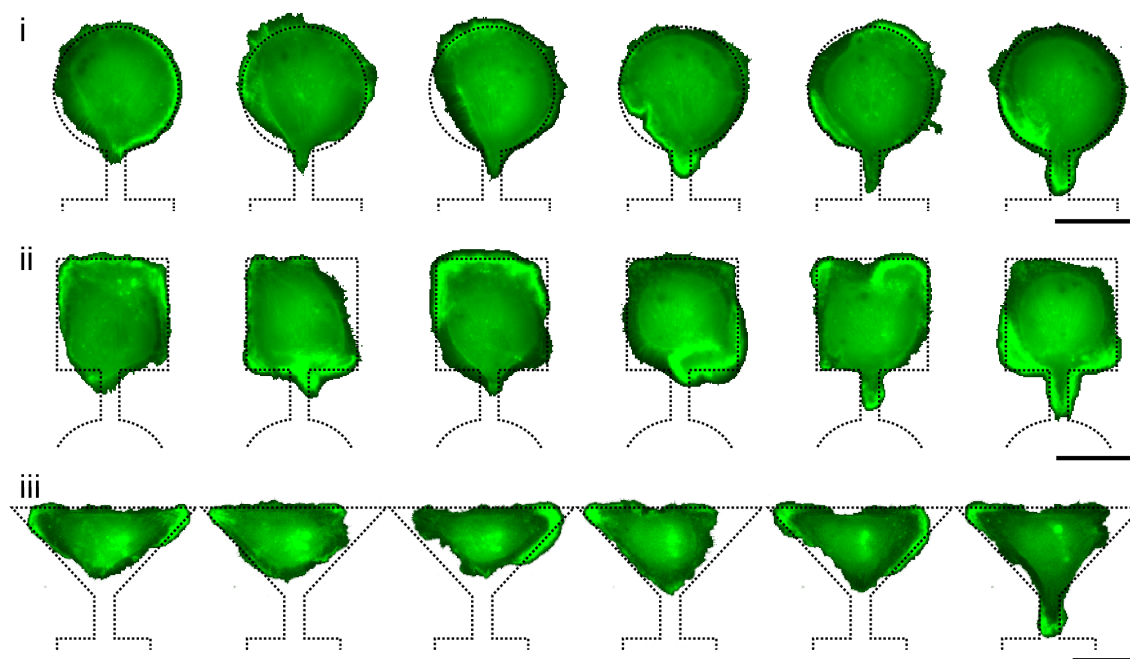

Figure 4.5.: Timeseries of LifeAct-GFP labelled MDA-MB-231 cells spreading on differently shaped adhesion sites. Bright green regions correspond to areas of actin accumulation. The non-fluorescent background was inverted using Adobe Photoshop. Scale bars: 25 µm. Figure reprinted from Fink et al.[2] with author's rights.

The same analysis can also be performed for all setups with rectangular adhesion
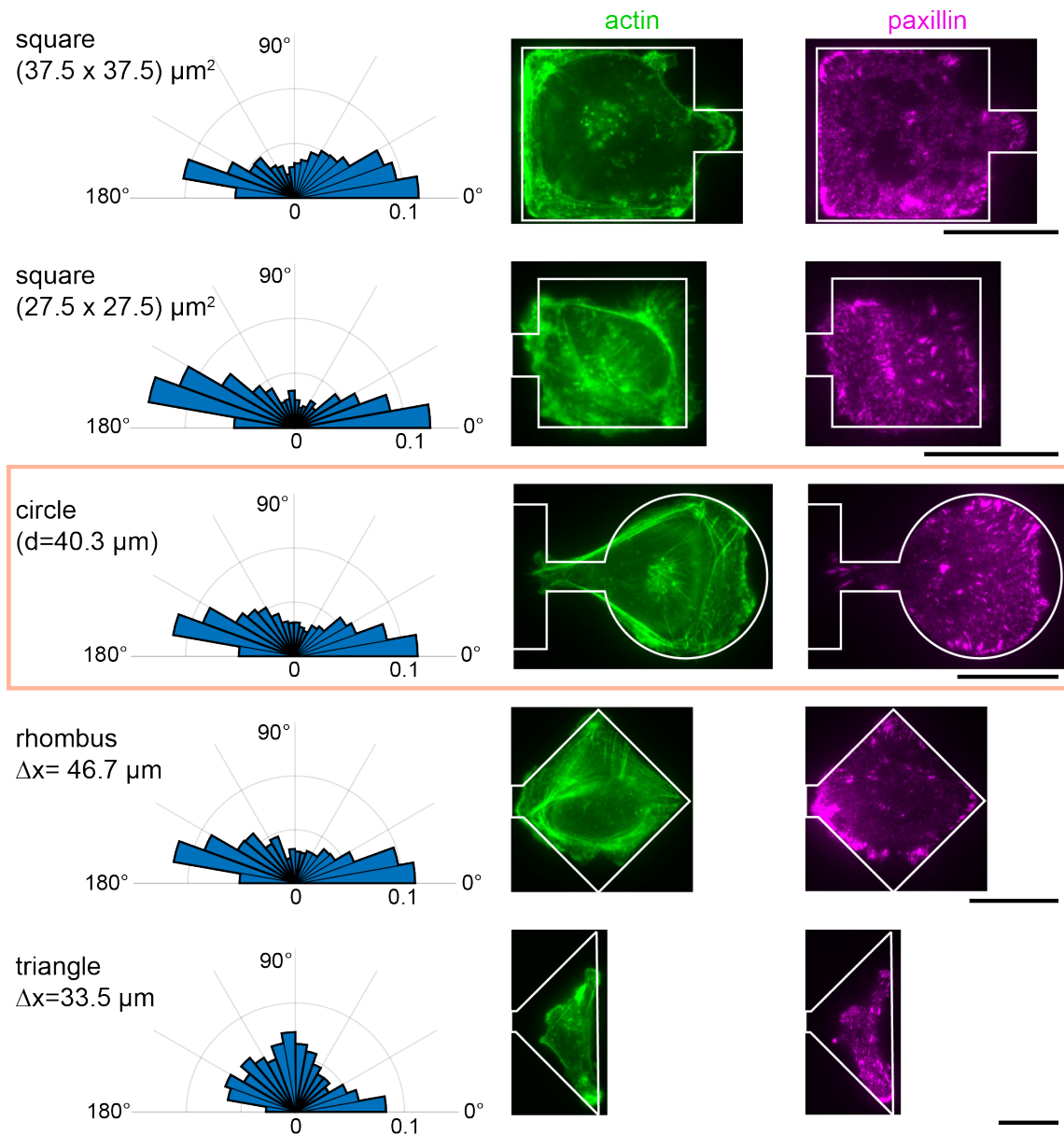
Figure 4.6.: Direction of motion with respect to the long axis of the micropattern on adhesion sites of different geometries. The angular probability distributions of the direction of cell velocities on the adhesion sites are shown. As the scalar product is used for the calculation of angles, each bar gives the frequency of motion in the direction of that angle and in the direction of (angle + 180°). On the right side, images of fixed cells on the respective adhesion sites, stained for actin and paxillin, are shown. Scale bars: 25 μm. Figure is adapted and modified from the SI of Fink et al. [2].
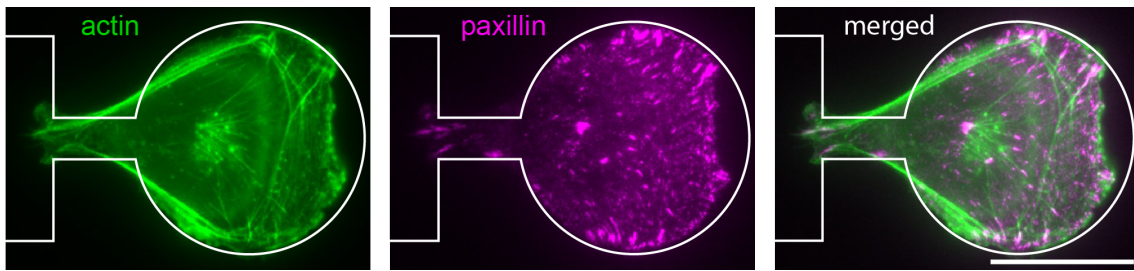
Figure 4.7.: Zoom-in into the fluorescence images of a fixed cell stained for its actin and paxillin on a circular adhesion site. The zoom-in corresponds to the images inside the orange frame shown in Fig. 4.6. In the merged image, the co-localisation of actin stress fibres and focal adhesions is visible. Scale bar: 25 μm.

sites (see Fig. 4.8). In the symmetric cases, the angular distributions on both sites look very similar. For two horizontal rectangles, cell motion is largely aligned with the direction of the long rectangle axis and the axis of transitions. Motion in the y-direction that is not within a ± 30°-interval of the long axis occurs very rarely (Fig. 4.8 (ii)). In contrast, if both rectangles are positioned in an upright manner, with their long axis perpendicular to the axis of transitions, the directions of cell velocities look almost uniformly distributed over the whole [0°, 180°] interval (Fig. 4.8 (iii)). Thus, cells also tend to migrate along the long rectangle axis. Interestingly, in the mixed setup as shown in Fig. 4.8 (i), the distribution on the upright rectangle differs from those in the symmetric setup. For the horizontal rectangle in the mixed setup, no such difference can be detected. In particular, cell motion in the y-direction seems to be more pronounced on the upright rectangle in the mixed setup.

When the mean dwell times $\langle \tau \rangle$ of every adhesion site from all tested asymmetric micropatterns are plotted against adhesion site areas in the same plot, i.e. in a similar manner as in Fig. 4.1 B, the data points corresponding to stays on the triangle and on the upright rectangle from the mixed setup deviate most from the linear trend observed for data from square-square and square-circle systems (Fig. 4.9). The mixed setup's upright rectangle data point stands out for another reason as well: For all other data, the neighbouring adhesion site's geometry does not seem to have an influence on $\langle \tau \rangle$. However, the mean dwell times of the vertical rectangles differ.
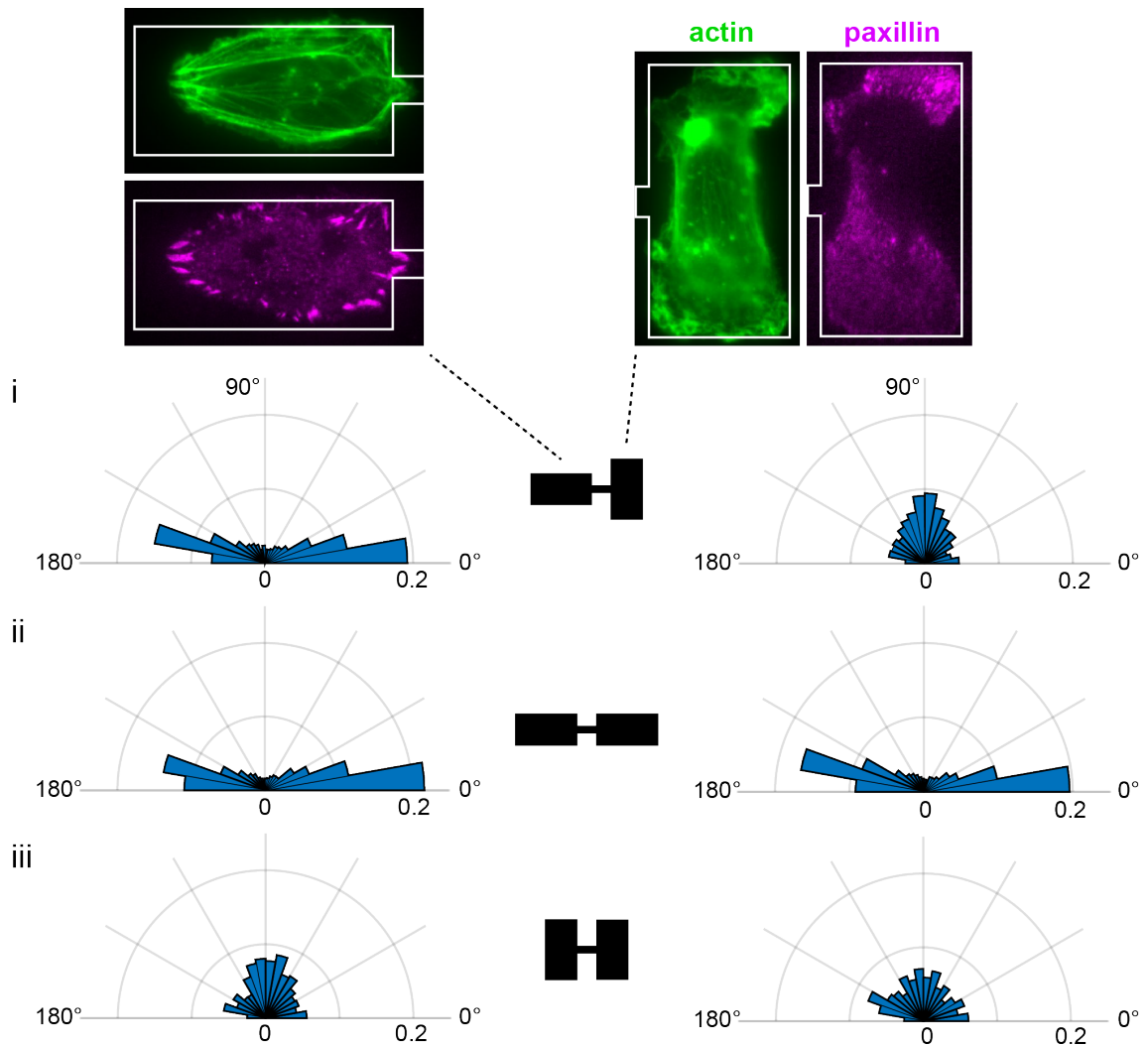
Figure 4.8.: The angular distributions of cell motion on rectangular adhesion sites for different combinations of adhesion site orientations. Fluorescence images of cells fixed on rectangular adhesion sites and stained for their actin and paxillin are shown for the mixed setup only. The internal cell organisation does not seem to vary between the different setups, it only depends on the orientation of the adhesion site. Figure reprinted from Fink et al. [2] with author's rights.
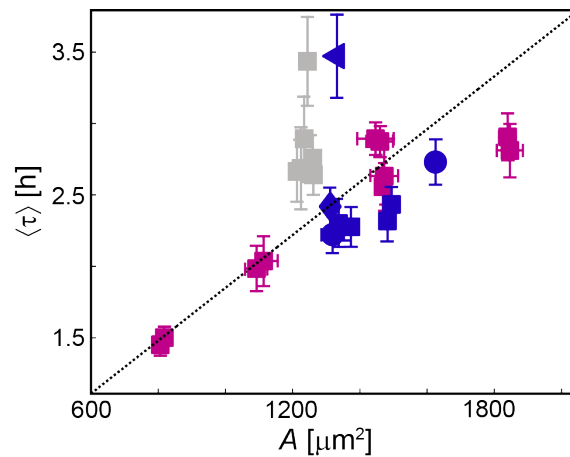
Figure 4.9.: Mean dwell times $\langle\tau\rangle$ plotted against adhesion site area for all adhesion site shapes and orientations in two-state micropatterns with a bridge length of $L \approx 16\,\mu\text{m}$. The pink data points correspond to square adhesion sites from square-square-micropatterns, for the blue data points the marker shape corresponds to adhesion site shape and the grey data points correspond to the rectangular adhesion sites. The grey outlier is $\langle\tau\rangle$ on the upright rectangle in the mixed setup. The dashed line is a guide to the eye. x-errors are weighted standard deviations and y-errors are bootstrapping errors. Figure reprinted from SI of Fink et al.[2].

4.3. Discussion

In this chapter it was shown that the previously described repeated transitions of cells on two-state micropatterns (Chapter 3) also occur when the adhesion site shape and orientation is varied. Furthermore, associated readouts like dwell times τ or velocities v can be used to quantify and characterise the cellular response to cues in the adhesive environment. The observation that cells preferentially localise on larger adhesion sites, and consequently exhibit larger dwell times there, is in line with reported *dimension sensing* on thin lines (termed 1D) interspersed with 2D rectangles. In that case it was found that cells preferentially localised on the rectangles[145]. Also, cells released from larger adhesive micropatterns tend to show reduced or no motility in comparison to those released from smaller micropatterns[45]. Endothelial cells stiffen with increasing spreading area[146]. In contrast, single MDCK II cells do not linearly increase their stiffness in response to different adhesion site areas but follow a bimodal trend. However, when they are part of a confluent cell layer, these cells also increase their stiffness with increasing cell area[147]. Although there is no equi-

valent to dwell times in cell migration on unpatterned 2D substrates, it is possible that similar mechanisms influence cell behaviour. Thus, freely migrating cells show reduced migration rates with increasing spreading area[131]. Larger adhesive areas provide more adhesive ligands, and high levels of substrate adhesiveness reduce cell migration velocities[148], providing a potential explanation for the increase of dwell times with adhesion site areas. In line with studies on micropatterns, it was found that spread out mesenchymal cells reduce their volume by water efflux, which in turn results in cell stiffening[149]. A stiffer cell cortex has been linked to slower migration and lower invasion[150]. Thus, another likely explanation for the observed increase of dwell times with adhesion site areas (Fig. 4.1 B, C) is a transient cell stiffening due to increasing cell size on larger adhesion sites. As mentioned previously in Chapter 4.1, cell area does not increase as much as adhesion site areas (Fig. 4.1 D). Therefore, other mechanisms are likely to contribute to the linear increase in mean dwell times $\langle \tau \rangle$ as well. For example, cells which do not fully fill the adhesion sites are free to migrate within. The angular distributions of cell velocities (Fig. 4.6) support this assumption, as for medium-sized squares the extent of motion perpendicular to the axis of transitions is higher than for cells on small squares.

For adhesion sites symmetric under rotations of 90° we found only a weak dependence of occupation probabilities on shape (see Fig. 4.3 B). In particular, no bias in the square-circle system was observed. Previous studies report differently localised cellular protrusions on square and circular micropatterns[41,151]. Interestingly, this does not seem to influence escape rates measured here, although it has been suggested by Caballero et al. that hopping rates between adhesion sites depend on protrusion localisation and dynamics[49,152]. The observations reported in this thesis are in line with other reports showing that cells lack polarity on square and circular micropatterns[41] and that mechanical properties such as stiffness and contractility do not change for endothelial cells patterned on squares and circles[146]. While lacking a net polarity, it is possible that cells polarise transiently on squares and circles during the dynamic exploration of adhesion sites[153] or as a pre-requisite for transitions along the bridge. Such transient polarisation is evident in the images of the actin cytoskeleton of cells on squares and circles (Fig. 4.6). Confirming the lack of net polarisation are experiments where cells released from micropatterned squares and circles did not have a preferred direction of motion[44]. The weak influence of adhesion site shape is further remarkable as the circular adhesion sites have the

same area but a different perimeter from the opposite square adhesion sites and cell spreading is frequently modelled as being dependent on both, area and perimeter (compare Eq. 2.2)[35,36,154].

Previous studies of cell migration on triangle- or teardrop-shaped micropatterns have contradictory results and different approaches to explain their findings. While in all cases, it has been shown that teardrops and triangles can bias the direction of cell motion, the direction seems to vary depending on the cell type and on the exact design of the micropatterned surface. Thus, cells released from teardrops, or migrating on a circular arrangement of many teardrops, move in the direction of the broad, convex end[44,48]. In contrast, in a row of (unconnected) triangles (*ratchet*), cells move in the direction of the sharp triangle end[14,49]. While in the former case, it was proposed that cells migrate in response to their internal polarisation (which was also observed by Caballero et al.[49,152]), in the latter cases different mechanisms based on cellular protrusions were proposed: Thus, the direction of motion is either determined by the frequency of protrusions and the available adhesive area in that direction[49] or it is a consequence of actin stress fibres not connecting and the possibility for the resulting lamellipodium to anchor against the flat side of the neighbouring triangle[14]. Therefore, *a priori*, it was not clear what would happen for the triangular adhesion site tested here. The results obtained for the rhombus indicate that a corner pointed towards the bridge is, in the presence of other geometric cues, not sufficient to bias occupation probabilities (Fig. 4.3 B). In the case of the triangular site, the specific geometric cues also present are acute corners pointed perpendicularly to the axis of transitions. It has previously been shown that acute angles can stretch and orient cells in their direction and thereby increase friction during migration[152]. Also, cells preferentially extend lamellipodia from acute angles[155]. Therefore, our findings are in line with other studies.

Mean dwell times $\langle \tau \rangle$ on triangular and upright rectangular adhesion sites deviate most from the observed linear relationship between mean dwell times and adhesion site area (Fig. 4.9). While the triangle has acute angles located on a line perpendicular to the axis of transitions (which can act as guidance cues to the migrating cell), in terms of angles, the rectangles are similar to the square adhesion sites. However, the rectangles are not isotropic under 90° rotations, have an aspect ratio of ≈ 0.5 and consequently, an orientation. Protrusion formation along the long axis of the triangle could be observed (Fig. 4.3 A) but it is even more prominent in

the rectangular adhesion sites, as can be seen in Fig. 4.4 A. Thus, cell polarisation induced by the orientation of adhesion sites biases the occupancies on rectangular adhesion sites. This polarisation is evidenced by the mean orientation of long stress fibres[156] observed in fixed cells (Fig. 4.8). Also, cell elongation is considered an indicator of polarisation[157]. Furthermore, cell polarisation in response to rectangles of lower aspect ratios[41] and lamellipodia extension from the short edges, as well as migration in the direction of the long rectangle axis[44,45,158] has been reported before. Also stripe patterns, which are similar to the rectangular adhesion sites, establish cell polarity[142,157]. In general, the effect of anisotropic adhesion sites is in agreement with conclusions made by Jiang et al. that "*asymmetry in the pattern alone is sufficient to bias the direction of cell motility*"[44] and that the overall aspect ratio of an adhesion site has a strong effect on cell polarisation[41].

The findings reported for fixed cells stained for actin and for paxillin (i.e. focal adhesions), are in agreement with observations by other authors. The dark membrane ruffles and actin hotspots visible mainly in cell corners in Figures 3.2, 3.4 and 4.3 A, are in accordance with preferential extension of lamellipodia from corners[41,44,45,151,155]. Furthermore, it was documented that focal adhesions are preferentially assembled in corners[38,151]. The observation that focal adhesions are not localised directly at the foremost actin structures (Fig. 4.7) are in line with findings for migrating endothelial cells[159] and could correspond to the difference between the functional entities of lamella and lamellipodium[63]. It is known that stress fibres orient along the direction of cell motion[160]. Therefore, the organisation of stress fibres as presented in fixed cells captured in mid-motion is not surprising (Fig. 4.6, Fig. 4.8). Looking at the angular distributions of cell velocities (Fig. 4.6, Fig. 4.8), it is possible to infer cell polarisation, as polarisation is essential for directed motion. However, it has to be noted that cell polarisation has been observed on micropatterns fully confining cells resulting in no net cell displacement[37,41]. Therefore, the angular distribution maps may not be able to completely capture cell polarisation on the presented micropatterns.

It was found that cell migration in two-state micropatterns with unequally sized adhesive islands can be captured with the same framework, Eq. 3.3, as used for equally sized squares[1]. However, intriguingly, the theoretical description does not capture the occupation probabilities on rhombi, triangles and upright rectangles, indicating that a new quantity has to enter the model to fully capture the dynamics

on anisotropic adhesion sites. This is not altogether surprising, as the mean dwell times on triangles and upright rectangles deviate from the linear area-dependence of dwell times (Fig. 4.9), and the motion within the adhesion sites has a non-negligible extent in y-direction (Fig. 4.6, Fig. 4.8). Moreover, on rectangular adhesion sites, memory effects seem to be relevant. On no other tested adhesion site geometry, the dwell times depend on the neighbouring adhesion site (Fig. 4.1 B, Fig. 4.9 and Tab. 4.1). Neither actin nor paxillin organisation is different for the different rectangle two-state-system setups[2]. Memory effects have been observed before for cells migrating on topological ratchet patterns[135], for cells spreading on fibronectin micropatterns[35] and for cell migration in the presence of chemoattractants[161]. Interestingly, a memory for the orientation of stress fibres was reported with a memory time of ≈ 50 minutes[35]. While this is shorter than typical dwell times on the rectangles (compare Table 4.1), it is of the same order of magnitude, and could certainly contribute to the difference in dwell times. However, why the effect seemingly only occurs for the vertical rectangle is unclear, especially in light of the dwell times $\tau_\parallel$ for all setups being equal within errors.

5. Conclusion and Outlook

In this thesis, I introduced an artificial two-state system, consisting of two cell-sized adhesion sites which are connected by a thin bridge. MDA-MB-231 cells repeatedly transition over the bridge and adapt their shape and migratory behaviour in response to the adhesion site geometry. We have developed a theoretical model based on the short-timescale dynamics of transitioning cells that accurately captures time- and ensemble-averaged quantities of the system. The resulting phase-space maps can be used to compare cellular dynamics with respect to a "ground state". Here, a ground state could be given by the migration of wild-type cell lines in the symmetric two-state system, and the change in dynamics in response to the addition of drugs or to a change in gene expression could be systematically analysed. So far, an analytical expression for both, $F(x, v)$ and $\sigma(x, v)$ could not be found. However, it might be possible in future work to derive analytical expressions, making it easier to extract actual parameters and to link them to "state variables" of the cell. Related to that, the Cellular Potts Model could help gain insights into the "laws" of cell migration in confining two-state micropatterns. If its parameters are set in a way that the main quantities of migrating cells on dumbbell-like micropatterns are captured, they could be linked to experimental quantities.

In the two-state micropatterns, cell lines derived from different tissue types transition between the two adhesion sites, indicating that this is a common behaviour in motile cells. So far, the migration of MDA-MB-231 and MCF10A cells within the two-state setup has been extensively analysed. For quantification of the cellular dynamics, it is essential to be able to generate large statistics, which is also a pre-requisite for the data-driven modelling approach. To quantify the migration of a wider range of cell lines, it is necessary to find the right parameters for micropatterning. Both, the size of the adhesion sites and channels, and the biochemistry involved contribute to efficient confinement and cell guidance. Perhaps not surprising, but intriguing, is the fact that some cells can be confined on micropatterns created by μCP but disregard the patterned structures if placed on microstructures created by μPIPP. This phenomenon could be related to the different mechanisms of protein adsorption to the surface, namely by hydrophobic effect (μPIPP) or via electrostatic interac-

tions (μCP), or to some residual topography. Also, the surface exposed to oxygen plasma or subjected to UV light/ozone treatment is altered; thus, hydrophobic surfaces become hydrophilic and the surface roughness was found to increase[162,163]. This should theoretically not affect cells during the experiments, as they supposedly are not in direct contact with the plastic substrate. However, the relative height of polyethylene glycol (PEG) brushes and protein might be different for the two patterning techniques. Also, the surfaces to which fibronectin adsorbs are different: For μCP the whole surface is subjected to UV/ozone treatment, and therefore fibronectin binds to a hydrophilic surface, while the surface remains hydrophobic for μPIPP. That fibronectin orientation on hydrophobic and hydrophilic surfaces is different, has been established[164]. Moreover, fibronectin orientation is also related to fibronectin concentration - an effect less pronounced for high fibronectin concentrations[165]. Potentially, the difference in migration behaviour is related to the ability of cells to rearrange adsorbed fibronectin[166]. While there are many approaches to explain the differences in cell response to differently patterned surfaces, further study is required to elucidate the actual mechanisms. Resolving the height and nanostructure of the micropatterned surfaces using atomic force microscopy (AFM) could provide valuable insights.

The theoretical model gives detailed insights into the dynamics of cell migration. Specifically, on two-state patterns with a bridge width of 7.2 µm, the deterministic dynamics of MDA-MB-231 cells follows a limit cycle, while MCF10A cells show bistable behaviour. As a next step, it is crucial to gain a more thorough understanding of the fundamental cellular processes underlying migration in two-state micropatterns. To this end, modified versions of the previously used cell lines could be used. A genetic knockout or overexpression, possibly combined with a fluorescence tag for quantification purposes, would allow to study the individual contribution of target proteins to cellular dynamics. Proteins of particular interest are E-Cadherins: MDA-MB-231 and MCF10A cells express different levels of E-Cadherins[167]. While MDA-MB-231 cells have undergone the epithelial-mesenchymal transition (EMT), MCF10A cells have an epithelial phenotype[167,168]. Also, E-Cadherins are key mediators of cell-cell contacts and seem to regulate invasiveness. Specifically, it has previously been established that increased E-Cadherin expression reduces invasiveness *in vitro*[169,170] and the loss of E-Cadherin promotes invasion and motility. However, for invasion it is not sufficient that cells lose their cell-cell adhesions, as in the pres-

ence of the intra-cellular domain of E-Cadherin invasiveness was not increased[171]. Thus, it remains to be seen how much of the difference in cell dynamics established for both cell types relates to their E-Cadherin levels. Another approach to pinpoint molecular key players would be to apply drugs to inhibit functions in wild-type cells. This method in particular would also help with the parametrisation of the theoretical model. Also, the effect of polarisation-disrupting drugs could be studied to further test the conclusions drawn in Chapter 4.

Interestingly, phenomenologically non-cancerous MCF10A and highly metastatic MDA-MB-231 cells show a very similar migration behaviour in the dumbbell-setup. In contrast, we identified qualitative differences in the deterministic dynamics. What is more, even for a single cell line, MDA-MB-231, we found three different dynamic behaviours, namely limit-cycle oscillations, bistable behaviour and the relaxation onto a line of fixed points at $v = 0$. In particular, the dynamic response depends on the bridge width in the two-state micropattern. As the cells have to deform during lamellipodia formation that precedes transitions, and also during the transition over the bridge, the readouts obtained in experiments on dumbbell micropatterns may be related to cellular and nuclear mechanics, and ultimately to invasive potential[172,173]. This is all the more important, as invasiveness is a clinically relevant parameter. The standard method to measure invasiveness is a Boyden chamber migration assay, where the fraction of cells that migrate through ECM and a porous membrane within a certain time is determined[174,175]. Thus, the Boyden chamber assay yields a meaningful endpoint readout that, however, does not reveal the dynamics of invasion. In many cases, invasiveness was only determined for similar cell types. Therefore, it was not possible to directly compare invasiveness ratings for all cell lines probed in our setup (as illustrated in Table 3.1 where no unifying invasiveness scale could be used). However, a simple Boyden chamber invasion experiment could provide this information. It is yet unclear which quantities characterising cell migration in two-state micropatterns are particularly suited to characterise invasiveness. Specifically, in recent work, based on classification by machine learning, no correlation between 2D migration speed or persistence and 3D invasion was found[176]. Once suitable parameters are determined, in analogy to the first World Cell Race[46] ranking cell speed, a ranking of invasive potential based on these quantities could be developed for a wide range of cell types.

In the experiments presented in this thesis, which were performed for up to 50 h,

a large amount of data is recorded. As cells divide after a certain time, naturally, a large dataset of two-cell systems migrating in the two-state patterns is generated. What is more, these two-cell systems should be genetically identical and cell-cycle synchronised as they are daughter cells. Apart from being influenced by the respective single-cell dynamics, the interactions between MDA-MB-231 and MCF10A daughters should also be sensitive to the E-Cadherin levels of the respective cell lines. Thus, one would expect that MCF10A cells are more sticky, i.e. more adhesive to each other. In addition, it would be interesting to see whether two interacting daughter cells are more similar in their interactions and dynamics than the dynamics of two cells which do not have the same mother cell. To answer this question robustly, measurements would have to be started directly after cell seeding to track the history of all cell pairs. In a similar spirit, Milano et al. investigated homotypic collisions of MDA-MB-231 and MCF10A on micropatterned lines of variable widths. Intriguingly, they found that on all line widths MDA-MB-231 cells are more likely to slide past each other, while pairs of MCF10A cells predominantly reverse their migration direction upon contact. The knockdown of E-Cadherin, as well as activating ErbB2 while downregulating PARD3, increased the number of sliding interactions in MCF10A cells significantly. Moreover, MDA-MB-231 cells with induced E-Cadherin expression were less likely to perform sliding interactions than their wild-type counterparts[177].

The two-state micropatterns yield insight into single-cell and cell-to-cell variability. Cell-cycle synchronised cells might be used for the experiments, as a means to reduce variations in ensemble-averaged quantities at any point in time. This would be of particular interest for the study of area-dependence of dwell times, as cells grow over time and the cell-cycle synchronisation could lead to a more homogeneous distribution of cell sizes. The usefulness of drugs notwithstanding, especially in view of potential clinical applications, it would be preferable to eliminate the need for any cell labels for tracking. At the moment, all migration data is extracted from nuclear trajectories and in order to visualise the nuclear fluorescence, cells are stained with Hoechst 33342 and irradiated with UV light. A recent advance in nuclear staining was the development of sir-DNA[178], which is a nuclear label in the far-red region of light. A different approach to cell tracking would be to rely on machine learning, enabling the tracking of cells solely based on their outlines in brightfield movies. However, often measurement noise, such as floating (cell) debris, background fluor-

escence or limited image resolution complicates data analysis. Also, it remains to be seen how centre-of-mass cell coordinates are related to nuclear centre-of-mass coordinates.

It is not yet clear how the dynamics observed in 2D two-state micropatterns compares to that in 3D micropatterns. Three-dimensional dumbbell-shaped wells are already available, fabricated by hot embossing of a plastic slip[179]. Surface functionalisation is achieved by fibronectin incubation. To prevent cell adhesion to the outside of wells, and to enhance confinement, the fibronectin on the outside of the wells can be removed in a lift off step[180]. Potentially, in the 3D system nuclear deformation will become of importance, as the cell will have to squeeze through channels rather than pull itself along stripes. Nuclear staining, which is already performed for tracking purposes, may help to gain more insights into the reorientation and potential deformation of the nucleus during 2D and 3D migration. By nuclear deformation, gene expression levels may be altered[181]. The 3D setup may also be more biologically relevant[182] in the sense that cancer cell invasion typically involves physically squeezing through thin pores or the ECM. It is of special interest whether and how transition rates are linked to cancer cell invasiveness.

I could show in this thesis that the dwell times of cells scale linearly with adhesion site area, and that for the tested geometries perimeter does not seem to determine the dwell times. This finding is surprising in light of several theoretical models comprising perimeter-dependent terms which successfully predict cell shape in jammed epithelial sheets[154,183] or during spreading on micropatterns[36]. Could it be that *within the two-state setup*, where cells are constantly contracting for the bridge passage, line tension does not contribute significantly to the occupation probabilities of cells on differently sized adhesion sites? To answer this question robustly, the response to a variety of square-circle systems with equal areas but different perimeters could be probed. Also, neither cell area nor cell perimeter correspond to adhesive area and perimeter at all times. It would therefore be necessary to carefully analyse cell area and perimeter to conclude on the applicability of those models on cell migration in two-state patterns. Blebbistatin was found to selectively alter line tension[35]. Therefore, effective Blebbistatin treatment of cells could help gain insight into the relevance of line tension for migration in confinement.

On most adhesion sites with different sizes and shapes, the escape rates are inde-

pendent of the neighbouring adhesion site. Memory effects seem to be detectable only in the mean dwell times in micropatterns with orthogonally oriented rectangular adhesion sites. It remains an open question why cells leave the upright rectangle at a lower rate than in the comparable system consisting of two upright rectangles. It might be necessary to image stress fibre (SF) dynamics and quantify SF orientation as it has been previously shown that SFs can act as a memory of cell spreading[35]. Also, a careful analysis of protrusion dynamics and protrusion geometry could give insights into the transition mechanisms. Caballero et al. have shown how a transition bias can be explained by geometric considerations alone[49].

While the influence of adhesion site geometry on escape rates has been probed extensively, it is not yet known how cells would respond to adhesion sites of different chemical composition. Is it possible to measure relative affinities towards surface coatings? Such an outcome would be applicable in tissue engineering. Two-protein patterning has the potential to be employed in such experiments. However, first of all, the second protein needs to be incubated in the presence of the first protein that is already adsorbed onto the surface. For that reason, protein-protein binding presents a challenge. Second, the technique introduced by Segerer et al.[93] makes use of framed patterns, where the frame is coated in a protein different from that within the framed area. Therefore, the response to both proteins would not be probed separately. Photopatterning is an emerging technique for surface modification[184–186]. For example, using UV light, it is possible to project a pattern onto a PEG-coated surface, which leads to localised PEG cleavage due to the presence of a photo initiator, leaving blank spaces for protein adsorption. This can be repeated, and various proteins can be subsequently incubated[187]. Once more, protein-protein binding might be an issue as the second protein is incubated on top of the first one. Also, the speed of the patterning process is often a limitation[185]. However, in theory, optical methods allow for the parallel patterning of several geometries, and for wavelength-dependent selection mechanisms. In addition, the patterning is less sensitive to manual handling variations than stamp-based techniques. Thus, photopatterning techniques have the potential to replace μCP and μPIPP.

In summary, I have developed an artificial two-state system which is a versatile tool to study cell migration as a function of the confining microenvironment. Specifically, we find that the cellular dynamics of MDA-MB-231 and MCF10A cells within the two-state system is well captured by a nonlinear stochastic equation of motion. This

holds for micropatterns with varying bridge lengths and widths and with differently sized and shaped adhesion sites. The escape probabilities of cells from adhesion sites depend on adhesion site area, shape and orientation. In combination with fluorescent tags, and mutants of the cell lines studied so far, the molecular mechanisms governing cell migration in confinement can potentially be unravelled.

A. Appendix: Methods

A.1. Experimental Methods

A.1.1. Microscale Plasma-Initiated Protein-Patterning

Silicone wafer moulds are prepared in the clean room using photolithography (see SI to Brückner et al.[1], Segerer et al.[93]). To create stamps, polydimethylsiloxane (PDMS) monomer and crosslinker (DC 184 elastomer kit, Dow Corning) are mixed in a 10:1 (w/w) ratio and then degassed for about 1 h in an exsiccator. Afterwards, the mix is poured onto the silicone wafer, degassed for about 2 h and cured overnight in an oven at 50°C. Stamps are prepared by peeling the PDMS off the wafer, and cutting the structured areas of the PDMS into small pieces of a maximum approximate size of $0.4\,cm \times 0.4\,cm$. These stamps, with the features facing down, are then placed into a μ-dish (ibidi GmbH). In the next step, the dish, with the lid taken off, is put into the plasma cleaner (Pico, electronic diener). To achieve a clean plasma, the chamber is evacuated for 10 minutes before it is flooded with oxygen for 3 minutes. Subsequently, at a constant gas pressure of 0.48 mbar, the plasma process is started and the sample is subjected to oxygen plasma for 3 minutes. Quickly after the plasma process has finished, a drop of $2\,mg\,ml^{-1}$ PLL(20)-g[3.5]-PEG(2) solution (pll-PEG, from SuSoS AG, resuspended in 10 mM HEPES (Gibco) and 150 mM NaCl (Roth)) is added to each stamp, where it creeps under the stamp into the uncovered spaces by capillary action. It is of utmost importance that during the addition of the pll-PEG the stamps are not touched. The pll-PEG is left to incubate for 25 minutes to achieve a good background passivation. Prior to the removal of stamps, 1 ml of phosphate-buffered saline (PBS) is added to the dish. Using tweezers, each stamp is quickly pulled up and thereby removed from the substrate. Upon removal of $500\,\mu l$ PBS, $150\,\mu l$ of $216.67\,\mu g\,ml^{-1}$ fibronectin solution are added (YO Proteins), so that a final fibronectin concentration of $50\,\mu g\,ml^{-1}$ is left to incubate for 50 minutes. The last step is to wash the sample with PBS nine times. After preparation, samples should be stored at 4°C in PBS.

A.1.2. Cell Culture

MDA-MB-231 human breast carcinoma cells (DSMZ) are cultured in minimal essential medium (MEM) (initially obtained from c.c. pro and supplemented with 2 mM L-Glutamine (c.c. pro), later replaced with MEM from Gibco) with 10% fetal calf serum (FCS) (Gibco). Cells are cultured at 37°C in a 5% CO_2 atmosphere. At about 70-90% confluence, cells are passaged: First, cells are rinsed once with PBS. Second, Trypsin-EDTA (0.05%, Gibco) is added and incubated for 3 minutes at 37°C. During splitting, medium is added to the cell suspension, the required fraction of cells is seeded in a new culture flask and covered in fresh medium. For experiments, the trypsinised cell solution is centrifuged at 1000 rcf for 3 minutes, the cell pellet is resuspended in MEM and cells are counted in a Neubauer cytometer. One fraction of cells is used for further culturing and approximately 10000 cells are subsequently seeded per patterned μ-dish. Prior to that, the patterned dish is taken out of the fridge, and the PBS is gradually exchanged for cell culture medium. Cells are left to adhere for approximately 4 h in the incubator, before the medium is exchanged to CO_2-independent L-15 medium (without phenol red; containing L-Glutamine (Gibco), additionally supplemented with 10% FCS) with 25 nM Hoechst 33342 (Invitrogen) to stain the cell nuclei. Afterwards, the dish is placed under the microscope and left to thermally equilibrate for 30 minutes before time-lapse positions are set. Experiments are typically started within 2 hours after the last medium exchange.

MCF10A cells (ATCC) are cultured in DMEM:F-12 medium including Glutamax (Gibco), supplemented with 5% Horse Serum (Thermo Fisher), $20\,\text{ng}\,\text{ml}^{-1}$ human Epidermal Growth Factor (hEGF) (Sigma), $500\,\text{ng}\,\text{ml}^{-1}$ Hydrocortisone (Sigma), $100\,\text{ng}\,\text{ml}^{-1}$ Cholera Toxin (Sigma) and $10\,\mu\text{g}\,\text{ml}^{-1}$ Insulin (Sigma) at 37°C in an atmosphere containing 5% CO_2. For passaging, the supernatant is aspirated and subsequently centrifuged at 300 rcf for 8 minutes. In the meantime, cells are rinsed with PBS and detached using Accutase, which needs to be incubated for 12 minutes at 37°C. Upon addition of medium, the cell solution is centrifuged at 500 rcf for 6 minutes. The cell pellets resulting from both centrifugation steps are resuspended in medium. For further culturing, a fraction of the cells detached with Accutase, and all cells from the supernatant are used. For experiments, 10000 cells are seeded per micropatterned μ-dish. Samples are then put into the incubator and left to adhere

to the patterns for at least 4 h. Afterwards, the medium is exchanged to DMEM:F-12 containing all supplements but lacking phenolred. Also, 15 nM Hoechst 33342 is added. During experiments, the samples are kept in an atmosphere with 5% CO_2 and at 37°C.

A.1.3. Cell Fixation and Immunostaining

For actin and paxillin localisation experiments, cells are cultured and seeded as previously described. However, the medium is not changed to L-15 and cells are left for a total of 16-24 h in the incubator after seeding. Then cells are rinsed once with (37°C) warm PBS, and afterwards warm (37°C) 3.8% formaldehyde in PBS (Sigma) is added for fixation and incubated for 15 minutes at room temperature. The cells are rinsed twice with PBS, before a 0.5% Triton X-100 (Roth) in PBS solution is added for 5 minutes. After washing the sample twice, a blocking solution consisting of 10% normal goat serum (Abcam), 0.2% Triton X-100 and PBS is applied for 30 minutes at room temperature. This is replaced by the same blocking solution containing the primary antibody, mouse anti-paxillin (Invitrogen), at a concentration of $5\,\mu g\,ml^{-1}$. After incubation for 1 h at room temperature, the sample is washed three times for 5 minutes with PBS containing 1% (w/v) bovine serum albumin (BSA)(Roth). Subsequently, $5\,\mu g\,ml^{-1}$ of the secondary antibody (goat anti-mouse conjugated with Alexa Fluor 488; Abcam) and 100 nM rhodamine phalloidin (Molecular Probes) are added in a blocking solution made of 10% normal goat serum in PBS. This is incubated for 30 minutes at room temperature. Care has to be taken to protect the sample from light to avoid photobleaching. The sample is washed three times for 5 minutes in PBS-BSA. In the next step, $0.5\,\mu g\,ml^{-1}$ DAPI (Sigma) is added for 5 minutes at room temperature. Lastly, the sample is washed three times with pure PBS for 5 minutes, and can be stored in the fridge afterwards.

Note that it is important that the solutions are prepared freshly on the day of experiments. It is also recommended to image the sample on the day of preparation as the fluorescence deteriorates after prolonged storage. Furthermore, I found that it is preferable to image a maximum three stamps per dish as the fluorescence intensity and staining quality deteriorates throughout the sample during imaging. For greater statistics, it is advisable to prepare several dishes in parallel.

A.1.4. LifeAct-GFP Transfection

For live cell experiments with stained actin, approximately 12500 MDA-MB-231 cells, cultured and resuspended as described above, are seeded in patterned μ-dishes and left to adhere overnight. Two vials need to be prepared: **Vial I** contains 500 ng LifeAct-GFP messenger ribonucleic acid (mRNA) (in-house prepared) resuspended in OptiMEM (Gibco) to a final volume of 150 µl. **Vial II** contains a mix of 1.25 µl Lipofectamine 2000 (Invitrogen) and 123.75 µl OptiMEM, which needs to stand for 5 minutes after mixing. Then, the contents of **vial I** are added to the contents of **vial II** and mixed carefully by pipetting up and down several times. The mix is left for 20 minutes at room temperature. Before the transfection mix is added to the sample, cells are rinsed once with PBS. Cells are incubated with the transfection mix for at least 3 h in the incubator. Afterwards, the transfection mix is replaced by L-15 medium supplemented with L-Glutamine and FCS.

As cells are washed more often than for experiments without actin staining, it is advisable to seed more cells. Also, I have tried to change the order of the transfection protocol, first transfecting cells grown in the culture flask up to approximately 70% confluence and only subsequently seeding the transfected cells onto the micropatterns. However, this resulted in a low number of transfected cells on the patterns. It seems as though transfected cells do not adhere as well to the fibronectin-coated micropatterns as untransfected cells.

A.1.5. Microscopy

Time-lapse measurements of up to 50 h duration are performed either on an IMIC digital microscope (TILL Photonics) or on a Nikon Eclipse Ti microscope using a 10x or a 60x oil-immersion objective. To keep samples at 37°C throughout the measurement, the microscopes are fitted with heated chambers (ibidi GmbH or Okolab) into which the samples are placed. In Table A.1, illumination settings are detailed for the different types of experiments.

Note that while the temperature of the heated chamber is set to a fixed value, temperature variations are likely to occur. The temperature of the chamber is calibrated for a certain room temperature, and unless used in sample-feedback loop, only the chamber cage temperature is used for feedback. In particular, the chamber is placed

Experiment	Micro-scope	Ob-jective	Chan-nels	Illumination	Inter-val
Standard Protocol	Nikon TIRF	10x	BF DAPI	40 ms, 30% 250 ms, 50%	10 min
Standard Protocol	Imic	10x	BF DAPI	100 ms, 60% 100 ms, 25%	10 min
Standard Protocol MCF10A	Nikon TIRF	10x	BF DAPI	40 ms, 30% 100 ms, 50%	10 min
Actin-LifeAct	Nikon TIRF	60x	BF GFP	40 ms, 30% 150 ms, 50%	10 min

Table A.1.: Microscope and illumination settings for the different experimental setups. Unless further specified, these are the settings used for imaging MDA-MB-231 cells.

inside a room that until recently was not air conditioned, and was therefore subject to temperature variations. Also, the temperature within the sample is likely to rise through continued illumination as well.

For MCF10A cells stained with 15 nM Hoechst 33342 these illumination settings are the minimum required exposure time and illumination intensity. It is recommended to check whether these settings are sufficient because for some of the cells I tracked, the nuclear fluorescence was of the order of the background fluorescence.

It is interesting to note that under these experimental conditions we observe that the doubling time of cells is slightly larger than in cell culture. The influence of micropattern size and geometry on cell proliferation has been reported before[32,146,188].

A.1.6. Cell Area Determination

Cell areas are manually traced with the help of ImageJ's Ivussnakes Plugin[189]. Cell areas are determined only at times of full confinement within an adhesion site (i.e. there are no protrusions inside the channel). It is likely that this approach overestimates the influence of smaller cells, which are more likely to fully fit into adhesion sites of all tested sizes. Thus, to mitigate that effect, the mean cell area is calculated for each stay rather than being calculated as an average over all video frames used. The average of these areas per stay is taken as final cell area.

A.1.7. Micropattern Design

The exact dimensions of two-state micropatterns are detailed in Tables A.2, A.3, A.4 and A.5. Adhesive area dimensions were adapted to cell area to provide enough adhesive area for cells so that cells would fully fit into the sites. Thus, it was found that for square adhesion sites with edge lengths smaller than approximately 25 µm cells would still transition between adhesion sites but could partially remain on the bridge and the larger adhesion site. Therefore, no adhesion sites with edge lengths smaller than 25 µm were used. To prevent extensive cell motion within the adhesion sites, no squares with edges longer than 42.2 µm were used.

The reference area used is that of unconfined cells plated on a fibronectin-coated substrate. Thus, about 4 h after cell seeding, the mean cell area is 939 ± 37 µm^2, and within the next 20.5 h it increases to 1395 ± 122 µm^2. This is all the more important as some adhesion sites may be too large initially but may be filled completely by cells at a later point in time.

The aim of using square-circle micropatterns is to present adhesion sites of either the same area or the same perimeter to cells. Micropatterns with rhombi and triangles were designed to have adhesion sites of equal areas and to have a right angle pointed at the bridge. This is to test the influence of shape while keeping the funnelling angle constant. Rectangular adhesion sites have equal areas. Their area was chosen to be similar to that of the squares in symmetric square-square patterns. The rectangles have an aspect ratio of 2:1. For all two-state micropatterns with unequal adhesion sites, a similar bridge length was used. The bridge length was chosen to be equal to one of the bridge lengths used in the symmetric square-square setup. Further considerations concern the generation of sufficient statistics, which means that the bridge should be as short as possible while providing sufficient spatial separation of the adhesion sites so that cells are occupying one adhesion site at most times rather than stretching onto both. To achieve the latter point, long bridges are favourable. As a compromise, a medium bridge length was chosen for asymmetric micropatterns. As the dynamics and sizes of different cell types vary, such geometric scaling considerations have to be taken into account for each cell line individually.

Errors in the pattern dimensions are weighted standard deviations, unless noted otherwise, accounting for the variable statistics in different experiments. Final protein patterns are subject to experiment-to-experiment and wafer-to-wafer variations.

X-Dimensions Left Site [µm] (a)	X-Dimensions Right Site [µm] (a)	Area Left [µm^2]	Area Right [µm^2]	Number of Analysed Cells	Bridge Length (L) x Width (w) [µm^2]
37.2 ± 0.2	37.1 ± 0.1	1380.6 ± 11.2	1377.6 ± 10.9	98	$(6.4 \pm 0.3) \times (7.8 \pm 0.6)$
36.4 ± 0.1	36.3 ± 0.2	1327.9 ± 5.4	1314.1 ± 11.1	101	$(9.2 \pm 0.3) \times (7.5 \pm 0.7)$
37.2 ± 0.8	37.4 ± 0.6	1385.1 ± 57.7	1397.0 ± 43.7	169	$(15.7 \pm 0.3) \times (7.4 \pm 0.3)$
36.1 ± 0.1	36.3 ± 0.2	1303.7 ± 10.0	1316.0 ± 13.7	216	$(23.7 \pm 0.4) \times (6.3 \pm 0.7)$
37.6 ± 0.1	37.4 ± 0.2	1411.3 ± 9.5	1395.4 ± 13.4	149	$(35.3 \pm 0.5) \times (7.2 \pm 0.5)$
36.1 ± 0.1	36.2 ± 0.1	1304.0 ± 5.2	1311.2 ± 9.5	127	$(46.2 \pm 0.4) \times (6.2 \pm 0.7)$
35.9 ± 0.0	36.1 ± 0.1	1292.2 ± 1.3	1302.6 ± 6.0	74	$(56.0 \pm 0.3) \times (5.9 \pm 0.3)$

Table A.2.: Detailed measures of the square adhesion sites of two-state patterns with varying bridge length L. The variations in bridge widths w and adhesion site edge lengths a are mainly due to wafer-to-wafer variability. Errors, apart for the bridge widths w, are weighted standard deviations. The error in w is the standard deviation.

X-Dimensions Left Site [µm] (a)	X-Dimensions Right Site [µm] (a)	Area Left [µm^2]	Area Right [µm^2]	Number of Analysed Cells	Bridge Length (L) x Width (w) [µm^2]
37.5 ± 0.3	27.5 ± 0.2	1405.0 ± 22.5	754.7 ± 11.0	47	(16.0 ± 0.3) $\times$ (7.8 ± 0.3)
37.6 ± 0.6	32.4 ± 0.7	1410.6 ± 45.1	1052.0 ± 45.4	68	
42.1 ± 0.3	27.3 ± 0.4	1776.2 ± 25.3	743.1 ± 21.8	58	
42.2 ± 0.5	32.1 ± 0.6	1782.1 ± 42.2	1028.8 ± 38.5	74	

Table A.3.: Detailed measures of the two-state patterns with differently sized square adhesion sites. Errors, apart for the bridge widths w, are weighted standard deviations. The error in w is the standard deviation.

X-Dimensions Left Site [µm]* (a)	X-Dimensions Right Site [µm]* (a)	Area Left [µm²]	Area Right [µm²]	Number of Analysed Cells	Bridge Length (L) x Width (w) [µm²]	Experiment
36.5 ± 0.4	40.3 ± 0.6	1329.7 ± 29.2	1275.0 ± 38.0	67	(14.5 ± 0.2) $\times$ (6.1 ± 0.1)	eqA
35.9 ± 0.2	44.6 ± 0.3	1291.9 ± 14.4	1580.2 ± 21.0	98		eqU
37.6 ± 0.2	46.7 ± 0.5 49.6 ± 0.6	1413.8 ± 14.3	1243.2 ± 24.7	63	(17.7 ± 0.1) $\times$ (7.7 ± 0.1)	rho
37.8 ± 0.2	33.5 ± 0.3 67.7 ± 0.7	1428.8 ± 17.3	1263.8 ± 16.5	82		tri
48.9 ± 0.7 24.9 ± 0.3	48.9 ± 0.8 24.9 ± 0.3	1217.6 ± 26.2	1217.6 ± 24.6	78	(16.2 ± 0.1) $\times$ (5.0 ± 0.2)	LR
24.9 ± 0.4 47.9 ± 0.5	24.8 ± 0.3 47.8 ± 0.4	1192.7 ± 22.1	1185.4 ± 15.3	65		SR
48.2 ± 0.7 24.3 ± 0.4	25.2 ± 0.2 47.8 ± 0.5	1171.3 ± 24.0	1204.6 ± 16.9	59		MR

Table A.4.: Detailed measures of the two-state patterns with differently shaped and oriented adhesion sites. Errors, apart for the bridge widths w, are weighted standard deviations. The error in w is the standard deviation. The abbreviations for experiments denote the following setups: *eqA, eqU* - square-circle patterns with equal area or perimeter respectively, *rho, tri* - square-rhombus, square-triangle patterns, *LR, SR, MR* - lying, standing and mixed rectangles, respectively.

*: If the adhesion site is not symmetric in x- and y-direction, the measures of the edge lengths in both directions are given, with the upper number corresponding to x-dimensions (a) and the lower number corresponding to y-measures (b) of the longest axis, respectively.

X-Dimensions Left Site [µm] (a)	X-Dimensions Right Site [µm] (a)	Bridge Length (L) [µm]	Bridge Width (w) [µm]	Number of Analysed Cells
36.2 ± 0.1	36.1 ± 0.0	36.8 ± 0.1	3.5 ± 0.2	89
35.5 ± 0.1	35.4 ± 0.2	37.6 ± 0.2	12.1 ± 0.1	97
35.7 ± 0.1	35.7 ± 0.1	37.3 ± 0.1	18.5 ± 0.3	127
-	-	103.4 ± 0.3	34.8 ± 0.2	212

Table A.5.: Detailed measures of the square adhesion sites and bridges of two-state patterns with varying bridge width w. The variations in adhesion site edge lengths a are mainly due to wafer-to-wafer variability. The last entry corresponds to a rectangular stripe of similar dimensions to the two-state micropatterns. Errors are weighted standard deviations.

The experiment-to-experiment variability is mainly caused by the manual stamping process and the associated intrinsic variance. Also, it is difficult to assess exact measures due to limited image resolution, so that measurement uncertainty is another factor contributing to the errors.

A.2. Data Analysis

A.2.1. Movie Analysis

Unless specified otherwise, all image analysis is performed using ImageJ[190]: The acquired time-lapse movies are manually screened to find cells suitable for further analysis. The criteria determining what a suitable cell is are detailed below in Section A.2.2. The micropatterns are easily visible in phase contrast images, as the plasma process modifies surface properties. If suitable cells are found, the original movies are cropped and rotated so that the micropattern's long axis is aligned horizontally. The horizontal axis is from now on defined as x. For each video, the coordinates of a manually selected point on the left side of the micropattern roughly at the height of the middle of the bridge are recorded. In the next step, a band pass filter is applied to the fluorescence images of the nucleus to de-noise them. This enables the use of a thresholding method to binarise the images. For that, the threshold is set manually by operating a slider on the user interface, and by inspecting the

nuclear images. Only if the nucleus is the only feature left in the thresholded images, ImageJ's Analyze Particles plugin is run, reading out the positions of the nucleus' brightness centre-of-mass. As the images have been binarised before, this is equal to the nucleus' centre-of-mass. The error in the localisation of nuclear centres-of-mass has been estimated to be ≈ 2 µm by repeated manual thresholding and tracking.

Absolute nuclear positions in the frame of reference of the micropattern can be determined by subtracting the nuclear coordinate from the boundary coordinate. In order to localise the cell within the micropatterned geometry, it is also necessary to know the measures of the micropattern. I have chosen between 5-10 videos from each experiment and manually marked the following features:

- left edge of the micropattern

- the point where the left adhesion site meets the bridge

- the point where the right adhesion site meets the bridge

- right edge of the micropattern

With these coordinates, micropatterns are well defined in one dimension. To centre cell trajectories, the coordinate of the middle of the micropattern has to be calculated, and this value can then be used to subtract from the nuclear coordinate. Mean micropattern dimensions are calculated per experiment. Pixel values are converted to micrometres using the following relations:

- **Nikon TIRF microscope**, 10x objective: 1px $\hat{=}$ 0.648 µm

- **Imic microscope**, 10x objective: 1px $\hat{=}$ 0.647 µm

Also note that while the nuclear x-coordinate is well defined by actual micropattern features for reference, the y-coordinate is less well defined due to the choice of the point of reference. In future work it would be useful to define a corner of the micropattern as a point of reference, or to automatically detect the pattern outlines.

A.2.2. Data Inclusion Criteria

For all micropatterns with a constriction, only cells complying with the following criteria were used for further analysis. These criteria were determined in order to achieve maximum comparability between cells and experiments by standardisation of procedures and to limit the effects of abnormal migration behaviour.

1. Only single cell trajectories are included in the analysis. No other cells are allowed in the micropattern for the duration of tracking. Also, cells are not included if other cells have previously occupied that micropattern or if other cells are close enough to the micropattern so that both, the cell within and the cell outside interact with each other. Cells are tracked between the time point they enter the micropattern and when they round up for division.

2. Only trajectories of cells which are entirely confined within the micropattern are included. This means that the cells and their protrusions have to be within the boundaries of the micropattern at all times.

3. To avoid start- and end-of-measurement artefacts, the trajectories are cropped so that they only include the motion between the first and up to the last transition between adhesion sites.

4. Only cells which do not show abnormalities such as multiple nuclei are included for further analysis. Cells undergoing cell death at any point during the measurement are excluded from further analysis.

5. Cells have to perform complete transitions in the vast majority of cases. A complete transition is a transition where all parts of the cell have left the previous adhesion site once that the cell nucleus enters a new adhesion site.

While criteria 1 and 4 are basic requirements for the study of single cells, criteria 2, 3 and 5 are a consequence of the experimental setup. Criterion 2 may need to be refined or relaxed as it is based on what is visible under a 10x objective in phase contrast microscopy. Under higher magnification, I have seen filopodia vividly exploring the passivated area and also it seems that the lamellipodia frequently extend a few micrometers into the passivated areas. Criterion 5 may be a rather strong constraint, depending on the cell type. Therefore, we previously tested whether we can relax this criterion and found that it does not affect general conclusions on cell dynamics[1]. However, considering that we intend to probe cell response to adhesion sites of different geometries *separately*, it seems sensible to apply criterion 5 nonetheless. Furthermore, incomplete transitions are only one manifestation of cells interacting with both adhesion sites at once. Sometimes, cells start spanning between the two furthest edges of the micropattern. As it has been shown that in such cases the nucleus migrates back and forth[139], such a behaviour could bias the dwell times. Also, the impact of incomplete transitions and spanning behaviour will depend on

the choice of the definition of the two states in the micropatterns; if the two states are defined as being to the left and to the right of the middle of the bridge, nuclear fluctuations will more severely affect dwell times. If the the two states are defined on the islands only, at least spanning behaviour should not bias dwell times. A strong argument for the inclusion of cells <u>not</u> complying with criterion 5 is improving the statistics, and also probing a higher proportion of the cell population with more variable behavioural phenotypes.

On rectangular stripes, all moving cells were included for further analysis. In consequence, cells which do not comply with criterion 3 were also included, as "transitions" are not well defined on a continuous stripe.

A.2.3. Dwell Times and Occupation Probabilities

According to the data inclusion criteria, trajectories are cropped so that they start after the first transition and end before the last transition. To calculate dwell times, cellular x-positions are binarised according to the definition of the two states on the micropattern. In this thesis, the middle of the connecting bridge defines the border between the two states. Specifically, the middle of the bridge is determined by adding the sum of the dimensions in x of the left adhesion site and half of the bridge length to the left border reference point for each cell. The dimensions of the adhesion site and of the bridge used in this calculation are mean values determined for each experiment. τ, the dwell time, is defined as the time between two subsequent transitions of the cell nucleus over the middle of the bridge, or, in other words, the time spent in each state. Relative occupation probabilities p_i are the sum of all dwell times τ_i on adhesion site i divided by the total observation time T_{tot}:

$$p_i = \frac{\sum_i \tau_i}{T_{tot}} = \frac{N i \langle \tau_i \rangle}{T_{tot}} \tag{A.1}$$

where N_i is the number of stays on site i.

And thus

$$\frac{p_{left}}{p_{right}} = \frac{N_{left} \langle \tau_{left} \rangle}{N_{right} \langle \tau_{right} \rangle} \overset{N_{left} \approx N_{right}}{\approx} \frac{\langle \tau_{left} \rangle}{\langle \tau_{right} \rangle} \tag{A.2}$$

To account for the unintended difference in adhesion site areas in differently shaped adhesion sites, some of the occupation probabilities are normalised by adhesion site

area A:

$$p_{1,norm} = \frac{\frac{p_1}{A_1}}{\frac{p_1}{A_1} + \frac{p_2}{A_2}} \tag{A.3}$$

This normalisation has only been used for square-circle micropatterns with roughly the same area, square-rhombus and square-triangle micropatterns.

A.2.4. Survival Probability Function

To visualise the distribution of dwell times τ, survival probability functions $S(t)$ are useful. $S(t)$ is defined as follows:

$$S(t) = 1 - \int_0^t p(\tau)\, \mathrm{d}\tau \tag{A.4}$$

where $p(\tau)$ is the probability distribution of dwell times.

Note that as the data is recorded at discrete time intervals, in this work, the cumulative sum of the dwell time probabilities is used.

A.2.5. Direction of Cell Motion

The angular direction of cell motion is analysed on the adhesion sites only. To this end, the trajectories are divided into small sequences, each corresponding to a single stay on an adhesion site. These sequences are further cropped to only include positions within the adhesion sites. For each of the stays the difference between two subsequent position vectors is calculated to give a vector pointing into the direction of motion. Using the scalar product, it is possible to calculate the angle of the velocity vector with the x-axis:

$$\theta = \cos^{-1}\left(\frac{\vec{v} \cdot \vec{x}}{\|\vec{v}\|\|\vec{x}\|}\right) = \cos^{-1}\left(\frac{v_x}{\sqrt{(v_x)^2 + (v_y)^2}}\right) \tag{A.5}$$

where $\vec{v}$ is the velocity vector between two subsequent spatial coordinates of the cell nucleus, divided by the time difference between two subsequent images ($\Delta t = 10$ min) and $\vec{x}$ is the unit vector in x-direction.

A.2.6. Theoretical Analysis

We postulate that the system's dynamics can be captured with the following stochastic differential equation:

$$\frac{dv}{dt} = F(x,v) + \sigma(x,v)\eta(t) \tag{A.6}$$

with

$$F(x,v) = \langle \dot{v}|x,v \rangle \tag{A.7}$$

and

$$\sigma^2(x,v) = \Delta t \langle [\dot{v} - F(x,v)]^2 | x,v \rangle \tag{A.8}$$

The velocity v and acceleration a are calculated as numerical derivatives from the experimental data, $\eta(t)$ is Gaussian white noise with no correlations and a mean of zero. Both terms in Eq. A.6 are inferred by conditional averaging[1,191–193]. Eq. A.6 can be integrated numerically to test the model predictions.

A.2.7. Error Analysis

As the data used here is correlated, we use bootstrapping to estimate errors[194]. To this end, we generate a large number of new realisations, typically at least 50000, of our given datasets by randomly sampling from the original datasets *with replacement.* The new dataset $D = \{X_1, X_2, ..., X_N\}$ is used to calculate its mean $\langle D_{realisation} \rangle$. The standard deviation of all $\langle D_{realisation} \rangle$ gives the estimated error in the mean. To account specifically for temporal correlations in the data, the same procedure is carried out for groups of subsequent entries in the data. The number of subsequent entries used in each draw is given by the window size. The maximum window size we use is 60. The final bootstrapping error is given by the maximum standard deviation for all window sizes.

List of Abbreviations

1D one dimension(al)

2D two dimensions/two-dimensional

3D three dimensions/three-dimensional

ADF Actin Depolymerising factor

ADP Adenosine Diphosphate

AFM Atomic Force Microscopy

ATP Adenosine Triphosphate

BSA Bovine Serum Albumin

CPM Cellular Potts Model

ECM Extracellular Matrix

EMT Epithelial-Mesenchymal Transition

FA Focal Adhesion

FCS Fetal Calf Serum

FRET Fluorescence Resonance Energy Transfer

hEGF Human Epidermal Growth Factor

MEM Minimal Essential Medium

MLC Myosin Light Chain

mRNA Messenger Ribonucleic Acid

MSD Mean Squared Displacement

μ**CP** Microcontact Printing

μ**PIP** Microscale Plasma-Initiated Patterning

μ**PIPP** Microscale Plasma-Initiated Protein Patterning

PBS Phosphate-Buffered Saline

PDMS Polydimethylsiloxane

PEG Polyethylene Glycol

PLL Poly-L-Lysine

pll-PEG Poly-L-Lysine-graft-Polyethylene Glycol

RF Retraction Fibre

SF Stress Fibre

SI Supplementary Information

UV Ultraviolet

List of Figures

List of Tables

Bibliography

[1] David B. Brückner, Alexandra Fink, Christoph Schreiber, Peter J. F. Röttgermann, Joachim O. Rädler, and Chase P. Broedersz. Stochastic nonlinear dynamics of confined cell migration in two-state systems. *Nature Physics*, page 1, March 2019. ISSN 1745-2481. doi: 10.1038/s41567-019-0445-4. URL https://www.nature.com/articles/s41567-019-0445-4.

[2] Alexandra Fink, David B. Brückner, Christoph Schreiber, Peter J. F. Röttgermann, Chase P. Broedersz, and Joachim O. Rädler. Area and Geometry Dependence of Cell Migration in Asymmetric Two-State Micropatterns. *Biophysical Journal*, November 2019. ISSN 0006-3495. doi: 10.1016/j.bpj.2019.11.3389. URL http://www.sciencedirect.com/science/article/pii/S0006349519343474.

[3] David B. Brückner, Alexandra Fink, Joachim O. Rädler, and Chase P. Broedersz. Disentangling the Behavioural Variability of Confined Cell Migration. *bioRxiv*, page 797555, October 2019. doi: 10.1101/797555. URL https://www.biorxiv.org/content/10.1101/797555v1.

[4] P. Rakic. Principles of neural cell migration. *Experientia*, 46(9):882–891, September 1990. ISSN 1420-9071. doi: 10.1007/BF01939380. URL https://doi.org/10.1007/BF01939380.

[5] David M. Rose, Ronen Alon, and Mark H. Ginsberg. Integrin modulation and signaling in leukocyte adhesion and migration. *Immunological Reviews*, 218(1):126–134, August 2007. ISSN 1600-065X. doi: 10.1111/j.1600-065X.2007.00536.x. URL https://onlinelibrary.wiley.com/doi/10.1111/j.1600-065X.2007.00536.x.

[6] Leo Loeb. Über Regeneration des Epithels. *Archiv für Entwicklungsmechanik der Organismen*, 6(3):297–364, June 1898. ISSN 1432-041X. doi: 10.1007/BF02156714. URL https://doi.org/10.1007/BF02156714.

[7] Ann F. Chambers, Alan C. Groom, and Ian C. MacDonald. Dissemination and growth of cancer cells in metastatic sites. *Nature Reviews Cancer*, 2(8):

563–572, August 2002. ISSN 1474-1768. doi: 10.1038/nrc865. URL `https://www.nature.com/articles/nrc865`.

[8] Jean Aicardi. The Place of Neuronal Migration Abnormalities in Child Neurology. *Canadian Journal of Neurological Sciences*, 21(3):185–193, August 1994. ISSN 0317-1671, 2057-0155. doi: 10.1017/S0317167100041159. URL `https://www.cambridge.org/core/journals/canadian-journal-of-neurological-sciences/article/place-of-neuronal-migration-abnormalities-in-child-neurology/45BC65E7CD36DADD0B4A7D434DA98A2C`.

[9] Stephanie M. Willerth and Shelly E. Sakiyama-Elbert. Cell Therapy for Spinal Cord Regeneration. *Advanced drug delivery reviews*, 60(2):263–276, January 2008. ISSN 0169-409X. doi: 10.1016/j.addr.2007.08.028. URL `https://www.ncbi.nlm.nih.gov/pmc/articles/PMC2225623/`.

[10] Karl Przibram. Über die ungeordnete Bewegung niederer Tiere. *Pflüger's Archiv für die gesamte Physiologie des Menschen und der Tiere*, 153(8):401–405, August 1913. ISSN 1432-2013. doi: 10.1007/BF01686480. URL `https://doi.org/10.1007/BF01686480`.

[11] Reinhold Fürth. Die Brownsche Bewegung bei Berücksichtigung einer Persistenz der Bewegungsrichtung. Mit Anwendungen auf die Bewegung lebender Infusorien. *Zeitschrift für Physik*, 2(3):244–256, June 1920. ISSN 0044-3328. doi: 10.1007/BF01328731. URL `https://doi.org/10.1007/BF01328731`.

[12] Carl Zeiss. *Zeiss-Zeichenprisma, Zeichenapparate nach Abbe*, volume 118 of *Mikro*. Zeiss, Jena, 1931. URL `http://echo.mpiwg-berlin.mpg.de/MPIWG:RUQ0C6PC`. Available as online ressource. Copyright: Max Planck Institute for the History of Science.

[13] Peter Dieterich, Rainer Klages, Roland Preuss, and Albrecht Schwab. Anomalous dynamics of cell migration. *Proceedings of the National Academy of Sciences*, 105(2):459–463, January 2008. ISSN 0027-8424, 1091-6490. doi: 10.1073/pnas.0707603105. URL `https://www.pnas.org/content/105/2/459`.

[14] Goher Mahmud, Christopher J. Campbell, Kyle J. M. Bishop, Yulia A. Komarova, Oleg Chaga, Siowling Soh, Sabil Huda, Kristiana Kandere-

Grzybowska, and Bartosz A. Grzybowski. Directing cell motions on micropatterned ratchets. *Nature Physics*, 5(8):606–612, August 2009. ISSN 1745-2473. doi: 10.1038/nphys1306. URL `http://www.nature.com/nphys/journal/v5/n8/abs/nphys1306.html`.

[15] Jiranuwat Sapudom, Johannes Waschke, Katja Franke, Mario Hlawitschka, and Tilo Pompe. Quantitative label-free single cell tracking in 3D biomimetic matrices. *Scientific Reports*, 7(1):1–9, October 2017. ISSN 2045-2322. doi: 10.1038/s41598-017-14458-x. URL `https://www.nature.com/articles/s41598-017-14458-x`.

[16] Alexandra Murschhauser, Peter J. F. Röttgermann, Daniel Woschée, Martina F. Ober, Yan Yan, Kenneth A. Dawson, and Joachim O. Rädler. A high-throughput microscopy method for single-cell analysis of event-time correlations in nanoparticle-induced cell death. *Communications Biology*, 2(1): 1–11, January 2019. ISSN 2399-3642. doi: 10.1038/s42003-019-0282-0. URL `https://www.nature.com/articles/s42003-019-0282-0`.

[17] Mitchell H. Gail and Charles W. Boone. The Locomotion of Mouse Fibroblasts in Tissue Culture. *Biophysical Journal*, 10(10):980–993, October 1970. ISSN 0006-3495. doi: 10.1016/S0006-3495(70)86347-0. URL `http://www.sciencedirect.com/science/article/pii/S0006349570863470`.

[18] Gargi Maheshwari and Douglas A. Lauffenburger. Deconstructing (and reconstructing) cell migration. *Microscopy Research and Technique*, 43(5):358–368, 1998. ISSN 1097-0029. doi: 10.1002/(SICI)1097-0029(19981201)43:5<358:: AID-JEMT2>3.0.CO;2-D. URL `https://onlinelibrary.wiley.com/doi/abs/10.1002/%28SICI%291097-0029%2819981201%2943%3A5%3C358%3A%3AAID-JEMT2%3E3.0.CO%3B2-D`.

[19] Alka A. Potdar, Junhwan Jeon, Alissa M. Weaver, Vito Quaranta, and Peter T. Cummings. Human Mammary Epithelial Cells Exhibit a Bimodal Correlated Random Walk Pattern. *PLOS ONE*, 5(3):e9636, March 2010. ISSN 1932-6203. doi: 10.1371/journal.pone.0009636. URL `https://journals.plos.org/plosone/article?id=10.1371/journal.pone.0009636`.

[20] David Selmeczi, Stephan Mosler, Peter H. Hagedorn, Niels B. Larsen, and Henrik Flyvbjerg. Cell Motility as Persistent Random Motion: Theories from

Experiments. *Biophysical Journal*, 89(2):912–931, August 2005. ISSN 0006-3495. doi: 10.1529/biophysj.105.061150. URL `http://www.sciencedirect.com/science/article/pii/S0006349505727430`.

[21] Jinghuan Huang, Stefan V. Gräter, Francesca Corbellini, Sabine Rinck, Eva Bock, Ralf Kemkemer, Horst Kessler, Jiandong Ding, and Joachim P. Spatz. Impact of Order and Disorder in RGD Nanopatterns on Cell Adhesion. *Nano Letters*, 9(3):1111–1116, March 2009. ISSN 1530-6984. doi: 10.1021/nl803548b. URL `https://doi.org/10.1021/nl803548b`.

[22] Mark Schvartzman, Matteo Palma, Julia Sable, Justin Abramson, Xian Hu, Michael P. Sheetz, and Shalom J. Wind. Nanolithographic Control of the Spatial Organization of Cellular Adhesion Receptors at the Single-Molecule Level. *Nano Letters*, 11(3):1306–1312, March 2011. ISSN 1530-6984. doi: 10.1021/nl104378f. URL `https://doi.org/10.1021/nl104378f`.

[23] Elisabetta A. Cavalcanti-Adam, Alexandre Micoulet, Jacques Blümmel, Jörg Auernheimer, Horst Kessler, and Joachim P. Spatz. Lateral spacing of integrin ligands influences cell spreading and focal adhesion assembly. *European Journal of Cell Biology*, 85(3):219–224, April 2006. ISSN 0171-9335. doi: 10.1016/j.ejcb.2005.09.011. URL `http://www.sciencedirect.com/science/article/pii/S0171933505001500`.

[24] Marco Arnold, Elisabetta Ada Cavalcanti-Adam, Roman Glass, Jacques Blümmel, Wolfgang Eck, Martin Kantlehner, Horst Kessler, and Joachim P. Spatz. Activation of Integrin Function by Nanopatterned Adhesive Interfaces. *ChemPhysChem*, 5(3):383–388, March 2004. ISSN 1439-7641. doi: 10.1002/cphc.200301014. URL `https://onlinelibrary.wiley.com/doi/abs/10.1002/cphc.200301014`.

[25] J. Vielmetter, B. Stolze, F. Bonhoeffer, and C. a. O. Stuermer. In vitro assay to test differential substrate affinities of growing axons and migratory cells. *Experimental Brain Research*, 81(2):283–287, July 1990. ISSN 0014-4819, 1432-1106. doi: 10.1007/BF00228117. URL `https://link.springer.com/article/10.1007/BF00228117`.

[26] Ross W. Gundersen. Response of sensory neurites and growth cones to patterned substrata of laminin and fibronectin in vitro. *Developmental Biology*,

121(2):423–431, June 1987. ISSN 0012-1606. doi: 10.1016/0012-1606(87)90179-5. URL `http://www.sciencedirect.com/science/article/pii/0012160687901795`.

[27] Amaretta R. Evans, Sara Euteneuer, Eduardo Chavez, Lina M. Mullen, Elliot E. Hui, Sangeeta N. Bhatia, and Allen F. Ryan. Laminin and fibronectin modulate inner ear spiral ganglion neurite outgrowth in an in vitro alternate choice assay. *Developmental Neurobiology*, 67(13):1721–1730, November 2007. ISSN 1932-846X. doi: 10.1002/dneu.20540. URL `https://onlinelibrary.wiley.com/doi/abs/10.1002/dneu.20540`.

[28] Albert Harris. Behavior of cultured cells on substrata of variable adhesiveness. *Experimental Cell Research*, 77(1):285–297, March 1973. ISSN 0014-4827. doi: 10.1016/0014-4827(73)90579-X. URL `http://www.sciencedirect.com/science/article/pii/001448277390579X`.

[29] Stephen Britland, Peter Clark, Patricia Connolly, and Geoffrey Moores. Micropatterned substratum adhesiveness: A model for morphogenetic cues controlling cell behavior. *Experimental Cell Research*, 198(1):124–129, January 1992. ISSN 00144827. doi: 10.1016/0014-4827(92)90157-4. URL `http://linkinghub.elsevier.com/retrieve/pii/0014482792901574`.

[30] Sébastien G. Ricoult, Greta Thompson-Steckel, James P. Correia, Timothy E. Kennedy, and David Juncker. Tuning cell–surface affinity to direct cell specific responses to patterned proteins. *Biomaterials*, 35(2):727–736, January 2014. ISSN 0142-9612. doi: 10.1016/j.biomaterials.2013.10.023. URL `http://www.sciencedirect.com/science/article/pii/S0142961213012532`.

[31] R. Singhvi, A. Kumar, G. P. Lopez, G. N. Stephanopoulos, D. I. Wang, G. M. Whitesides, and D. E. Ingber. Engineering cell shape and function. *Science*, 264(5159):696–698, April 1994. ISSN 0036-8075, 1095-9203. doi: 10.1126/science.8171320. URL `http://science.sciencemag.org/content/264/5159/696`.

[32] Christopher S. Chen, Milan Mrksich, Sui Huang, George M. Whitesides, and Donald E. Ingber. Geometric Control of Cell Life and Death. *Science*, 276(5317):1425–1428, May 1997. ISSN 0036-8075, 1095-9203. doi:

10.1126/science.276.5317.1425. URL `http://www.sciencemag.org/content/276/5317/1425`.

[33] Ammar Azioune, Marko Storch, Michel Bornens, Manuel Théry, and Matthieu Piel. Simple and rapid process for single cell micro-patterning. *Lab on a Chip*, 9(11):1640–1642, 2009. doi: 10.1039/B821581M. URL `https://pubs.rsc.org/en/content/articlelanding/2009/lc/b821581m`.

[34] Ce Yan, Jianguo Sun, and Jiandong Ding. Critical areas of cell adhesion on micropatterned surfaces. *Biomaterials*, 32(16):3931–3938, June 2011. ISSN 0142-9612. doi: 10.1016/j.biomaterials.2011.01.078. URL `http://www.sciencedirect.com/science/article/pii/S0142961211001499`.

[35] Elena Kassianidou, Dimitri Probst, Julia Jäger, Stacey Lee, Anne-Lou Roguet, Ulrich Sebastian Schwarz, and Sanjay Kumar. Extracellular Matrix Geometry and Initial Adhesive Position Determine Stress Fiber Network Organization during Cell Spreading. *Cell Reports*, 27(6):1897–1909.e4, May 2019. ISSN 2211-1247. doi: 10.1016/j.celrep.2019.04.035. URL `http://www.sciencedirect.com/science/article/pii/S2211124719305005`.

[36] Philipp J. Albert and Ulrich S. Schwarz. Dynamics of Cell Shape and Forces on Micropatterned Substrates Predicted by a Cellular Potts Model. *Biophysical Journal*, 106(11):2340–2352, June 2014. ISSN 0006-3495. doi: 10.1016/j.bpj.2014.04.036. URL `http://www.sciencedirect.com/science/article/pii/S0006349514004548`.

[37] Manuel Théry, Victor Racine, Matthieu Piel, Anne Pépin, Ariane Dimitrov, Yong Chen, Jean-Baptiste Sibarita, and Michel Bornens. Anisotropy of cell adhesive microenvironment governs cell internal organization and orientation of polarity. *Proceedings of the National Academy of Sciences*, 103(52):19771–19776, December 2006. ISSN 0027-8424, 1091-6490. doi: 10.1073/pnas.0609267103. URL `https://www.pnas.org/content/103/52/19771`.

[38] Manuel Théry, Anne Pépin, Emilie Dressaire, Yong Chen, and Michel Bornens. Cell distribution of stress fibres in response to the geometry of the adhesive environment. *Cell Motility and the Cytoskeleton*, 63(6):341–355, June 2006. ISSN 0886-1544. doi: 10.1002/cm.20126.

[39] Manuel Théry, Victor Racine, Anne Pépin, Matthieu Piel, Yong Chen, Jean-Baptiste Sibarita, and Michel Bornens. The extracellular matrix guides the orientation of the cell division axis. *Nature Cell Biology*, 7(10):947–953, October 2005. ISSN 1476-4679. doi: 10.1038/ncb1307. URL `https://www.nature.com/articles/ncb1307`.

[40] Manuel Théry, Andrea Jiménez-Dalmaroni, Victor Racine, Michel Bornens, and Frank Jülicher. Experimental and theoretical study of mitotic spindle orientation. *Nature*, 447(7143):493–496, May 2007. ISSN 1476-4687. doi: 10.1038/nature05786. URL `https://www.nature.com/articles/nature05786`.

[41] Jane James, Edgar D. Goluch, Huan Hu, Chang Liu, and Milan Mrksich. Sub-cellular curvature at the perimeter of micropatterned cells influences lamellipodial distribution and cell polarity. *Cell Motility*, 65(11):841–852, 2008. ISSN 1097-0169. doi: 10.1002/cm.20305. URL `https://onlinelibrary.wiley.com/doi/abs/10.1002/cm.20305`.

[42] Peter J. F. Röttgermann, Kenneth A. Dawson, and Joachim O. Rädler. Time-Resolved Study of Nanoparticle Induced Apoptosis Using Microfabricated Single Cell Arrays. *Microarrays*, 5(2):8, June 2016. doi: 10.3390/microarrays5020008. URL `https://www.mdpi.com/2076-3905/5/2/8`.

[43] Mehrije Ferizi, Carolin Leonhardt, Christian Meggle, Manish K. Aneja, Carsten Rudolph, Christian Plank, and Joachim O. Rädler. Stability analysis of chemically modified mRNA using micropattern-based single-cell arrays. *Lab on a Chip*, 15(17):3561–3571, 2015. doi: 10.1039/C5LC00749F. URL `https://pubs.rsc.org/en/content/articlelanding/2015/lc/c5lc00749f`.

[44] Xingyu Jiang, Derek A. Bruzewicz, Amy P. Wong, Matthieu Piel, and George M. Whitesides. Directing cell migration with asymmetric micropatterns. *Proceedings of the National Academy of Sciences*, 102(4):975–978, January 2005. ISSN 0027-8424, 1091-6490. doi: 10.1073/pnas.0408954102. URL `https://www.pnas.org/content/102/4/975`.

[45] Bo Chen, Girish Kumar, Carlos C. Co, and Chia-Chi Ho. Geometric Control of Cell Migration. *Scientific Reports*, 3:2827, October 2013. ISSN 2045-2322. doi: 10.1038/srep02827. URL `https://www.nature.com/articles/srep02827`.

[46] Paolo Maiuri, Emmanuel Terriac, Perrine Paul-Gilloteaux, Timothée Vignaud, Krista McNally, James Onuffer, Kurt Thorn, Phuong A. Nguyen, Nefeli Georgoulia, Daniel Soong, Asier Jayo, Nina Beil, Jürgen Beneke, Joleen Chooi Hong Lim, Chloe Pei-Ying Sim, Yeh-Shiu Chu, Andrea Jiménez-Dalmaroni, Jean-François Joanny, Jean-Paul Thiery, Holger Erfle, Maddy Parsons, Timothy J. Mitchison, Wendell A. Lim, Ana-Maria Lennon-Duménil, Matthieu Piel, and Manuel Théry. The first World Cell Race. *Current Biology*, 22(17):R673–R675, September 2012. ISSN 0960-9822. doi: 10.1016/j.cub.2012.07.052. URL `http://www.sciencedirect.com/science/article/pii/S0960982212008779`.

[47] Christoph Schreiber, Felix J. Segerer, Ernst Wagner, Andreas Roidl, and Joachim O. Rädler. Ring-Shaped Microlanes and Chemical Barriers as a Platform for Probing Single-Cell Migration. *Scientific Reports*, 6:26858, May 2016. URL `http://dx.doi.org/10.1038/srep26858`.

[48] Girish Kumar, Carlos C. Co, and Chia-Chi Ho. Steering Cell Migration Using Microarray Amplification of Natural Directional Persistence. *Langmuir*, 27(7):3803–3807, April 2011. ISSN 0743-7463. doi: 10.1021/la2000206. URL `http://dx.doi.org/10.1021/la2000206`.

[49] David Caballero, Raphaël Voituriez, and Daniel Riveline. Protrusion Fluctuations Direct Cell Motion. *Biophysical Journal*, 107(1):34–42, July 2014. ISSN 0006-3495. doi: 10.1016/j.bpj.2014.05.002. URL `http://www.sciencedirect.com/science/article/pii/S0006349514004688`.

[50] Douglas Hanahan and Robert A. Weinberg. The Hallmarks of Cancer. *Cell*, 100(1):57–70, January 2000. ISSN 0092-8674. doi: 10.1016/S0092-8674(00)81683-9. URL `http://www.sciencedirect.com/science/article/pii/S0092867400816839`.

[51] Douglas Hanahan and Robert A. Weinberg. Hallmarks of Cancer: The Next Generation. *Cell*, 144(5):646–674, March 2011. ISSN 0092-8674. doi: 10.1016/j.cell.2011.02.013. URL `http://www.sciencedirect.com/science/article/pii/S0092867411001279`.

[52] W. G. Jiang, A. J. Sanders, M. Katoh, H. Ungefroren, F. Gieseler, M. Prince, S. K. Thompson, M. Zollo, D. Spano, P. Dhawan, D. Sliva, P. R. Sub-

barayan, M. Sarkar, K. Honoki, H. Fujii, A. G. Georgakilas, A. Amedei, E. Niccolai, A. Amin, S. S. Ashraf, L. Ye, W. G. Helferich, X. Yang, C. S. Boosani, G. Guha, M. R. Ciriolo, K. Aquilano, S. Chen, A. S. Azmi, W. N. Keith, A. Bilsland, D. Bhakta, D. Halicka, S. Nowsheen, F. Pantano, and D. Santini. Tissue invasion and metastasis: Molecular, biological and clinical perspectives. *Seminars in Cancer Biology*, 35:S244–S275, December 2015. ISSN 1044-579X. doi: 10.1016/j.semcancer.2015.03.008. URL `http://www.sciencedirect.com/science/article/pii/S1044579X15000231`.

[53] Colin D. Paul, Panagiotis Mistriotis, and Konstantinos Konstantopoulos. Cancer cell motility: lessons from migration in confined spaces. *Nature Reviews Cancer*, 17(2):131–140, February 2017. ISSN 1474-1768. doi: 10.1038/nrc.2016.123. URL `https://www.nature.com/articles/nrc.2016.123`.

[54] Katarina Wolf, Stephanie Alexander, Vivien Schacht, Lisa M. Coussens, Ulrich H. von Andrian, Jacco van Rheenen, Elena Deryugina, and Peter Friedl. Collagen-based cell migration models in vitro and in vivo. *Seminars in Cell & Developmental Biology*, 20(8):931–941, October 2009. ISSN 1084-9521. doi: 10.1016/j.semcdb.2009.08.005. URL `http://www.sciencedirect.com/science/article/pii/S108495210900161X`.

[55] Katarina Wolf, Mariska te Lindert, Marina Krause, Stephanie Alexander, Joost te Riet, Amanda L. Willis, Robert M. Hoffman, Carl G. Figdor, Stephen J. Weiss, and Peter Friedl. Physical limits of cell migration: Control by ECM space and nuclear deformation and tuning by proteolysis and traction force. *The Journal of Cell Biology*, 201(7):1069–1084, June 2013. ISSN 0021-9525, 1540-8140. doi: 10.1083/jcb.201210152. URL `http://jcb.rupress.org/content/201/7/1069`.

[56] Kacey VanderVorst, Courtney A. Dreyer, Sara E. Konopelski, Hyun Lee, Hsin-Yi Henry Ho, and Kermit L. Carraway. Wnt/PCP Signaling Contribution to Carcinoma Collective Cell Migration and Metastasis. *Cancer Research*, 79(8):1719–1729, April 2019. ISSN 0008-5472, 1538-7445. doi: 10.1158/0008-5472.CAN-18-2757. URL `https://cancerres.aacrjournals.org/content/79/8/1719`.

[57] Veronika te Boekhorst, Luigi Preziosi, and Peter Friedl. Plasticity of Cell

Migration In Vivo and In Silico. *Annual Review of Cell and Developmental Biology*, 32(1):491–526, 2016. doi: 10.1146/annurev-cellbio-111315-125201. URL `https://doi.org/10.1146/annurev-cellbio-111315-125201`.

[58] Katrin Talkenberger, Elisabetta Ada Cavalcanti-Adam, Anja Voss-Böhme, and Andreas Deutsch. Amoeboid-mesenchymal migration plasticity promotes invasion only in complex heterogeneous microenvironments. *Scientific Reports*, 7(1):1–12, August 2017. ISSN 2045-2322. doi: 10.1038/s41598-017-09300-3. URL `https://www.nature.com/articles/s41598-017-09300-3`.

[59] Yan-Jun Liu, Maël Le Berre, Franziska Lautenschlaeger, Paolo Maiuri, Andrew Callan-Jones, Mélina Heuzé, Tohru Takaki, Raphaël Voituriez, and Matthieu Piel. Confinement and Low Adhesion Induce Fast Amoeboid Migration of Slow Mesenchymal Cells. *Cell*, 160(4):659–672, February 2015. ISSN 0092-8674. doi: 10.1016/j.cell.2015.01.007. URL `http://www.sciencedirect.com/science/article/pii/S0092867415000082`.

[60] Ewa K. Paluch and Erez Raz. The role and regulation of blebs in cell migration. *Current Opinion in Cell Biology*, 25(5):582–590, October 2013. ISSN 0955-0674. doi: 10.1016/j.ceb.2013.05.005. URL `http://www.sciencedirect.com/science/article/pii/S0955067413000793`.

[61] K. Paňková, D. Rösel, M. Novotný, and Jan Brábek. The molecular mechanisms of transition between mesenchymal and amoeboid invasiveness in tumor cells. *Cellular and Molecular Life Sciences*, 67(1):63–71, January 2010. ISSN 1420-9071. doi: 10.1007/s00018-009-0132-1. URL `https://doi.org/10.1007/s00018-009-0132-1`.

[62] Anne J. Ridley, Martin A. Schwartz, Keith Burridge, Richard A. Firtel, Mark H. Ginsberg, Gary Borisy, J. Thomas Parsons, and Alan Rick Horwitz. Cell Migration: Integrating Signals from Front to Back. *Science*, 302 (5651):1704–1709, December 2003. ISSN 0036-8075, 1095-9203. doi: 10.1126/science.1092053. URL `https://science.sciencemag.org/content/302/5651/1704`.

[63] A. Ponti, M. Machacek, S. L. Gupton, C. M. Waterman-Storer, and G. Danuser. Two Distinct Actin Networks Drive the Protrusion of Migrating

Cells. *Science*, 305(5691):1782–1786, September 2004. ISSN 0036-8075, 1095-9203. doi: 10.1126/science.1100533. URL `https://science.sciencemag.org/content/305/5691/1782`.

[64] Ariel Livne and Benjamin Geiger. The inner workings of stress fibers - from contractile machinery to focal adhesions and back. *Journal of Cell Science*, 129(7):1293–1304, April 2016. ISSN 0021-9533, 1477-9137. doi: 10.1242/jcs.180927. URL `https://jcs.biologists.org/content/129/7/1293`.

[65] Anne J. Ridley. Rho GTPase signalling in cell migration. *Current Opinion in Cell Biology*, 36:103–112, October 2015. ISSN 0955-0674. doi: 10.1016/j.ceb.2015.08.005. URL `http://www.sciencedirect.com/science/article/pii/S0955067415001106`.

[66] Thomas D. Pollard and Gary G. Borisy. Cellular Motility Driven by Assembly and Disassembly of Actin Filaments. *Cell*, 112(4):453–465, February 2003. ISSN 0092-8674. doi: 10.1016/S0092-8674(03)00120-X. URL `http://www.sciencedirect.com/science/article/pii/S009286740300120X`.

[67] Marcus Prass, Ken Jacobson, Alex Mogilner, and Manfred Radmacher. Direct measurement of the lamellipodial protrusive force in a migrating cell. *The Journal of Cell Biology*, 174(6):767–772, September 2006. ISSN 0021-9525. doi: 10.1083/jcb.200601159. URL `https://rupress.org/jcb/article/174/6/767/44523/Direct-measurement-of-the-lamellipodial-protrusive`.

[68] A. Mogilner and G. Oster. Cell motility driven by actin polymerization. *Biophysical Journal*, 71(6):3030–3045, December 1996. ISSN 0006-3495. doi: 10.1016/S0006-3495(96)79496-1. URL `http://www.sciencedirect.com/science/article/pii/S0006349596794961`.

[69] Tatyana M. Svitkina, Alexander B. Verkhovsky, Kyle M. McQuade, and Gary G. Borisy. Analysis of the Actin–Myosin II System in Fish Epidermal Keratocytes: Mechanism of Cell Body Translocation. *The Journal of Cell Biology*, 139(2):397–415, October 1997. ISSN 0021-9525. doi: 10.1083/jcb.139.2.397. URL `https://rupress.org/jcb/article/139/2/397/47814/Analysis-of-the-Actin-Myosin-II-System-in-Fish`.

[70] Boris Rubinstein, Maxime F. Fournier, Ken Jacobson, Alexander B. Verkhovsky, and Alex Mogilner. Actin-Myosin Viscoelastic Flow in the Keratocyte Lamellipod. *Biophysical Journal*, 97(7):1853–1863, October 2009. ISSN 0006-3495. doi: 10.1016/j.bpj.2009.07.020. URL `http://www.sciencedirect.com/science/article/pii/S0006349509012417`.

[71] Erin Barnhart, Kun-Chun Lee, Greg M. Allen, Julie A. Theriot, and Alex Mogilner. Balance between cell-substrate adhesion and myosin contraction determines the frequency of motility initiation in fish keratocytes. *Proceedings of the National Academy of Sciences*, 112(16):5045–5050, April 2015. ISSN 0027-8424, 1091-6490. doi: 10.1073/pnas.1417257112. URL `https://www.pnas.org/content/112/16/5045`.

[72] Alexander B. Verkhovsky. The mechanisms of spatial and temporal patterning of cell-edge dynamics. *Current Opinion in Cell Biology*, 36:113–121, October 2015. ISSN 0955-0674. doi: 10.1016/j.ceb.2015.09.001. URL `http://www.sciencedirect.com/science/article/pii/S0955067415001118`.

[73] Tim Mitchison and Marc Kirschner. Cytoskeletal dynamics and nerve growth. *Neuron*, 1(9):761–772, November 1988. ISSN 0896-6273. doi: 10.1016/0896-6273(88)90124-9. URL `http://www.sciencedirect.com/science/article/pii/0896627388901249`.

[74] Lindsay B. Case and Clare M. Waterman. Integration of actin dynamics and cell adhesion by a three-dimensional, mechanosensitive molecular clutch. *Nature Cell Biology*, 17(8):955–963, August 2015. ISSN 1476-4679. doi: 10.1038/ncb3191. URL `https://www.nature.com/articles/ncb3191`.

[75] Olivier Pertz, Louis Hodgson, Richard L. Klemke, and Klaus M. Hahn. Spatiotemporal dynamics of RhoA activity in migrating cells. *Nature*, 440(7087):1069–1072, April 2006. ISSN 1476-4687. doi: 10.1038/nature04665. URL `https://www.nature.com/articles/nature04665`.

[76] Alan Rick Horwitz and J. Thomas Parsons. Cell Migration–Movin' On. *Science*, 286(5442):1102–1103, November 1999. ISSN 0036-8075, 1095-9203. doi: 10.1126/science.286.5442.1102. URL `https://science.sciencemag.org/content/286/5442/1102`.

[77] Matthias Machacek, Louis Hodgson, Christopher Welch, Hunter Elliott, Olivier Pertz, Perihan Nalbant, Amy Abell, Gary L. Johnson, Klaus M. Hahn, and Gaudenz Danuser. Coordination of Rho GTPase activities during cell protrusion. *Nature*, 461(7260):99–103, September 2009. ISSN 1476-4687. doi: 10. 1038/nature08242. URL `https://www.nature.com/articles/nature08242`.

[78] Keith Burridge and Krister Wennerberg. Rho and Rac Take Center Stage. *Cell*, 116(2):167–179, January 2004. ISSN 0092-8674. doi: 10.1016/ S0092-8674(04)00003-0. URL `http://www.sciencedirect.com/science/ article/pii/S0092867404000030`.

[79] Ryan J. Petrie, Andrew D. Doyle, and Kenneth M. Yamada. Random versus directionally persistent cell migration. *Nature Reviews Molecular Cell Biology*, 10(8):538–549, August 2009. ISSN 1471-0080. doi: 10.1038/nrm2729. URL `https://www.nature.com/articles/nrm2729`.

[80] Paul Weiss. Cellular Dynamics. *Reviews of Modern Physics*, 31(1):11–20, January 1959. doi: 10.1103/RevModPhys.31.11. URL `https://link.aps. org/doi/10.1103/RevModPhys.31.11`.

[81] S. B. Carter. Principles of Cell Motility: The Direction of Cell Movement and Cancer Invasion. *Nature*, 208(5016):1183–1187, December 1965. ISSN 1476- 4687. doi: 10.1038/2081183a0. URL `https://www.nature.com/articles/ 2081183a0`.

[82] Chun-Min Lo, Hong-Bei Wang, Micah Dembo, and Yu-li Wang. Cell Movement Is Guided by the Rigidity of the Substrate. *Biophysical Journal*, 79(1):144–152, July 2000. ISSN 0006-3495. doi: 10.1016/S0006-3495(00)76279-5. URL `http: //www.sciencedirect.com/science/article/pii/S0006349500762795`.

[83] Morton McCutcheon. Chemotaxis in leukocytes. *Physiological Reviews*, 26 (3):319–336, July 1946. ISSN 0031-9333. doi: 10.1152/physrev.1946.26.3. 319. URL `https://www.physiology.org/doi/abs/10.1152/physrev.1946. 26.3.319`.

[84] Lionel F. Jaffe and Joseph W. Vanable. Electric fields and wound healing. *Clinics in Dermatology*, 2(3):34–44, July 1984. ISSN 0738-081X.

doi: 10.1016/0738-081X(84)90025-7. URL `http://www.sciencedirect.com/science/article/pii/0738081X84900257`.

[85] Laura Lara Rodriguez and Ian C. Schneider. Directed cell migration in multi-cue environments. *Integrative Biology*, 5(11):1306–1323, November 2013. doi: 10.1039/c3ib40137e. URL `https://academic-oup-com.emedien.ub.uni-muenchen.de/ib/article/5/11/1306/5204235`.

[86] M. Machacek and G. Danuser. Morphodynamic Profiling of Protrusion Phenotypes. *Biophysical Journal*, 90(4):1439–1452, February 2006. ISSN 0006-3495. doi: 10.1529/biophysj.105.070383. URL `http://www.sciencedirect.com/science/article/pii/S0006349506723347`.

[87] Erin L. Barnhart, Jun Allard, Sunny S. Lou, Julie A. Theriot, and Alex Mogilner. Adhesion-Dependent Wave Generation in Crawling Cells. *Current Biology*, 27(1):27–38, January 2017. ISSN 0960-9822. doi: 10.1016/j.cub.2016.11.011. URL `http://www.sciencedirect.com/science/article/pii/S0960982216313367`.

[88] Grégory Giannone, Benjamin J. Dubin-Thaler, Hans-Günther Döbereiner, Nelly Kieffer, Anne R. Bresnick, and Michael P. Sheetz. Periodic Lamellipodial Contractions Correlate with Rearward Actin Waves. *Cell*, 116(3):431–443, February 2004. ISSN 0092-8674. doi: 10.1016/S0092-8674(04)00058-3. URL `http://www.sciencedirect.com/science/article/pii/S0092867404000583`.

[89] Cody Reeves, Benjamin Winkler, Falko Ziebert, and Igor S. Aranson. Rotating lamellipodium waves in polarizing cells. *Communications Physics*, 1(1):1–11, November 2018. ISSN 2399-3650. doi: 10.1038/s42005-018-0075-7. URL `https://www.nature.com/articles/s42005-018-0075-7`.

[90] Juliane Zimmermann and Martin Falcke. Formation of Transient Lamellipodia. *PLOS ONE*, 9(2):e87638, February 2014. ISSN 1932-6203. doi: 10.1371/journal.pone.0087638. URL `https://journals.plos.org/plosone/article?id=10.1371/journal.pone.0087638`.

[91] Yoichiro Mori, Alexandra Jilkine, and Leah Edelstein-Keshet. Wave-Pinning and Cell Polarity from a Bistable Reaction-Diffusion System. *Biophysical Journal*, 94(9):3684–3697, May 2008. ISSN 0006-3495. doi: 10.1529/biophysj.

107.120824. URL `http://www.sciencedirect.com/science/article/pii/S0006349508704442`.

[92] Nir S. Gov and Ajay Gopinathan. Dynamics of Membranes Driven by Actin Polymerization. *Biophysical Journal*, 90(2):454–469, January 2006. ISSN 0006-3495. doi: 10.1529/biophysj.105.062224. URL `http://www.sciencedirect.com/science/article/pii/S0006349506722263`.

[93] F. J. Segerer, P. J. F. Röttgermann, S. Schuster, A. Piera Alberola, S. Zahler, and J. O. Rädler. Versatile method to generate multiple types of micropatterns. *Biointerphases*, 11(1):011005, March 2016. ISSN 1934-8630, 1559-4106. doi: 10.1116/1.4940703. URL `http://scitation.aip.org/content/avs/journal/bip/11/1/10.1116/1.4940703`.

[94] James L. Wilbur, Amit Kumar, Hans A. Biebuyck, Enoch Kim, and George M. Whitesides. Microcontact printing of self-assembled monolayers: applications in microfabrication. *Nanotechnology*, 7(4):452–457, December 1996. ISSN 0957-4484. doi: 10.1088/0957-4484/7/4/028. URL `https://doi.org/10.1088%2F0957-4484%2F7%2F4%2F028`.

[95] Sami Alom Ruiz and Christopher S. Chen. Microcontact printing: A tool to pattern. *Soft Matter*, 3(2):168–177, January 2007. ISSN 1744-6848. doi: 10.1039/B613349E. URL `http://pubs.rsc.org/en/content/articlelanding/2007/sm/b613349e`.

[96] Manuel Théry and Matthieu Piel. Adhesive Micropatterns for Cells: A Microcontact Printing Protocol. *Cold Spring Harbor Protocols*, 2009(7): pdb.prot5255, January 2009. ISSN 1940-3402, 1559-6095. doi: 10.1101/pdb.prot5255. URL `http://cshprotocols.cshlp.org/content/2009/7/pdb.prot5255`.

[97] Bryan A. Langowski and Kathryn E. Uhrich. Microscale Plasma-Initiated Patterning (μPIP). *Langmuir*, 21(23):10509–10514, November 2005. ISSN 0743-7463. doi: 10.1021/la052222m. URL `https://doi.org/10.1021/la052222m`.

[98] Anna Tourovskaia, Thomas Barber, Bronwyn T. Wickes, Danny Hirdes, Boris Grin, David G. Castner, Kevin E. Healy, and Albert Folch. Micropatterns of Chemisorbed Cell Adhesion-Repellent Films Using Oxygen Plasma Etching

and Elastomeric Masks. *Langmuir*, 19(11):4754–4764, May 2003. ISSN 0743-7463. doi: 10.1021/la0267948. URL https://doi.org/10.1021/la0267948.

[99] Remigio Picone, Buzz Baum, and Rachel McKendry. Chapter 5 - Plasma Microcontact Patterning (PμCP): A Technique for the Precise Control of Surface Patterning at Small-Scale. In Matthieu Piel and Manuel Théry, editors, *Methods in Cell Biology*, volume 119 of *Micropatterning in Cell Biology Part A*, pages 73–90. Academic Press, January 2014. doi: 10.1016/B978-0-12-416742-1.00005-6. URL http://www.sciencedirect.com/science/article/pii/B9780124167421000056.

[100] Q. Cheng and K. Komvopoulos. Integration of plasma-assisted surface chemical modification, soft lithography, and protein surface activation for single-cell patterning. *Applied Physics Letters*, 97(4):043705, July 2010. ISSN 0003-6951. doi: 10.1063/1.3462326. URL http://aip.scitation.org/doi/10.1063/1.3462326.

[101] Michael Junkin and Pak Kin Wong. Probing cell migration in confined environments by plasma lithography. *Biomaterials*, 32(7):1848–1855, March 2011. ISSN 0142-9612. doi: 10.1016/j.biomaterials.2010.11.009. URL http://www.sciencedirect.com/science/article/pii/S0142961210014316.

[102] Amandine MC Egea, Emmanuelle Trévisiol, and Christophe Vieu. Direct patterning of probe proteins on an antifouling PLL-g-dextran coating for reducing the background signal of fluorescent immunoassays. *Biointerphases*, 8(1):37, December 2013. ISSN 1559-4106. doi: 10.1186/1559-4106-8-37. URL https://doi.org/10.1186/1559-4106-8-37.

[103] Peter J. F. Röttgermann, Alicia Piera Alberola, and Joachim O. Rädler. Cellular self-organization on micro-structured surfaces. *Soft Matter*, 10(14):2397–2404, March 2014. ISSN 1744-6848. doi: 10.1039/C3SM52419A. URL https://pubs.rsc.org/en/content/articlelanding/2014/sm/c3sm52419a.

[104] Fabrice Senger, Amandine Pitaval, Hajer Ennomani, Laetitia Kurzawa, Laurent Blanchoin, and Manuel Théry. Spatial integration of mechanical forces by α-actinin establishes actin network symmetry. *Journal of Cell Science*, 132(22), November 2019. ISSN 0021-9533, 1477-9137. doi: 10.1242/jcs.236604. URL https://jcs.biologists.org/content/132/22/jcs236604.

[105] Yoran Margaron, Tomoaki Nagai, Laurent Guyon, Laetitia Kurzawa, Anne-Pierre Morel, Alice Pinheiro, Laurent Blanchoin, Fabien Reyal, Alain Puisieux, and Manuel Théry. Biophysical properties of intermediate states of EMT outperform both epithelial and mesenchymal states. *bioRxiv*, page 797654, October 2019. doi: 10.1101/797654. URL `https://www.biorxiv.org/content/10.1101/797654v1`.

[106] D. Selmeczi, L. Li, L. I.I. Pedersen, S. F. Nrrelykke, P. H. Hagedorn, S. Mosler, N. B. Larsen, E. C. Cox, and H. Flyvbjerg. Cell motility as random motion: A review. *The European Physical Journal Special Topics*, 157(1):1–15, April 2008. ISSN 1951-6401. doi: 10.1140/epjst/e2008-00626-x. URL `https://doi.org/10.1140/epjst/e2008-00626-x`.

[107] Pei-Hsun Wu, Anjil Giri, Sean X. Sun, and Denis Wirtz. Three-dimensional cell migration does not follow a random walk. *Proceedings of the National Academy of Sciences*, 111(11):3949–3954, March 2014. ISSN 0027-8424, 1091-6490. doi: 10.1073/pnas.1318967111. URL `https://www.pnas.org/content/111/11/3949`.

[108] Brian A. Camley and Wouter-Jan Rappel. Velocity alignment leads to high persistence in confined cells. *Physical Review E*, 89(6):062705, June 2014. doi: 10.1103/PhysRevE.89.062705. URL `https://link.aps.org/doi/10.1103/PhysRevE.89.062705`.

[109] M. Le Berre, Yan-Jun Liu, J. Hu, Paolo Maiuri, O. Bénichou, R. Voituriez, Y. Chen, and M. Piel. Geometric Friction Directs Cell Migration. *Physical Review Letters*, 111(19):198101, November 2013. doi: 10.1103/PhysRevLett.111.198101. URL `https://link.aps.org/doi/10.1103/PhysRevLett.111.198101`.

[110] Brian A. Camley, Yanxiang Zhao, Bo Li, Herbert Levine, and Wouter-Jan Rappel. Periodic Migration in a Physical Model of Cells on Micropatterns. *Physical Review Letters*, 111(15):158102, October 2013. doi: 10.1103/PhysRevLett.111.158102. URL `https://link.aps.org/doi/10.1103/PhysRevLett.111.158102`.

[111] Fang Zhou, Sophia A. Schaffer, Christoph Schreiber, Felix J. Segerer, Andriy Goychuk, Erwin Frey, and Joachim O. Rädler. Quasi-periodic migra-

tion of single cells on short microlanes. *bioRxiv*, page 809939, October 2019. doi: 10.1101/809939. URL `https://www.biorxiv.org/content/10.1101/809939v1`.

[112] Bodo Borm, Robert P. Requardt, Volker Herzog, and Gregor Kirfel. Membrane ruffles in cell migration: indicators of inefficient lamellipodia adhesion and compartments of actin filament reorganization. *Experimental Cell Research*, 302(1):83–95, January 2005. ISSN 0014-4827. doi: 10.1016/j.yexcr. 2004.08.034. URL `http://www.sciencedirect.com/science/article/pii/S0014482704005142`.

[113] German Collection of Microorganisms and Cell Cultures GmbH. MDA-MB-231 (ACC 732) cell line. URL `https://www.dsmz.de/collection/catalogue/details/culture/ACC-732`. Accessed on 9.11.2019.

[114] Connie L. Sommers, Stephen W. Byers, Erik W. Thompson, Jeffrey A. Torri, and Edward P. Gelmann. Differentiation state and invasiveness of human breast cancer cell lines. *Breast Cancer Research and Treatment*, 31(2):325–335, January 1994. ISSN 1573-7217. doi: 10.1007/BF00666165. URL `https://doi.org/10.1007/BF00666165`.

[115] Linda A. Gordon, Kellie T. Mulligan, Helen Maxwell-Jones, Matthew Adams, Rosemary A. Walker, and J. Louise Jones. Breast cell invasive potential relates to the myoepithelial phenotype. *International Journal of Cancer*, 106(1):8–16, August 2003. ISSN 0020-7136. doi: 10.1002/ijc.11172. URL `https://onlinelibrary.wiley.com/doi/full/10.1002/ijc.11172`.

[116] LGC Standards and ATCC. MCF 10A ATCC CRL-10317 Homo sapiens mammary gland cell line, website accessed on 9.11.2019. URL `https://www.lgcstandards-atcc.org/Global/Products/1/6/3/A/CRL-10317.aspx`.

[117] LGC Standards and ATCC. MDA-MB-436 ATCC HTB-130 Homo sapiens mammary gland cell line, website accessed on 9.11.2019. URL `https://www.lgcstandards-atcc.org/Global/Products/3/A/6/1/HTB-130.aspx`.

[118] LGC Standards and ATCC. MDCK (NBL-2) ATCC CCL-34 Canis familiaris kidney normal cell line, website accessed on 9.11.2019. URL `https://www.lgcstandards-atcc.org/en/Global/Products/7/A/9/7/CCL-34.aspx`.

[119] J. Behrens, M. M. Mareel, F. M. Van Roy, and W. Birchmeier. Dissecting tumor cell invasion: epithelial cells acquire invasive properties after the loss of uvomorulin-mediated cell-cell adhesion. *The Journal of Cell Biology*, 108 (6):2435–2447, June 1989. ISSN 0021-9525, 1540-8140. doi: 10.1083/jcb.108. 6.2435. URL `http://jcb.rupress.org/content/108/6/2435`.

[120] LGC Standards and ATCC. A549 ATCC CCL-185 Homo sapiens epithelial lung cell line, website accessed on 9.11.2019. URL `https://www.lgcstandards-atcc.org/Global/Products/D/A/D/6/CCL-185.aspx`.

[121] A. Bruckner, A. E. Filderman, J. C. Kirchheimer, B. R. Binder, and H. G. Remold. Endogenous Receptor-bound Urokinase Mediates Tissue Invasion of the Human Lung Carcinoma Cell Lines A549 and Calu-1. *Cancer Research*, 52(11):3043–3047, June 1992. ISSN 0008-5472, 1538-7445. URL `https://cancerres.aacrjournals.org/content/52/11/3043`.

[122] I.A.Z. Institut für angewandte Zellkultur. HuH7 human liver carcinoma cell line. URL `http://www.i-a-z-zellkultur.de/institut/zelllinien.html`. Accessed on 9.11.2019.

[123] Jing Su, Qing Wang, Yiping Liu, and Meizuo Zhong. miR-217 inhibits invasion of hepatocellular carcinoma cells through direct suppression of E2F3. *Molecular and Cellular Biochemistry*, 392(1):289–296, July 2014. ISSN 1573-4919. doi: 10.1007/s11010-014-2039-x. URL `https://doi.org/10.1007/s11010-014-2039-x`.

[124] Oliver Jonas, Claudia T. Mierke, and Josef A. Käs. Invasive cancer cell lines exhibit biomechanical properties that are distinct from their noninvasive counterparts. *Soft Matter*, 7(24):11488–11495, 2011. doi: 10.1039/C1SM05532A. URL `http://pubs.rsc.org/en/content/articlelanding/2011/sm/c1sm05532a`.

[125] Fu-Shi Quan and Kyung Sook Kim. Medical applications of the intrinsic mechanical properties of single cells. *Acta Biochimica et Biophysica Sinica*, 48(10): 865–871, October 2016. ISSN 1672-9145. doi: 10.1093/abbs/gmw081. URL `https://academic.oup.com/abbs/article/48/10/865/2388990`.

[126] Felix J. Segerer, Florian Thüroff, Alicia Piera Alberola, Erwin Frey, and Joachim O. Rädler. Emergence and Persistence of Collective Cell Migration on Small Circular Micropatterns. *Physical Review Letters*, 114(22): 228102, June 2015. doi: 10.1103/PhysRevLett.114.228102. URL `https://link.aps.org/doi/10.1103/PhysRevLett.114.228102`.

[127] Yansheng Liu, Yang Mi, Torsten Mueller, Saskia Kreibich, Evan G. Williams, Audrey Van Drogen, Christelle Borel, Max Frank, Pierre-Luc Germain, Isabell Bludau, Martin Mehnert, Michael Seifert, Mario Emmenlauer, Isabel Sorg, Fedor Bezrukov, Frederique Sloan Bena, Hu Zhou, Christoph Dehio, Giuseppe Testa, Julio Saez-Rodriguez, Stylianos E. Antonarakis, Wolf-Dietrich Hardt, and Ruedi Aebersold. Multi-omic measurements of heterogeneity in HeLa cells across laboratories. *Nature Biotechnology*, 37(3):314–322, March 2019. ISSN 1546-1696. doi: 10.1038/s41587-019-0037-y. URL `https://www.nature.com/articles/s41587-019-0037-y`.

[128] Uri Ben-David, Benjamin Siranosian, Gavin Ha, Helen Tang, Yaara Oren, Kunihiko Hinohara, Craig A. Strathdee, Joshua Dempster, Nicholas J. Lyons, Robert Burns, Anwesha Nag, Guillaume Kugener, Beth Cimini, Peter Tsvetkov, Yosef E. Maruvka, Ryan O'Rourke, Anthony Garrity, Andrew A. Tubelli, Pratiti Bandopadhayay, Aviad Tsherniak, Francisca Vazquez, Bang Wong, Chet Birger, Mahmoud Ghandi, Aaron R. Thorner, Joshua A. Bittker, Matthew Meyerson, Gad Getz, Rameen Beroukhim, and Todd R. Golub. Genetic and transcriptional evolution alters cancer cell line drug response. *Nature*, 560(7718):325–330, August 2018. ISSN 1476-4687. doi: 10.1038/s41586-018-0409-3. URL `https://www.nature.com/articles/s41586-018-0409-3`.

[129] Alex Sigal, Ron Milo, Ariel Cohen, Naama Geva-Zatorsky, Yael Klein, Yuvalal Liron, Nitzan Rosenfeld, Tamar Danon, Natalie Perzov, and Uri Alon. Variability and memory of protein levels in human cells. *Nature*, 444(7119):643–646, November 2006. ISSN 1476-4687. doi: 10.1038/nature05316. URL `https://www.nature.com/articles/nature05316`.

[130] Mario Niepel, Sabrina L. Spencer, and Peter K. Sorger. Non-genetic cell-to-cell variability and the consequences for pharmacology. *Current opinion in chemical biology*, 13(5-6):556–561, December 2009. ISSN 1367-5931.

doi: 10.1016/j.cbpa.2009.09.015. URL `https://www.ncbi.nlm.nih.gov/pmc/articles/PMC2975492/`.

[131] Ken Webb, Vladimir Hlady, and Patrick A. Tresco. Relationships among cell attachment, spreading, cytoskeletal organization, and migration rate for anchorage-dependent cells on model surfaces. *Journal of Biomedical Materials Research*, 49(3):362–368, 2000. ISSN 1097-4636. doi: 10.1002/(SICI)1097-4636(20000305)49:3<362::AID-JBM9>3.0.CO;2-S. URL `https://onlinelibrary.wiley.com/doi/abs/10.1002/%28SICI%291097-4636%2820000305%2949%3A3%3C362%3A%3AAID-JBM9%3E3.0.CO%3B2-S`.

[132] Danahe Mohammed, Guillaume Charras, Eléonore Vercruysse, Marie Versaevel, Joséphine Lantoine, Laura Alaimo, Céline Bruyère, Marine Luciano, Karine Glinel, Geoffrey Delhaye, Olivier Théodoly, and Sylvain Gabriele. Substrate area confinement is a key determinant of cell velocity in collective migration. *Nature Physics*, 15(8):858–866, August 2019. ISSN 1745-2481. doi: 10.1038/s41567-019-0543-3. URL `https://www.nature.com/articles/s41567-019-0543-3`.

[133] Benoit Vianay, Jos Käfer, Emmanuelle Planus, Marc Block, François Graner, and Hervé Guillou. Single Cells Spreading on a Protein Lattice Adopt an Energy Minimizing Shape. *Physical Review Letters*, 105(12):128101, September 2010. doi: 10.1103/PhysRevLett.105.128101. URL `http://link.aps.org/doi/10.1103/PhysRevLett.105.128101`.

[134] Dapeng Bi, Jorge H. Lopez, J. M. Schwarz, and M. Lisa Manning. Energy barriers and cell migration in densely packed tissues. *Soft Matter*, 10(12):1885–1890, February 2014. ISSN 1744-6848. doi: 10.1039/C3SM52893F. URL `https://pubs.rsc.org/en/content/articlelanding/2014/sm/c3sm52893f`.

[135] Jordi Comelles, David Caballero, Raphaël Voituriez, Verónica Hortigüela, Viktoria Wollrab, Amélie Luise Godeau, Josep Samitier, Elena Martínez, and Daniel Riveline. Cells as Active Particles in Asymmetric Potentials: Motility under External Gradients. *Biophysical Journal*, 107(7):1513–1522, Oc-

tober 2014. ISSN 0006-3495. doi: 10.1016/j.bpj.2014.08.001. URL `http://www.sciencedirect.com/science/article/pii/S0006349514008054`.

[136] Philipp J. Albert and Ulrich S. Schwarz. Modeling cell shape and dynamics on micropatterns. *Cell Adhesion & Migration*, 10(5):516–528, September 2016. ISSN 1933-6918. doi: 10.1080/19336918.2016.1148864. URL `http://dx.doi.org/10.1080/19336918.2016.1148864`.

[137] Pascal Martin, D. Bozovic, Y. Choe, and A. J. Hudspeth. Spontaneous Oscillation by Hair Bundles of the Bullfrog's Sacculus. *Journal of Neuroscience*, 23(11):4533–4548, June 2003. ISSN 0270-6474, 1529-2401. doi: 10.1523/JNEUROSCI.23-11-04533.2003. URL `https://www.jneurosci.org/content/23/11/4533`.

[138] Chuan-Hsiang Huang, Ming Tang, Changji Shi, Pablo A. Iglesias, and Peter N. Devreotes. An excitable signal integrator couples to an idling cytoskeletal oscillator to drive cell migration. *Nature Cell Biology*, 15(11):1307–1316, November 2013. ISSN 1476-4679. doi: 10.1038/ncb2859. URL `https://www.nature.com/articles/ncb2859`.

[139] B. Szabó, Zs Környei, J. Zách, D. Selmeczi, G. Csúcs, A. Czirók, and T. Vicsek. Auto-reverse nuclear migration in bipolar mammalian cells on micropatterned surfaces. *Cell Motility*, 59(1):38–49, 2004. ISSN 1097-0169. doi: 10.1002/cm.20022. URL `https://onlinelibrary.wiley.com/doi/abs/10.1002/cm.20022`.

[140] Stephanie I. Fraley, Yunfeng Feng, Anjil Giri, Gregory D. Longmore, and Denis Wirtz. Dimensional and temporal controls of three-dimensional cell migration by zyxin and binding partners. *Nature Communications*, 3(1):1–13, March 2012. ISSN 2041-1723. doi: 10.1038/ncomms1711. URL `https://www.nature.com/articles/ncomms1711`.

[141] Simon Lo Vecchio, Raghavan Thiagarajan, David Caballero, Vincent Vigon, Laurent Navoret, Raphaël Voituriez, and Daniel Riveline. Cell motion as a stochastic process controlled by focal contacts dynamics. *bioRxiv*, page 750331, August 2019. doi: 10.1101/750331. URL `https://www.biorxiv.org/content/10.1101/750331v1`.

[142] Andrew D. Doyle, Francis W. Wang, Kazue Matsumoto, and Kenneth M. Yamada. One-dimensional topography underlies three-dimensional fibrillar cell migration. *The Journal of Cell Biology*, 184(4):481–490, February 2009. ISSN 0021-9525, 1540-8140. doi: 10.1083/jcb.200810041. URL http://jcb.rupress.org/content/184/4/481.

[143] Simon L. Schuster, Felix J. Segerer, Florian A. Gegenfurtner, Kerstin Kick, Christoph Schreiber, Max Albert, Angelika M. Vollmar, Joachim O. Rädler, and Stefan Zahler. Contractility as a global regulator of cellular morphology, velocity, and directionality in low-adhesive fibrillary micro-environments. *Biomaterials*, 102:137–147, September 2016. ISSN 0142-9612. doi: 10.1016/j.biomaterials.2016.06.021. URL http://www.sciencedirect.com/science/article/pii/S0142961216302757.

[144] Keiichiro Kushiro, Stephanie Chang, and Anand R. Asthagiri. Reprogramming Directional Cell Motility by Tuning Micropattern Features and Cellular Signals. *Advanced Materials*, 22(40):4516–4519, October 2010. ISSN 1521-4095. doi: 10.1002/adma.201001619. URL http://onlinelibrary.wiley.com/doi/10.1002/adma.201001619/abstract.

[145] Stephanie S. Chang, Wei-hui Guo, Youngeun Kim, and Yu-li Wang. Guidance of Cell Migration by Substrate Dimension. *Biophysical Journal*, 104(2):313–321, January 2013. ISSN 0006-3495. doi: 10.1016/j.bpj.2012.12.001. URL http://www.sciencedirect.com/science/article/pii/S0006349512050795.

[146] Pere Roca-Cusachs, Jordi Alcaraz, Raimon Sunyer, Josep Samitier, Ramon Farré, and Daniel Navajas. Micropatterning of Single Endothelial Cell Shape Reveals a Tight Coupling between Nuclear Volume in G1 and Proliferation. *Biophysical Journal*, 94(12):4984–4995, June 2008. ISSN 0006-3495. doi: 10.1529/biophysj.107.116863. URL http://www.sciencedirect.com/science/article/pii/S000634950870362X.

[147] Stefan Nehls, Helen Nöding, Susanne Karsch, Franziska Ries, and Andreas Janshoff. Stiffness of MDCK II Cells Depends on Confluency and Cell Size. *Biophysical Journal*, 116(11):2204–2211, June 2019. ISSN 0006-3495. doi:

10.1016/j.bpj.2019.04.028. URL `http://www.sciencedirect.com/science/article/pii/S0006349519303625`.

[148] Sean P. Palecek, Joseph C. Loftus, Mark H. Ginsberg, Douglas A. Lauffen-burger, and Alan F. Horwitz. Integrin-ligand binding properties govern cell migration speed through cell-substratum adhesiveness. *Nature*, 385(6616): 537–540, February 1997. ISSN 1476-4687. doi: 10.1038/385537a0. URL `https://www.nature.com/articles/385537a0`.

[149] Ming Guo, Adrian F. Pegoraro, Angelo Mao, Enhua H. Zhou, Praveen R. Arany, Yulong Han, Dylan T. Burnette, Mikkel H. Jensen, Karen E. Kasza, Jeffrey R. Moore, Frederick C. Mackintosh, Jeffrey J. Fredberg, David J. Mooney, Jennifer Lippincott-Schwartz, and David A. Weitz. Cell volume change through water efflux impacts cell stiffness and stem cell fate. *Proceedings of the National Academy of Sciences*, 114(41):E8618–E8627, October 2017. ISSN 0027-8424, 1091-6490. doi: 10.1073/pnas.1705179114. URL `https://www.pnas.org/content/114/41/E8618`.

[150] Vinay Swaminathan, Karthikeyan Mythreye, E. Tim O'Brien, Andrew Berchuck, Gerard C. Blobe, and Richard Superfine. Mechanical Stiffness Grades Metastatic Potential in Patient Tumor Cells and in Cancer Cell Lines. *Cancer Research*, 71(15):5075–5080, August 2011. ISSN 0008-5472, 1538-7445. doi: 10.1158/0008-5472.CAN-11-0247. URL `https://cancerres.aacrjournals.org/content/71/15/5075`.

[151] Kevin Kit Parker, Amy Lepre Brock, Cliff Brangwynne, Robert J. Mannix, Ning Wang, Emanuele Ostuni, Nicholas A. Geisse, Josephine C. Adams, George M. Whitesides, and Donald E. Ingber. Directional control of lamellipodia extension by constraining cell shape and orienting cell tractional forces. *The FASEB Journal*, 16(10):1195–1204, January 2002. ISSN 0892-6638, 1530-6860. doi: 10.1096/fj.02-0038com. URL `http://www.fasebj.org/content/16/10/1195`.

[152] David Caballero, Raphaël Voituriez, and Daniel Riveline. The cell ratchet: Interplay between efficient protrusions and adhesion determines cell motion. *Cell Adhesion & Migration*, 9(5):327–334, September 2015. ISSN 1933-

6918. doi: 10.1080/19336918.2015.1061865. URL `https://doi.org/10.1080/19336918.2015.1061865`.

[153] Kristiana Kandere-Grzybowska, Siowling Soh, Goher Mahmud, Yulia Komarova, Didzis Pilans, and Bartosz A. Grzybowski. Short-term molecular polarization of cells on symmetric and asymmetric micropatterns. *Soft Matter*, 6(14):3257–3268, 2010. doi: 10.1039/B922647H. URL `http://pubs.rsc.org/en/content/articlelanding/2010/sm/b922647h`.

[154] Dapeng Bi, Xingbo Yang, M. Cristina Marchetti, and M. Lisa Manning. Motility-Driven Glass and Jamming Transitions in Biological Tissues. *Physical Review X*, 6(2):021011, April 2016. doi: 10.1103/PhysRevX.6.021011. URL `https://link.aps.org/doi/10.1103/PhysRevX.6.021011`.

[155] Amy Brock, Eric Chang, Chia-Chi Ho, Philip LeDuc, Xingyu Jiang, George M. Whitesides, and Donald E. Ingber. Geometric Determinants of Directional Cell Motility Revealed Using Microcontact Printing. *Langmuir*, 19(5):1611–1617, March 2003. ISSN 0743-7463. doi: 10.1021/la026394k. URL `http://dx.doi.org/10.1021/la026394k`.

[156] Masha Prager-Khoutorsky, Alexandra Lichtenstein, Ramaswamy Krishnan, Kavitha Rajendran, Avi Mayo, Zvi Kam, Benjamin Geiger, and Alexander D. Bershadsky. Fibroblast polarization is a matrix-rigidity-dependent process controlled by focal adhesion mechanosensing. *Nature Cell Biology*, 13(12):1457–1465, December 2011. ISSN 1476-4679. doi: 10.1038/ncb2370. URL `https://www.nature.com/articles/ncb2370`.

[157] François Pouthas, Philippe Girard, Virginie Lecaudey, Thi Bach Nga Ly, Darren Gilmour, Christian Boulin, Rainer Pepperkok, and Emmanuel G. Reynaud. In migrating cells, the Golgi complex and the position of the centrosome depend on geometrical constraints of the substratum. *Journal of Cell Science*, 121(14):2406–2414, July 2008. ISSN 0021-9533, 1477-9137. doi: 10.1242/jcs.026849. URL `https://jcs.biologists.org/content/121/14/2406`.

[158] Young-Gwang Ko, Carlos C. Co, and Chia-Chi Ho. Directing cell migration in continuous microchannels by topographical amplification of natural directional persistence. *Biomaterials*, 34(2):353–360, January 2013. ISSN 0142-9612. doi:

10.1016/j.biomaterials.2012.09.071. URL `http://www.sciencedirect.com/science/article/pii/S0142961212010940`.

[159] Ronen Zaidel-Bar, Christoph Ballestrem, Zvi Kam, and Benjamin Geiger. Early molecular events in the assembly of matrix adhesions at the leading edge of migrating cells. *Journal of Cell Science*, 116(22):4605–4613, November 2003. ISSN 0021-9533, 1477-9137. doi: 10.1242/jcs.00792. URL `https://jcs.biologists.org/content/116/22/4605`.

[160] Y. L. Wang. Reorganization of actin filament bundles in living fibroblasts. *The Journal of Cell Biology*, 99(4):1478–1485, October 1984. ISSN 0021-9525, 1540-8140. doi: 10.1083/jcb.99.4.1478. URL `http://jcb.rupress.org/content/99/4/1478`.

[161] Harrison V. Prentice-Mott, Yasmine Meroz, Andreas Carlson, Michael A. Levine, Michael W. Davidson, Daniel Irimia, Guillaume T. Charras, L. Mahadevan, and Jagesh V. Shah. Directional memory arises from long-lived cytoskeletal asymmetries in polarized chemotactic cells. *Proceedings of the National Academy of Sciences*, 113(5):1267–1272, February 2016. ISSN 0027-8424, 1091-6490. doi: 10.1073/pnas.1513289113. URL `https://www.pnas.org/content/113/5/1267`.

[162] Man Lung Sham, Jing Li, Peng Cheng Ma, and Jang-Kyo Kim. Cleaning and Functionalization of Polymer Surfaces and Nanoscale Carbon Fillers by UV/Ozone Treatment: A Review. *Journal of Composite Materials*, 43(14):1537–1564, July 2009. ISSN 0021-9983. doi: 10.1177/0021998308337740. URL `https://doi.org/10.1177/0021998308337740`.

[163] Isabelle Beaulieu, Matthias Geissler, and Janine Mauzeroll. Oxygen Plasma Treatment of Polystyrene and Zeonor: Substrates for Adhesion of Patterned Cells. *Langmuir*, 25(12):7169–7176, June 2009. ISSN 0743-7463. doi: 10.1021/la9001972. URL `https://doi.org/10.1021/la9001972`.

[164] Magnus Bergkvist, Jan Carlsson, and Sven Oscarsson. Surface-dependent conformations of human plasma fibronectin adsorbed to silica, mica, and hydrophobic surfaces, studied with use of Atomic Force Microscopy. *Journal of Biomedical Materials Research Part A*, 64A(2):349–356, 2003. ISSN 1552-

4965. doi: 10.1002/jbm.a.10423. URL `https://onlinelibrary.wiley.com/doi/abs/10.1002/jbm.a.10423`.

[165] Frederick Grinnell. Fibronectin Adsorption on Material Surfacesa. *Annals of the New York Academy of Sciences*, 516(1):280–290, 1987. ISSN 1749-6632. doi: 10.1111/j.1749-6632.1987.tb33048.x. URL `https://nyaspubs.onlinelibrary.wiley.com/doi/abs/10.1111/j.1749-6632.1987.tb33048.x`.

[166] G. Altankov and Th. Groth. Reorganization of substratum-bound fibronectin on hydrophilic and hydrophobic materials is related to biocompatibility. *Journal of Materials Science: Materials in Medicine*, 5(9):732–737, September 1994. ISSN 1573-4838. doi: 10.1007/BF00120366. URL `https://doi.org/10.1007/BF00120366`.

[167] Steve Pawlizak, Anatol W. Fritsch, Steffen Grosser, Dave Ahrens, Tobias Thalheim, Stefanie Riedel, Tobias R. Kießling, Linda Oswald, Mareike Zink, M. Lisa Manning, and Josef A. Käs. Testing the differential adhesion hypothesis across the epithelial-mesenchymal transition. *New Journal of Physics*, 17(8):083049, August 2015. ISSN 1367-2630. doi: 10.1088/1367-2630/17/8/083049. URL `https://doi.org/10.1088%2F1367-2630%2F17%2F8%2F083049`.

[168] Yen-Liang Liu, Chao-Kai Chou, Mirae Kim, Rohan Vasisht, Yu-An Kuo, Phyllis Ang, Cong Liu, Evan P. Perillo, Yu-An Chen, Katherine Blocher, Hannah Horng, Yuan-I. Chen, Duc Trung Nguyen, Thomas E. Yankeelov, Mien-Chie Hung, Andrew K. Dunn, and Hsin-Chih Yeh. Assessing metastatic potential of breast cancer cells based on EGFR dynamics. *Scientific Reports*, 9(1):1–13, March 2019. ISSN 2045-2322. doi: 10.1038/s41598-018-37625-0. URL `https://www.nature.com/articles/s41598-018-37625-0`.

[169] U. H. Frixen, J. Behrens, M. Sachs, G. Eberle, B. Voss, A. Warda, D. Löchner, and W. Birchmeier. E-cadherin-mediated cell-cell adhesion prevents invasiveness of human carcinoma cells. *The Journal of Cell Biology*, 113(1):173–185, April 1991. ISSN 0021-9525, 1540-8140. doi: 10.1083/jcb.113.1.173. URL `http://jcb.rupress.org/content/113/1/173`.

[170] David Sarrió, José Palacios, Marta Hergueta-Redondo, Gonzalo Gómez-López, Amparo Cano, and Gema Moreno-Bueno. Functional characterization of E- and P-cadherin in invasive breast cancer cells. *BMC Cancer*, 9(1):74, March 2009. ISSN 1471-2407. doi: 10.1186/1471-2407-9-74. URL `https://doi.org/10.1186/1471-2407-9-74`.

[171] Tamer T. Onder, Piyush B. Gupta, Sendurai A. Mani, Jing Yang, Eric S. Lander, and Robert A. Weinberg. Loss of E-Cadherin Promotes Metastasis via Multiple Downstream Transcriptional Pathways. *Cancer Research*, 68(10): 3645–3654, May 2008. ISSN 0008-5472, 1538-7445. doi: 10.1158/0008-5472. CAN-07-2938. URL `https://cancerres.aacrjournals.org/content/68/10/3645`.

[172] Erika Jonietz. Mechanics: The forces of cancer. *Nature*, 491(7425):S56–S57, November 2012. ISSN 1476-4687. doi: 10.1038/491S56a. URL `http://www.nature.com/articles/491S56a`.

[173] Lena A. Lautscham, Christoph Kämmerer, Janina R. Lange, Thorsten Kolb, Christoph Mark, Achim Schilling, Pamela L. Strissel, Reiner Strick, Caroline Gluth, Amy C. Rowat, Claus Metzner, and Ben Fabry. Migration in Confined 3D Environments Is Determined by a Combination of Adhesiveness, Nuclear Volume, Contractility, and Cell Stiffness. *Biophysical Journal*, 109(5):900–913, September 2015. ISSN 0006-3495. doi: 10.1016/j.bpj.2015.07.025. URL `http://www.sciencedirect.com/science/article/pii/S0006349515007328`.

[174] Marco Falasca, Claudio Raimondi, and Tania Maffucci. Boyden Chamber. In Claire M. Wells and Maddy Parsons, editors, *Cell Migration: Developmental Methods and Protocols*, Methods in Molecular Biology, pages 87–95. Humana Press, Totowa, NJ, 2011. ISBN 978-1-61779-207-6. doi: 10.1007/978-1-61779-207-6_7. URL `https://doi.org/10.1007/978-1-61779-207-6_7`.

[175] Hynda K. Kleinman and Karin Jacob. Invasion Assays. *Current Protocols in Cell Biology*, 00(1):12.2.1–12.2.5, 1998. ISSN 1934-2616. doi: 10.1002/0471143030.cb1202s00. URL `https://currentprotocols.onlinelibrary.wiley.com/doi/abs/10.1002/0471143030.cb1202s00`.

[176] Janani P. Baskaran, Anna Weldy, Justinne Guarin, Gabrielle Munoz, Michael Kotlik, Nandita Subbiah, Andrew Wishart, Yifan Peng, Miles A. Miller, Lenore Cowen, and Madeleine J. Oudin. Cell shape, and not 2D migration, predicts ECM-driven 3D cell invasion in breast cancer. *bioRxiv*, page 2019.12.31.892091, January 2020. doi: 10.1101/2019.12.31.892091. URL `https://www.biorxiv.org/content/10.1101/2019.12.31.892091v1`.

[177] Daniel F. Milano, Nicholas A. Ngai, Senthil K. Muthuswamy, and Anand R. Asthagiri. Regulators of Metastasis Modulate the Migratory Response to Cell Contact under Spatial Confinement. *Biophysical Journal*, 110(8):1886–1895, April 2016. ISSN 0006-3495. doi: 10.1016/j.bpj.2016.02.040. URL `http://www.sciencedirect.com/science/article/pii/S0006349516301138`.

[178] Gražvydas Lukinavičius, Claudia Blaukopf, Elias Pershagen, Alberto Schena, Luc Reymond, Emmanuel Derivery, Marcos Gonzalez-Gaitan, Elisa D'Este, Stefan W. Hell, Daniel Wolfram Gerlich, and Kai Johnsson. SiR–Hoechst is a far-red DNA stain for live-cell nanoscopy. *Nature Communications*, 6 (1):1–7, October 2015. ISSN 2041-1723. doi: 10.1038/ncomms9497. URL `https://www.nature.com/articles/ncomms9497`.

[179] H. Schift, L. J. Heyderman, C. Padeste, and J. Gobrecht. Chemical nano-patterning using hot embossing lithography. *Microelectronic Engineering*, 61-62:423–428, July 2002. ISSN 0167-9317. doi: 10.1016/S0167-9317(02) 00513-0. URL `http://www.sciencedirect.com/science/article/pii/S0167931702005130`.

[180] Markus Rottmar, Maria Håkanson, Michael Smith, and Katharina Maniura-Weber. Stem cell plasticity, osteogenic differentiation and the third dimension. *Journal of Materials Science: Materials in Medicine*, 21(3):999–1004, March 2010. ISSN 1573-4838. doi: 10.1007/s10856-009-3926-7. URL `https://doi.org/10.1007/s10856-009-3926-7`.

[181] Alexandra Lynn McGregor, Chieh-Ren Hsia, and Jan Lammerding. Squish and squeeze—the nucleus as a physical barrier during migration in confined environments. *Current Opinion in Cell Biology*, 40:32–40, June 2016. ISSN 0955-0674. doi: 10.1016/j.ceb.2016.01.011. URL `http://www.sciencedirect.com/science/article/pii/S0955067416300035`.

[182] Delphine Antoni, Hélène Burckel, Elodie Josset, and Georges Noel. Three-Dimensional Cell Culture: A Breakthrough in Vivo. *International Journal of Molecular Sciences*, 16(3):5517–5527, March 2015. doi: 10.3390/ijms16035517. URL https://www.mdpi.com/1422-0067/16/3/5517.

[183] Jin-Ah Park, Jae Hun Kim, Dapeng Bi, Jennifer A. Mitchel, Nader Taheri Qazvini, Kelan Tantisira, Chan Young Park, Maureen McGill, Sae-Hoon Kim, Bomi Gweon, Jacob Notbohm, Robert Steward Jr, Stephanie Burger, Scott H. Randell, Alvin T. Kho, Dhananjay T. Tambe, Corey Hardin, Stephanie A. Shore, Elliot Israel, David A. Weitz, Daniel J. Tschumperlin, Elizabeth P. Henske, Scott T. Weiss, M. Lisa Manning, James P. Butler, Jeffrey M. Drazen, and Jeffrey J. Fredberg. Unjamming and cell shape in the asthmatic airway epithelium. *Nature Materials*, 14(10):1040–1048, October 2015. ISSN 1476-4660. doi: 10.1038/nmat4357. URL https://www.nature.com/articles/nmat4357.

[184] Jonathan M. Bélisle, Dario Kunik, and Santiago Costantino. Rapid multicomponent optical protein patterning. *Lab on a Chip*, 9(24):3580–3585, November 2009. ISSN 1473-0189. doi: 10.1039/B911967A. URL http://pubs.rsc.org/en/content/articlelanding/2009/lc/b911967a.

[185] Ansgar Waldbaur, Björn Waterkotte, Katja Schmitz, and Bastian E. Rapp. Maskless Projection Lithography for the Fast and Flexible Generation of Grayscale Protein Patterns. *Small*, 8(10):1570–1578, 2012. ISSN 1613-6829. doi: 10.1002/smll.201102163. URL https://onlinelibrary.wiley.com/doi/abs/10.1002/smll.201102163.

[186] Rodney T. Chen, Silvia Marchesan, Richard A. Evans, Katie E. Styan, Georgina K. Such, Almar Postma, Keith M. McLean, Benjamin W. Muir, and Frank Caruso. Photoinitiated Alkyne–Azide Click and Radical Cross-Linking Reactions for the Patterning of PEG Hydrogels. *Biomacromolecules*, 13(3):889–895, March 2012. ISSN 1525-7797. doi: 10.1021/bm201802w. URL https://doi.org/10.1021/bm201802w.

[187] Pierre-Olivier Strale, Ammar Azioune, Ghislain Bugnicourt, Yohan Lecomte, Makhlad Chahid, and Vincent Studer. Multiprotein Printing by Light-Induced Molecular Adsorption. *Advanced Materials*, 28(10):2024–2029, March

2016. ISSN 1521-4095. doi: 10.1002/adma.201504154. URL `http://onlinelibrary.wiley.com/doi/10.1002/adma.201504154/abstract`.

[188] Rahul G. Thakar, Qian Cheng, Shyam Patel, Julia Chu, Mansoor Nasir, Dorian Liepmann, Kyriakos Komvopoulos, and Song Li. Cell-Shape Regulation of Smooth Muscle Cell Proliferation. *Biophysical Journal*, 96(8):3423–3432, April 2009. ISSN 0006-3495. doi: 10.1016/j.bpj.2008.11.074. URL `http://www.sciencedirect.com/science/article/pii/S0006349509004883`.

[189] Daniel Lélis Baggio. ImageJ Ivussnakes plugin. URL `http://ivussnakes.sourceforge.net/`. Accessed on 1.12.2019.

[190] Caroline A. Schneider, Wayne S. Rasband, and Kevin W. Eliceiri. NIH Image to ImageJ: 25 years of image analysis. *Nature Methods*, 9(7):671–675, July 2012. ISSN 1548-7105. doi: 10.1038/nmeth.2089. URL `https://www.nature.com/articles/nmeth.2089`.

[191] S. Siegert, R. Friedrich, and J. Peinke. Analysis of data sets of stochastic systems. *Physics Letters A*, 243(5):275–280, July 1998. ISSN 0375-9601. doi: 10.1016/S0375-9601(98)00283-7. URL `http://www.sciencedirect.com/science/article/pii/S0375960198002837`.

[192] Mario Ragwitz and Holger Kantz. Indispensable Finite Time Corrections for Fokker-Planck Equations from Time Series Data. *Physical Review Letters*, 87(25):254501, December 2001. doi: 10.1103/PhysRevLett.87.254501. URL `https://link.aps.org/doi/10.1103/PhysRevLett.87.254501`.

[193] Greg J. Stephens, Bethany Johnson-Kerner, William Bialek, and William S. Ryu. Dimensionality and Dynamics in the Behavior of C. elegans. *PLOS Computational Biology*, 4(4):e1000028, April 2008. ISSN 1553-7358. doi: 10.1371/journal.pcbi.1000028. URL `https://journals.plos.org/ploscompbiol/article?id=10.1371/journal.pcbi.1000028`.

[194] Bradley Efron and R. J. Tibshirani. *An Introduction to the Bootstrap*. CRC Press, May 1994. ISBN 978-0-412-04231-7. Google-Books-ID: gLlpIUxRntoC.

Acknowledgements